

# Synthesis and Characterization of Semiconductor and Semiconductor-Metal Nanoparticles

Von der Fakultät für Mathematik und Naturwissenschaften der Carl von  
Ossietsky Universität Oldenburg zur Erlangung des Grades und Titels eines

*Doctor rerum naturalium (Dr. rer. nat.)*

angenommene Dissertation

von

Frau Elena Selishcheva

geboren am 4.2.1985 in Woronesch (Russland)



---

Gutachter: Prof. Dr. Joanna Kolny-Olesiak

Zweitgutachter: Prof. Dr. Jürgen Parisi

Tag der Disputation: 19.12.2011

## Abstract

Nanoparticles are promising materials for many physical and chemical applications, because their properties depend on their size and shape, which can be controlled during the synthesis.

This work is a contribution to the development of colloidal synthesis of different nanomaterials, such as lead chalcogenide PbE (E = S, Se, Te), indium oxide ( $\text{In}_2\text{O}_3$ ) nanoparticles, and hybrid nanostructures, consisting of copper indium sulfide selenide (CuInSSe) and gold nanoparticles.

After a short general introduction into the theory of synthesis of nanomaterials, the investigations of the three systems mentioned above are described. In the first part, nearly monodisperse PbE semiconductor nanoparticles produced via a novel synthesis which includes the occurrence of in situ formed  $\text{Pb}^0$ -particles are shown. Spherical PbSe nanoparticles are further investigated with respect to possible application in hybrid solar cells.

The second part is about a novel non-injection synthesis route for the preparation of colloidal  $\text{In}_2\text{O}_3$  nanocrystals. The shape of the nanocrystals can be influenced by the addition of copper ions.

Finally, the selective growth of gold nanocrystals onto CuInSSe nanoparticles to form semiconductor/metal hybrid nanostructures is demonstrated. The CuInSSe nanoparticles used in our experiments have a trigonal pyramidal shape. During the synthesis gold nanocrystals grow onto vertexes of CuInSSe pyramids.

X-ray diffraction, transmission electron microscopy, nuclear magnetic resonance, UV-Vis absorption, photoluminescence and energy dispersive X-ray spectroscopy are used to characterize the samples.

---



## Kurzfassung

Nanopartikel sind ein vielversprechendes Material für viele physikalische und chemische Anwendungen, da ihre Eigenschaften von den Größen und Formen abhängen, welche während der Synthese kontrollierbar sind.

Diese Arbeit ist ein Beitrag zur die Entwicklung der kolloidalen Synthese von verschiedenen Nanomaterialien, wie Bleichalkogenide(PbE, E = S, Se, Te)- und Indiumoxid( $\text{In}_2\text{O}_3$ )-Nanopartikeln sowie hybriden Nanostrukturen, die aus Kupferindiumsulfidselenid( $\text{CuInSSe}$ )- und Gold-Nanopartikeln bestehen.

Nach einer kurzen allgemeinen Einleitung in die Theorie der Synthese von Nanomaterialien werden die drei oben genannten Systeme beschrieben. In dem ersten Teil werden quasi monodisperse PbE-Halbleiternanopartikel gezeigt, die mittels neuer Methode mit der Bildung von  $\text{Pb}^0$ -Partikeln synthetisiert werden. Sphärische PbSe-Nanopartikel werden für die Anwendung in hybriden Solarzellen untersucht.

Der zweite Teil handelt von der neuen Synthese für die Herstellung von kolloidalen  $\text{In}_2\text{O}_3$ -Nanokristallen. Die Form der Nanokristalle konnte durch die Zugabe von Cu-Ionen beeinflusst werden.

Schließlich wird das selektive Wachstum von Gold-Nanokristallen auf den  $\text{CuInSSe}$ -Nanopartikeln mit der Bildung von hybriden Metall-Halbleiter-Nanostrukturen dargestellt. Die  $\text{CuInSSe}$ -Nanopartikel haben eine pyramidale Form. Während der Synthese wachsen Gold-Nanokristalle auf den Spitzen dieser  $\text{CuInSSe}$ -Pyramiden.

Transmissionselektronenmikroskopie, UV-Vis Absorptions- und Photolumineszenz-Spektroskopie, Röntgenbeugung, Energiedispersive Röntgenspektroskopie und Kernspinresonanzspektroskopie werden für die Probencharakterisierung verwendet.

---

## Acknowledgements

I would like to thank all my colleagues who contributed to this work, especially Jun.-Prof. Dr. Joanna Kolny-Olesiak for enabling me to accomplish my PhD; Prof. Dr. Jürgen Parisi for his support and agreement to referee this thesis; Dr. Holger Borchert for good co-operations related to PbSe NPs; Dr. Erhard Rhiel, Heike Oetting, and Renate Kort for assistance in obtaining TEM images and EDX data, Andrea Tschirne and Dieter Neemeyer for assistance in obtaining NMR data, Florian Witt and Niklas Trautwein for ESR and PIA measurements, Dr. Daniela Fenske and Johannes Neumann for assistance in obtaining TGA data, Dr. Karsten Thiel for assistance in obtaining HRTEM images, Kambulakwao Chakanga from EWE-Forschungszentrum für Energietechnologie e. V. for assistance in obtaining absorption spectra; Dr. Irina Lokteva for her help to start my work here, Marta Kruszynska for synthesis of CuInS<sub>2</sub> NPs used in this thesis, Dr. Xiaodong Wang, Dr. Jie Li, Xiaoping Jin, and Björn Kempken for a nice collaboration, and Matthias Macke for the necessary chemicals. I am very grateful to Florian for his help with LATEX and my family for support during the past years. "EWE-Nachwuchsgruppe Dünnschicht Photovoltaik" by the EWE AG, Oldenburg is acknowledged for financial support.

---

# Contents

List of Figures	xiii
Glossary	xvii
<b>1 Introduction</b>	<b>1</b>
<b>2 Theoretical background</b>	<b>5</b>
2.1 Nanomaterials, their properties and application . . . . .	5
2.1.1 Hybrid nanomaterials . . . . .	13
2.2 Theory of nanocrystal synthesis . . . . .	15
2.2.1 Impact of experimental conditions . . . . .	15
2.2.2 Formation mechanism of spherical nanoparticles . . . . .	17
2.2.3 Shape control of nanoparticles . . . . .	24
2.2.4 Synthesis of hybrid nanostructures . . . . .	26
2.3 Characterization methods . . . . .	27
2.3.1 Electron microscopy . . . . .	27
2.3.2 X-ray characterization methods . . . . .	29
2.3.3 Optical studies . . . . .	31
2.3.4 Thermodynamic characterization methods . . . . .	32
<b>3 Experimental part</b>	<b>35</b>
3.1 Synthesis of lead chalcogenide nanocrystals . . . . .	35
3.1.1 Hexylamine treatment of original PbSe nanocrystals . . . . .	37
3.2 Synthesis of indium oxide nanoparticles . . . . .	37
3.2.1 Synthesis of flower-shaped In <sub>2</sub> O <sub>3</sub> nanocrystals . . . . .	38
3.2.2 Synthesis of In <sub>2</sub> O <sub>3</sub> nanocrystals employing organic ligand molecules	38

## CONTENTS

---

3.2.3	Synthesis of quasi-spherical $\text{In}_2\text{O}_3$ nanocrystals . . . . .	38
3.2.4	Synthesis of elongated $\text{In}_2\text{O}_3$ nanocrystals . . . . .	39
3.3	Synthesis of CIS and CIS/Au hybrid nanoparticles . . . . .	39
3.3.1	Synthesis of CIS nanoparticles . . . . .	39
3.3.2	Synthesis of CIS/Au hybrid nanoparticles . . . . .	40
3.4	Materials . . . . .	41
3.5	Characterization . . . . .	41
<b>4</b>	<b>Hot-injection synthesis of lead chalcogenide nanocrystals: Influence of synthesis mechanism on the nanocrystal surface properties</b>	<b>45</b>
4.1	Motivation . . . . .	45
4.2	Size and shape control of lead chalcogenide nanoparticles . . . . .	47
4.3	Reaction mechanism and product characterisation . . . . .	52
4.4	Surface investigation . . . . .	57
4.5	Study of charge transfer in blends of PbSe nanocrystals and P3HT . . . . .	60
4.6	Conclusion . . . . .	62
<b>5</b>	<b>Non-injection synthesis of <math>\text{In}_2\text{O}_3</math> nanoparticles and their shape control</b>	<b>65</b>
5.1	Motivation . . . . .	65
5.2	Synthesis investigation and characterization of flower-shaped $\text{In}_2\text{O}_3$ nanoparticles . . . . .	66
5.3	Shape control of $\text{In}_2\text{O}_3$ nanoparticles using organic ligand molecules . . . . .	71
5.4	Shape control of $\text{In}_2\text{O}_3$ nanoparticles using copper ions . . . . .	72
5.5	Conclusion . . . . .	77
<b>6</b>	<b>Synthesis and characterization of CIS/Au hybrid nanoparticles</b>	<b>79</b>
6.1	Motivation . . . . .	79
6.2	Synthesis and characterization of CuInSSe nanoparticles . . . . .	82
6.3	Synthesis and characterization of CuInSSe/Au hybrid nanostructures . . . . .	85
6.4	CuInS <sub>2</sub> /Au hybrid nanostructures: Difference in the synthesis mechanism . . . . .	89
6.5	Conclusion . . . . .	91
<b>7</b>	<b>Summary</b>	<b>93</b>

## CONTENTS

---

<b>A H-phrases and P-phrases</b>	<b>95</b>
A.1 Chemicals . . . . .	95
A.2 H-Statements . . . . .	98
A.3 P-Statements . . . . .	102
<b>Bibliography</b>	<b>111</b>

## CONTENTS

---



# List of Figures

2.1	Metric scale for classifying nanoparticles . . . . .	5
2.2	Size-dependent melting point of gold NPs . . . . .	6
2.3	CdSe NP suspensions in toluene . . . . .	7
2.4	Shape-dependent properties . . . . .	8
2.5	Fraction the surface atoms for sperical and elongated nanocrystals . . . . .	9
2.6	Examples of the application of semiconductor nanoparticles in solar cells (a) and in biology (b) . . . . .	10
2.7	TEM images of hybrid materials . . . . .	13
2.8	Electronic properties of hybrid materials . . . . .	14
2.9	Scheme of nanoparticle synthesis . . . . .	16
2.10	LaMer-diagram . . . . .	18
2.11	Free energy diagram . . . . .	19
2.12	Shape control . . . . .	25
2.13	A scheme illustrating heterogeneous deposition modes for material "2" from its precursor onto a seed substrate of material "1" . . . . .	27
2.14	A schematic representation of transmission electron microscope . . . . .	28
2.15	X-ray diffraction . . . . .	30
2.16	Energy dispersive X-ray spectroscopy . . . . .	31
2.17	Thermal gravimetric analysis . . . . .	32
3.1	Scheme of the experimental set-up for colloidal nanoparticle preparation using a hot-injection method . . . . .	36
3.2	Scheme of the experimental set-up for colloidal nanoparticle preparation using a non-injection technique . . . . .	37

## LIST OF FIGURES

---

3.3	Scheme of the experimental set-up for colloidal seed preparation using a hot-injection technique . . . . .	39
3.4	Scheme of the experimental set-up for colloidal preparation of hybrid nanostructures using a seed-mediated method . . . . .	40
4.1	TEM images of lead chalcogenide nanocrystals . . . . .	47
4.2	TEM images of spherical PbSe and cubic PbTe NCs illustrating the size control . . . . .	48
4.3	TEM images of PbSe NCs demonstrating the shape control . . . . .	49
4.4	TEM images of PbS nanorods . . . . .	49
4.5	TEM images of PbS NCs demonstrating the shape control . . . . .	50
4.6	XRD measurement of the Pb <sup>0</sup> precipitate . . . . .	52
4.7	Scheme of Pb precursor formation . . . . .	52
4.8	NMR measurements clarified reaction mechanism . . . . .	53
4.9	TEM image of as-synthesized PbSe NCs . . . . .	54
4.10	XRD measurement of the PbSe NCs . . . . .	55
4.11	EDX measurement of the PbSe NCs . . . . .	56
4.12	Thermogravimetric analysis of original and hexylamine-treated PbSe NCs	57
4.13	TEM images of original and hexylamine-treated PbSe NCs . . . . .	58
4.14	NMR measurement of PbSe NCs . . . . .	59
4.15	Photoinduced absorption spectrum of a P3HT/PbSe bulk heterojunction film . . . . .	60
4.16	Light induced electron spin resonance spectra of a P3HT/PbSe bulk heterojunction film . . . . .	62
5.1	TEM and HRTEM images of the In <sub>2</sub> O <sub>3</sub> NPs produced by the reaction of indium (III) acetate with oleylamine . . . . .	66
5.2	Powder X-ray diffraction patterns of flower-shaped In <sub>2</sub> O <sub>3</sub> nanoparticles produced by heating indium (III) acetate with oleylamine . . . . .	67
5.3	Absorption spectra of the samples taken from the reaction between indium acetate and oleylamine . . . . .	68
5.4	PL spectra of the samples taken from the reaction between indium acetate and oleylamine . . . . .	69

## LIST OF FIGURES

---

5.5	NMR spectra of the samples taken from the reaction between indium acetate and oleylamine . . . . .	70
5.6	TEM image of $\text{In}_2\text{O}_3$ NPs synthesized using organic ligand for stabilization	71
5.7	XRD of $\text{In}_2\text{O}_3$ NPs synthesized with increased amount of TOPO . . . . .	72
5.8	TEM images of $\text{In}_2\text{O}_3$ nanoparticles synthesized using $\text{Inac}_3$ and different copper salts . . . . .	73
5.9	X-ray diffraction pattern of the $\text{In}_2\text{O}_3$ nanoparticles produced by employing of Cuac together with copper particles . . . . .	74
5.10	Separation of $\text{In}_2\text{O}_3$ and Cu NPs through centrifugation . . . . .	74
5.11	TEM and HRTEM images as well as EDX measurement of $\text{In}_2\text{O}_3$ NPs .	75
5.12	Scheme of the reaction . . . . .	76
5.13	TEM image of the $\text{In}_2\text{O}_3$ nanoparticles synthesized using copper (I) acetate and indium (III) chloride . . . . .	77
6.1	Scheme of growth mechanism in the synthesis of hybrid nanostructures .	80
6.2	TEM image of the CuInSSe NPs . . . . .	82
6.3	EDX measurement of the CuInSSe NPs . . . . .	83
6.4	Powder X-ray diffraction patterns of the CuInSSe NPs . . . . .	84
6.5	Absorption spectrum of the original CuInSSe NPs . . . . .	85
6.6	TEM image of the CuInSSe-based hybrid nanostructures . . . . .	86
6.7	Powder X-ray diffraction patterns of the hybrid nanostructures . . . . .	87
6.8	Comparison of the absorption of the semiconductor and resulting semiconductor-metal nanostructures . . . . .	88
6.9	EDX measurement of the CuInSSe/Au NPs . . . . .	89
6.10	TEM image of the $\text{CuInS}_2/\text{Au}$ NPs . . . . .	90
6.11	Comparison of the absorption spectra of the original $\text{CuInS}_2$ NPs (a) and $\text{CuInS}_2/\text{Au}$ hybrid nanostructures (b) . . . . .	91
6.12	Comparison of the mechanism of the formation of hybrid CIS/Au NPs .	92
A.1	Structure of the H- and P-Statements . . . . .	95

## **GLOSSARY**

---

# Glossary

<b>ac</b>	Acetate	<b>NCs</b>	Nanocrystals
<b>acac</b>	Acetylacetonate	<b>NIR</b>	Near-Infrared
<b>CIS</b>	Copper Indium Sulfide and/or Selenide	<b>NMR</b>	Nuclear Magnetic Resonance
<b>DDA</b>	Dodecylamine	<b>NPs</b>	Nanoparticles
<b>DDAB</b>	Dodecyldimethylammoniumbromide	<b>OA</b>	Oleic Acid
<b>DDT</b>	1-Dodecanethiol	<b>ODE</b>	1-Octadecene
<b>EDX</b>	Energy Dispersive X-ray analysis	<b>OLA</b>	Oleylamine
<b>ESR</b>	Electron Spin Resonance	<b>P3HT</b>	Poly-3-Hexylthiophene
<b>HDA</b>	Hexadecylamine	<b>PEDOT:PSS</b>	Poly(3,4-Ethylenedioxythiophene) mixed with poly(Styrenesulfonate)
<b>HOMO</b>	Highest Occupied Molecular Orbitals	<b>PIA</b>	Photoinduced Absorption spectroscopy
<b>HRTEM</b>	High-Resolution Transmission Electron Microscopy	<b>PL</b>	Photoluminescence
<b>ICDD</b>	International Centre for Diffraction Data	<b>TBP</b>	Tributylphosphine
<b>ITO</b>	Indium Tin Oxide	<b>TEM</b>	Transmission Electron Microscopy
<b>LUMO</b>	Lowest Unoccupied Molecular Orbitals	<b>TGA</b>	Thermal Gravimetric Analysis
		<b>TMS</b>	Tetramethylsilane
		<b>TOP</b>	Trioctylphosphine
		<b>TOPO</b>	Trioctylphosphine Oxide
		<b>UV</b>	Ultraviolet
		<b>Vis</b>	Visible
		<b>XRD</b>	X-ray diffraction

## GLOSSARY

---

# Chapter 1

## Introduction

Over the past years so-called nanomaterials have acquired much attention in science and industry. The main reason for that is the possibility to control certain properties of such materials. While scientists study and describe systematically the processes responsible for the tunable properties as well as laws working at this frontier of physics and chemistry, the industrial world expects numerous possible applications of nanomaterials such as fabrication of more efficient physical devices (e.g. solar cells), catalysts in chemistry, or *in vivo* analysis of the biological bodies as well as treatment of diseases. There are already examples of involving nanoparticles in industrial products. Cosmetic industry uses  $\text{TiO}_2$  and  $\text{ZnO}$  nanoparticles for skin protection from ultraviolet (UV) radiation. Gold nanocrystals are applied for dyeing glass [1].

The success of the research and application of nanomaterials depends on their quality which can be influenced by their preparation. The material synthesis is a prerequisite of its further characterization and use in practice. Thus, the study of the synthetic procedure (its standard stages, mechanism, kinds, and possible techniques) takes an important place in the scientific world.

Since 1980 the synthetic technique has been developed to a high level. Control of the nanoparticle morphology has been achieved for different types of nanomaterials [2, 3, 4]. The most successful approaches are associated with scientists such as Bawendi [5], who introduced the hot-injection synthetic technique in his report on the synthesis of cadmium chalcogenide nanocrystals, Alivisatos and Peng [6], who presented for the first time the synthesis of  $\text{CdSe}$  nanorods, and Murphy [7], who demonstrated seed-mediated growth method. Since numerous existing synthetic methods need to be refined and

## 1. INTRODUCTION

---

applied to different materials as well as advanced nanostructures need to be produced for multiple applications, many challenges are present in the field of nanochemistry.

This thesis bases on the study of the colloidal synthesis of different semiconductors such as lead chalcogenide and indium oxide as well as semiconductor-metal nanomaterials (CuInSSe/Au). After the description of the theoretical background of the research objects (nanomaterials as well as synthesis) and the characterization methods used for determination of nanomaterial properties and the development of preparation process (Chapter 2), three different research systems are demonstrated. To begin with a hot-injection synthesis of lead chalcogenide nanoparticles (Chapter 4), continued with a non-injection synthesis of indium oxide nanoparticles (Chapter 5), the synthesis of hybrid CuInSSe/Au nanoparticles (Chapter 6) is presented based on the seed-mediated growth technique.

In this work, the well known hot-injection synthesis route of lead chalcogenide nanoparticles (PbE NPs) has been modified. That has a strong influence on the mechanism of this synthesis with respect to organic ligand molecules used for stabilization of nanoparticles. Consequently, the surface properties of the resulting product have been changed, since the original ligands applied in the synthesis were not present on the surface. Furthermore, a post-synthetic surface properties modification of as-synthesized PbSe NPs has been successfully carried out, what is important for further application in photovoltaics. With this particles a photophysical study [8] has been performed using photoinduced absorption (PIA) and electron spin resonance (ESR) spectroscopy. These measurements show promising results for their application in solar cells.

Next, the different approaches of a non-injection synthetic route have been applied to the preparation of  $\text{In}_2\text{O}_3$  NPs in order to control their shape with the focus on the processes taking place in this system. An easy and fast heating up approach involving only two compounds (In precursor and stabilizer) has been developed for producing flower-shaped  $\text{In}_2\text{O}_3$  NPs, which are formed from small particles through an oriented attachment mechanism. Thus, to stabilize every small nanoparticle two different strategies were applied, in particular the organic and the inorganic approach. Besides the possibility to control the branching of the flower-shaped nanocrystals by using additional organic ligands, the influence of copper ions on the studied system has been observed in the case of an inorganic shape control method: These ions could stabilize small  $\text{In}_2\text{O}_3$  NPs without the doping of Cu into  $\text{In}_2\text{O}_3$  crystallographic structure. Since,



---

on the one hand,  $\text{In}_2\text{O}_3$  is sensitive for toxic gases, and, on the other hand, the change of the nanoparticle shape leads to a change of the surface atoms number, this study is of interest for the research of sensor devices.

Finally, semiconductor-metal nanostructures involving metallic gold and semiconductor CIS ( $\text{CuInSSe}$  or  $\text{CuInS}_2$ ) nanoparticles have been produced using a seed-mediated method reported for lead and cadmium chalcogenide nanoparticles. The semiconductor part has been chosen in order to avoid the toxicity of Cd and Pb compounds. The results of the synthesis mechanism study of this system show the growth of gold nanocrystals onto the CIS NP surface. Apart from the placement of gold onto surface defects on the  $\text{CuInS}_2$  NPs, the occurrence of crystalline selenium nanoparticles has been demonstrated for  $\text{CuInSSe}$  NPs, while gold reduces onto its surface. Thus, the resulting nanoparticles consist of one structure with three compounds, in particular  $\text{CuInSSe}$ , Se and Au NPs. This system belongs to the class of the new hybrid nanostructures.

The Hazard and Precautionary statements for chemicals used in this thesis are listed in the Appendix.

## 1. INTRODUCTION

---

## Chapter 2

# Theoretical background

### 2.1 Nanomaterials, their properties and application

Nanoparticles are, by definition, particles with the size of 1-100 nm in at least one dimension [9]. These substances are categorized on the metric scale in between atoms

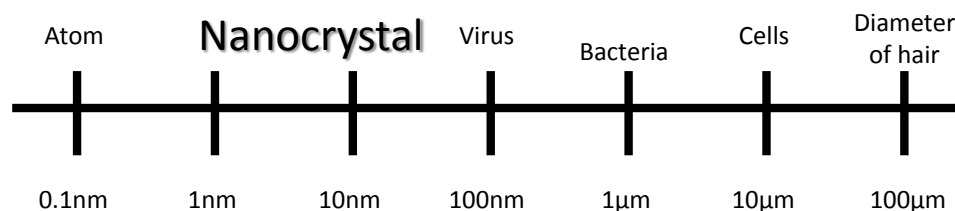


**Figure 2.1:** Metric scale for classifying nanoparticles - modified reproduction of [1].

or molecules and bulk materials as shown in figure 2.1 [10]. The nanoparticles are so small that they do not show fully delocalized electron properties as they occur in bulk crystals. Still, the nanocrystals possess some unique properties which do not show up on atomic and molecular scale.

In particular, scaling the material size to the nanometer region leads to a high surface to volume ratio. The large amount of surface atoms on the nanoparticle already causes differences in the properties of nanomaterials in comparison to those of bulk materials. Their surface energy significantly contributes to the free energy of whole system [3]. Therefore, by variation of the particle size, and thus the surface, the thermodynamic properties of this system can be changed. The reduction of the melting

## 2. THEORETICAL BACKGROUND

---

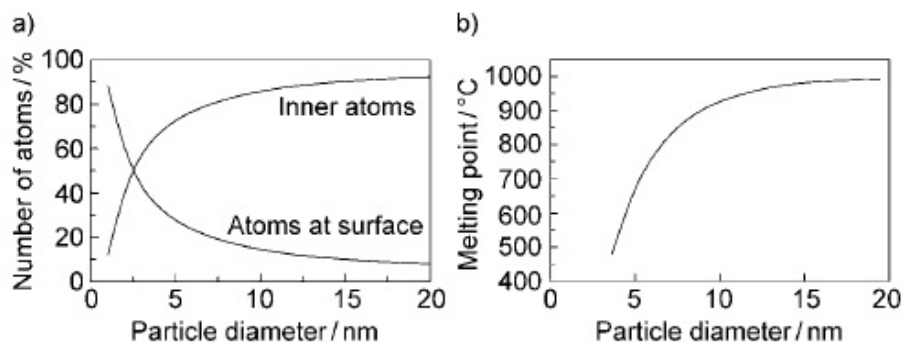


**Figure 2.2: Size-dependent melting point of gold NPs** - a) Number of surface and inner atoms as function of particle diameter and b) correlation between particle diameter and melting point of gold NPs (taken from [1]).

point of gold nanocrystals with decreasing particle size can serve as an example (figure 2.2). Furthermore, the catalytic activity of the materials can be improved. The vast surface area of nanomaterials provides a lot of catalytically active centers. Another deciding factor is the control of the catalytic selectivity. That is of great importance for the application of nanoparticles in catalysis.

Together with the high surface to volume ratio another major effect causes the specific properties of nanomaterials. That is the direct influence of the particle size on its electronic structure, which is called "quantum size effect" [1]. This can be visualized by considering the transition from discrete atomic energy levels to the dispersed bands of the bulk material. In the case of semiconductor nanoparticles, the band gap increases as the particle size decreases. One of the most impressive examples for that are the size-dependent optical properties of CdSe NPs (figure 2.3). When the nanoparticles become smaller, a blue shift in their absorption and emission spectra is observed. This is a direct result of the increasing band gap energy.

The quantum size effect can be theoretically described by a quantum-mechanical "particle-in-a-box" model. When the radius of the nanoparticle becomes smaller than its exciton Bohr radius, then the charges of the excitonic electron-hole pair are confined in a small volume and consequently the band gap increases [11]. Essentially, at such a small nanoparticle size the electron and hole interactions with the NP surface dominate the dynamics and the energy level scheme depends on the size, shape, and nature of the material [12]. There will be a series of excited, discrete bound states approaching an

## 2.1 Nanomaterials, their properties and application

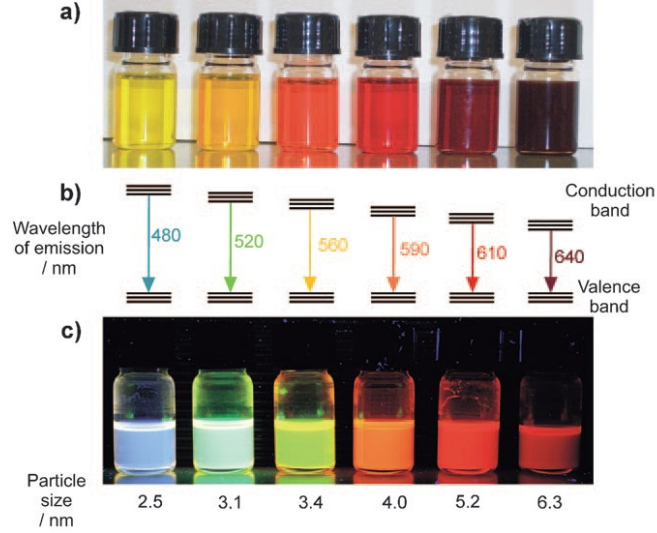


**Figure 2.3: CdSe NP suspensions in toluene** - a) Surface color in visible light, b) diagram of band gap and emission color depending on particle size, c) light emission by excitation with UV light (taken from [1]).

ionization limit corresponding to a positively charged nanoparticle and a free electron in vacuum. Schrödinger's equation for the excited states within the quantum confinement region in a sphere with radius  $R$  is given by

$$\left[ \frac{-\hbar}{2m_e} \nabla_e^2 + \frac{-\hbar}{2m_h} \nabla_h^2 + V_0(\overline{S}_e, \overline{S}_h) \right] \Phi(\overline{S}_e, \overline{S}_h) = E \Phi(\overline{S}_e, \overline{S}_h), \quad (2.1)$$

where  $m_e$  and  $m_h$  are electron and hole effective masses respectively,  $V_0$  is potential energy, and  $\overline{S}_e, \overline{S}_h$  are the positions of the charges in the nanoparticle.

At small  $R$ , the wave function  $\Phi$  will be dominated by the charge confinement, and  $E$  will increase. An approximate solution to  $\Phi$  in this limiting range is given by the wave function for a particle in a sphere:

$$\Psi_n(r) = \frac{C_n}{r} \sin(n\pi r/R). \quad (2.2)$$

The energy  $E$  is given by

$$E_n = \frac{\hbar^2 \pi^2 n^2}{2mR^2}, \quad (2.3)$$

where  $m$  is the appropriate effective mass.

The simple uncorrelated solution

$$\Phi_0 = \Psi_1(\overline{S}_e) \Psi_1(\overline{S}_h) \quad (2.4)$$

## 2. THEORETICAL BACKGROUND

---

is a fair approximation for some materials in this range of  $R$ .

With the wave function  $\Phi_0$  the energy of the lowest excited state becomes

$$E = \frac{\hbar^2 \pi^2}{2R^2} \left[ \frac{1}{m_e} + \frac{1}{m_h} \right] - \frac{1.8e^2}{4\pi\epsilon_0\epsilon R}, \quad (2.5)$$

where the first term is the quantum energy of localization, increasing with  $R^{-2}$  for both electron and hole; the second term is the Coulomb attraction, increasing with  $R^{-1}$  [13].

The equation (2.5) shows the size-dependence of the band gap. If the particle radius is smaller than the Bohr radius of the corresponding exciton, then the band gap increases with decreasing particle radius.

As it was already mentioned not only the size as a geometrical parameter, but also the shape of nanocrystals influences their properties. The shape is usually classified by their dimensionality: isotropic spheres, cubes, and polyhedrons belong to zero-dimensional (0D); rods and wires to 1D; discs, prisms, and plates to 2D structures [3]. By decreasing the dimensionality, there is a transition from a continuous density of energy states to a discrete one (figure 2.4). Furthermore, the nanocrystal shape

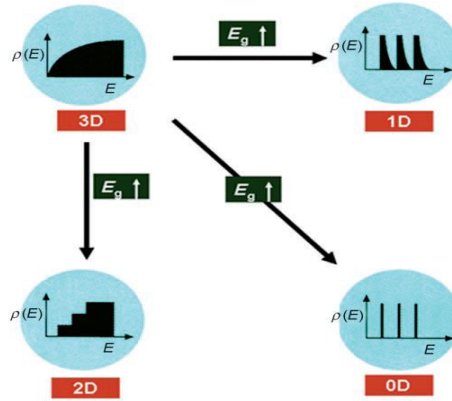


**Figure 2.4: Shape-dependent properties** - The smooth square-root density of states as a function of energy (for 3D crystals) changes to a discrete line (for 0D crystals) (taken from [3]).

influences the band-gap energy [14]. In CdSe nanorods it was observed that strong quantum confinement effects appear by the reduction of the diameter, while weaker quantum confinement effects were due to the length reduction. In contrast to spherical NCs, CdSe nanorods exhibit linearly polarized light emission [15]. Additionally, the number of the surface atoms is different for diverse shapes. Compared to other shapes,

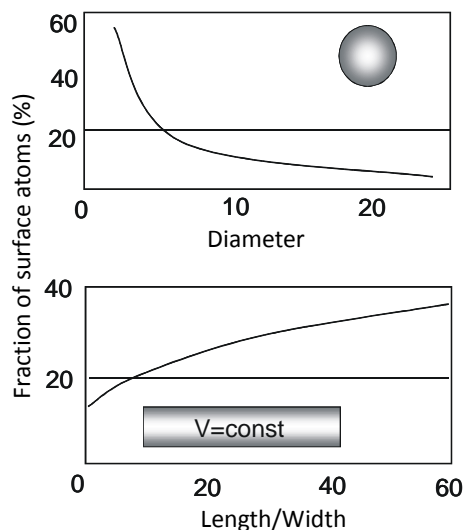


**Figure 2.5: Fraction the surface atoms for sperical and elongated nanocrystals**  
 - The volume of the rod-shaped particle is equivalent to an 8 nm diameter round particle.

the spherical nanocrystals have the smallest surface atom contribution, which decreases with the nanoparticle growth [11]. In contrast, the contribution of the surface atoms in a nanorod increases with increasing aspect ratio (figure 2.5).

The material plays also a significant role for nanoparticle properties. An interesting material class are the metal chalcogenides, which belong to semiconductors. Such nanoparticles demonstrate size-dependent optical properties, as it was shown above (see figure 2.3), that finds application in biological labeling and diagnostics, lasers, light emitting diodes, photovoltaic devices, and single-electron transistors [16, 17, 18, 19].

For example, CdSe or CdTe nanoparticles are used in photovoltaics for the preparation of solar cells [13]. Figure 2.6(a) illustrates the schematic architecture of so-called bulk heterojunction solar cell. A blend of two different materials called "bulk heterojunction" is used as the active layer. It is placed between two electrodes (Al and indium tin oxide (ITO)), where one of them is transparent (ITO). Material layers for transport of only holes (or only electrons) may be inserted between the bulk heterojunction and the electrodes (on the picture that is the polymer Poly(3,4-Ethylenedioxythiophene) mixed with poly(Styrenesulfonate) (PEDOT:PSS) used for hole transport). The conversion of sunlight to electricity can be divided in few steps: first, the absorption of light causes the generation of an exciton (electron-hole pair) in the active layer, followed

## 2. THEORETICAL BACKGROUND

---

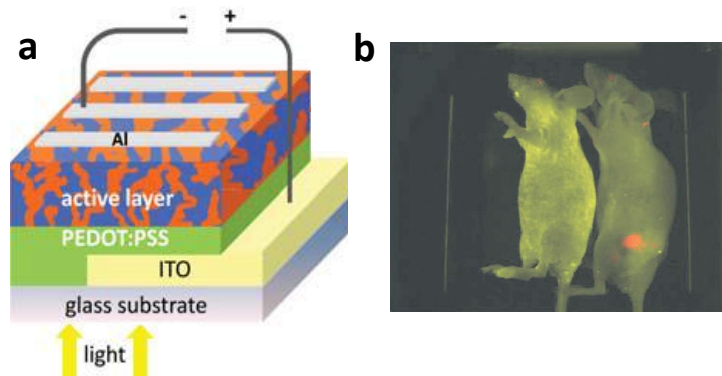


**Figure 2.6: Examples of the application of semiconductor nanoparticles in solar cells (a) and in biology (b)** - a) Scheme of a bulk heterojunction solar cell (taken from [13]) and b) *in vivo* detection of a prostate cancer in a mouse model before and after adding antibody-marked CdSe@ZnS quantum dots (taken from [20]).

by the charge separation and carrier transport (electrons - to the cathode and holes - to the anode) [13]. Due to the quantum size effect the absorption of the semiconductor nanoparticles is tunable over a wide range of the optical spectrum, that makes them attractive for the use in the active layer. Additionally, using nanoparticles with different shapes (for example, elongated CdSe nanocrystals [19]) can improve the electron transport in solar cell.

Biology and medicine are another interesting field for the application of semiconductor nanoparticles based on their ability to emit light. Due to the quantum confinement effect the nanoparticles have several advantages, such as high photostability, and long excited-state lifetime [21]. Their emission spectra can be tuned over a wide range of wavelength. Furthermore, the full width at half-maximum of the emission bands is relatively narrow, so the probability of a spectral overlap is reduced. Finally, the detection sensitivity is better optimized in comparison to conventional fluorophores. By using such nanomaterials, non-invasive *in vivo* whole-body diagnosis as well as *in vitro* examination of individual organs or cells have been developed [1]. The optical *in vivo* detection of a prostate carcinoma by means of antibody-functionalized CdSe@ZnS quantum dots is demonstrated in figure 2.6(b).

The commonly studied semiconductor nanoparticles consisted of materials absorbing in the visible range of the spectrum. Recently, the interest in near-infrared (NIR) ab-



## 2.1 Nanomaterials, their properties and application

---

<b>PbE/properties</b>	PbS	PbSe	PbTe
Bandgap (298K), eV [22]	0.41	0.278	0.31
Bandgap (4K), eV [22]	0.29	0.17	0.19
Dielectric constant	200	250 [25]	1000 [26]
Bohr radius, nm	18 [22]	46 [22]	46 [27]

**Table 2.1:** Properties of lead chalcogenides

sorbing materials has grown rapidly [22]. With respect to photovoltaics, such nanoparticles open the opportunity to use the sunlight more effectively. Also in the biological research these materials are advantageous because of their optical properties. Thick tissues in living animal models transmit the visible light poorly. Additionally, the autofluorescence of endogenous fluorophores appears at the visible range. In contrast, the NIR region is a "clear window" for most biological tissues [21]. That makes the NIR absorbing nanomaterials a promising candidate for biological application.

Lead chalcogenide (PbE, E = S, Se, Te) nanoparticles are some of the promising semiconductor materials for IR applications. These materials display several unique and unusual properties [23, 24]. PbE have relatively narrow bandgaps, large static dielectric constants, and large exciton Bohr radii (table 2.1). Furthermore, the effective masses of the electrons and holes are small and approximately equal [22]. The consequences are as following: The large Bohr radii are distributed almost equally between the electron and hole. Thus, both charge carriers are individually and strongly confined. This leads to a bandgap that can be several times larger than the one of the bulk. In other words, the absorption of PbE NPs can be easily tuned in the NIR or IR region (0.5-2.5 $\mu\text{m}$  for PbSe [21]). Additionally, the phenomenon of multiple exciton generation can occur [28]. In this process an exciton created by absorption of light with an energy exceeding the double of the band gap can relax by impact ionization. In this case, energy is transferred to another valence electron and a second electron-hole pair is created. This phenomenon provides solar cells based on lead chalcogenides a high potential for reducing thermalization losses [13]. The PbE nanoparticle emission in the NIR region is an ideal property for biological applications, as described above.

Another alternative material absorbing in NIR are I-III-VI semiconductor nanoparticles. Such materials are successfully used in inorganic thin film photovoltaic, mostly due to their advantageous properties: large absorption coefficient (e.g. of  $\sim 10^5 \text{ cm}^{-1}$

## 2. THEORETICAL BACKGROUND

---

at 500 nm for  $\text{CuInS}_2$ ), low bandgap ( $\sim 1.05\text{eV}$  for  $\text{CuInSe}_2$ ), and good radiation stability [29]. This nanomaterial, consisting of three components, is more complicated: not only the quantum size effect, but also the stoichiometry influences its properties. Taking into account that Cu-rich nanoparticles are a semiconductor of n-type, while In-rich NPs belong to p-type, bringing them together might lead to a bulk heterojunction. That might be interesting for photovoltaic applications. Finally, it is a nontoxic material, in contrast to the heavy metal compounds. That makes them attractive for biological applications. Their emission can be tuned in the NIR spectral region and its quantum yield can be improved by an appropriate shell. For example  $\text{CuInS}_2/\text{ZnS}$  core/shell NPs have been already employed in the biological research [30].

Oxide nanomaterials are indispensable for nanotechnological innovations, because they combine an infinite variety of structures and properties [2]. This is illustrated with a few examples. By magnetic oxide nanoparticles the targeting of tumors is developing, that raises new therapeutic hopes in the nanomedicine [31]. The catalytic and sensing functions of oxide nanomaterials are also very useful for the photocatalytic recycling of waste water or personalized nanosensors for the detection of health and atmospheric hazards. Additionally, these materials are used for hydrogen-based energy technologies, and miniaturized energy storage. In particular, the optical properties of ZnO or  $\text{TiO}_2$  nanoparticles are used in cosmetics for suncreening [1]. These particles are transparent for visible light and serve as protection from UV radiation. Other transition metal oxides find application in white pigments, electronic ceramics, and supports in catalysis [2, 3, 9]. Transparent conducting oxides (e.g. Indium tin oxide  $\text{In}_2\text{O}_3:\text{Sn}$ , ITO) belong to thin film electrodes, which are applied in solar cells (see figure 2.6(a)), flat panel display, thin film transistors [1, 32]. In such fields the vast surface area plays an important role. Compared to the bulk, devices consisting out of nanoparticles own better efficiencies, in particular in indium oxide nanoparticle sensors [33, 34].

Indium oxide ( $\text{In}_2\text{O}_3$ ) belongs to the class of n-type transparent semiconductors with high charge carrier mobility [35]. It has a wide direct band gap of about 3.6 eV [36], a high transparency to visible light [37], a relatively low electron affinity, and a high chemical inertness [38]. Besides its application in solar cells,  $\text{Cr}^{3+}$ -,  $\text{Mn}^{3+}$ -,  $\text{Fe}^{3+}$ -doped  $\text{In}_2\text{O}_3$  are ferromagnetic at room temperature [39]. Since its electrical conductance is changed upon exposure to gases [37], this material is used in gas detectors, which

## 2.1 Nanomaterials, their properties and application

shows high sensitivity for toxic and explosive gases already at low temperatures [40]. The sensitivity depends on the surface area, thus sensors using  $\text{In}_2\text{O}_3$  nanocrystals might exhibit superior performance.

### 2.1.1 Hybrid nanomaterials

The next step towards the properties modification of nanomaterials is the combination of different nanoparticles together. That promises new properties and provides novel building blocks for the application. Nanoparticles consisting of different materials in one

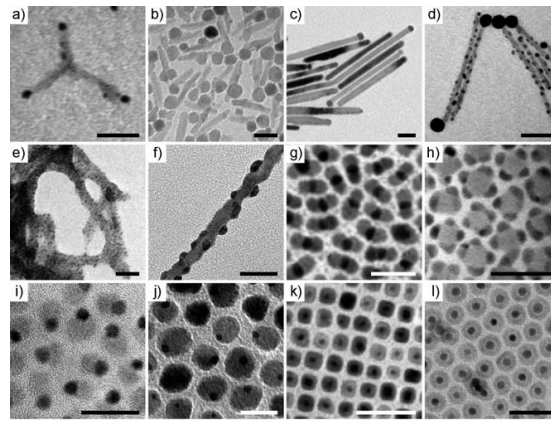


**Figure 2.7: TEM images of hybrid materials** - a) CdSe/Au, b)  $\text{TiO}_2/\text{Fe}_2\text{O}_3$ , c) Co/Au, d) CdS/Au, e) CdSe/Pt, f) PbSe/Au, g) Au/PbS, h) PbS/Au, i) CdS/FePt, j) Au/ $\text{Fe}_3\text{O}_4$ , k)  $\text{Fe}_3\text{O}_4/\text{Au}$ , l) Au/hollow iron oxide nanocrystals. All scale bars: 25 nm (modified reproduction from [10]).

common structure are called hybrid nanoparticles [10]. In figure 2.7 different hybrid nanostructures are shown. These are combinations of semiconductor and metallic, metallic and magnetic as well as magnetic and semiconductor nanoparticles. Such nanostructures display modified properties compared to the single components, such as retaining of the original properties of both materials but with achieving of some novel combination in one common nanoparticle system or a strong change of the properties of one material due to the presence of a second material [10].

In the case of semiconductor-metal materials, the electronic properties of each component change. When a semiconductor comes in contact with a metal surface it undergoes Fermi level equilibration (figure 2.8). In bulk systems, such an interface is characterized by the space-charge region and the corresponding Schottky barrier [10]. In

## 2. THEORETICAL BACKGROUND

---

the semiconductor nanocrystal the electrons are confined and the individual nanocrystal remains isoenergetic. Due to such size limitation the bands remain flat and the charge separation is essentially dictated by the Fermi level equilibration [41]. Metal

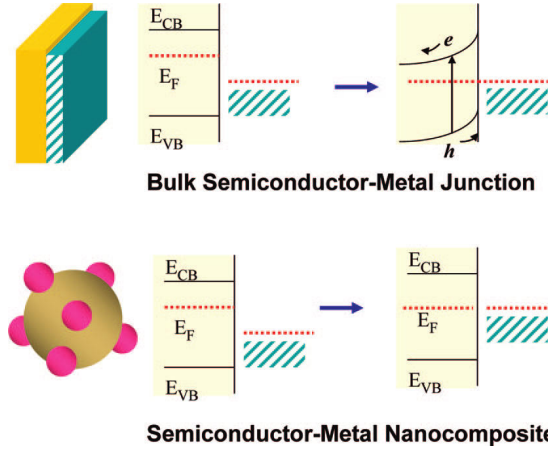


**Figure 2.8: Electronic properties of hybrid materials - Bulk and nanoparticle junction** (taken from [41]).

nanoparticles possess the property of storing electrons in a quantized fashion. When the semiconductor and metal nanoparticles are in contact, the photogenerated electrons are distributed between the semiconductor and metal nanoparticles. Since the electron accumulation increases the Fermi level of the metal to more negative potentials, the resultant Fermi level of the composite shifts closer to the conduction band of the semiconductor [41].

As a result, the optical properties, such as the absorption and the photoluminescence of metal-semiconductor nanoparticles are different from the sum of the spectra from each component [42, 43]. An interesting possibility for application is based on the charge separation in the hybrid nanoparticles. This process is of great importance in photovoltaics and photocatalysis [41]. Metal-semiconductor hybrid nanoparticles lead to a significant progress in nanoelectronics, because the metallic part serves as an electrical contact and as well enables self-organization [44].

In summary, the physical and chemical properties of nanoparticles strongly depend on their size and shape as well as surface and material. Controlling these parameters opens the possibility to control the properties of material, which are of strong interest with respect to further application.

## 2.2 Theory of nanocrystal synthesis

Synthesis of monodisperse nanoparticles (with a size distribution  $\sigma_r \leq 5\%$ ) is of great importance not only because of scientific interest, but also for the technological applications [9]. The uniformity of the synthesis product is crucial for its further characterization and application, because of the strong size- and shape-dependence of the NP properties. A variation of the reaction conditions influences the nanoparticle parameters such as size, shape, and surface, that enables controlled tuning of nanoparticle properties. So the synthesis is responsible for the quality of the nanoparticles. Understanding the formation mechanism of monodisperse nanocrystals is important because it will help us to develop improved synthetic methods that can be generally applicable to various kinds of materials.

All the nanoparticle synthetic methods can be classified into two different approaches: the "top-down" and the "bottom-up" approach. The first one consists of physical methods carried out by the comminution of the bulk materials until the nanometer size. The second one is based on the construction of the nanomaterials out of atoms and molecules, which includes solution-phase colloidal chemistry. The advantage of the "bottom-up" synthetic methods is the ability to better control the nanoparticle parameters [9].

### 2.2.1 Impact of experimental conditions

In the synthesis of colloidal nanoparticles several experimental conditions come into play to manipulate their size and morphology, such as the choice of precursors, stabilizers, temperature and other. Figure 2.9 shows a scheme of a typical colloidal synthesis, employed precursors which consists out of the elements for future particles, the solvent which brings them together for reaction, and the ligands which stabilize the nanoparticles and thus prevent their growth to bulk material as well as their agglomeration. Thus, as-prepared nanoparticles have always a "shell" providing the steric stabilization, consisting out of long-chain organic molecules like phosphines, amines, organic acids, and thiols (figure 2.9). Their impact on the nanoparticle formation often determines the properties of resulting product.

The formation of nanocrystals can be divided into two stages: the nucleation (a process which creates the "seeds" for the crystal growth) and the growth. The ligands

## 2. THEORETICAL BACKGROUND

---

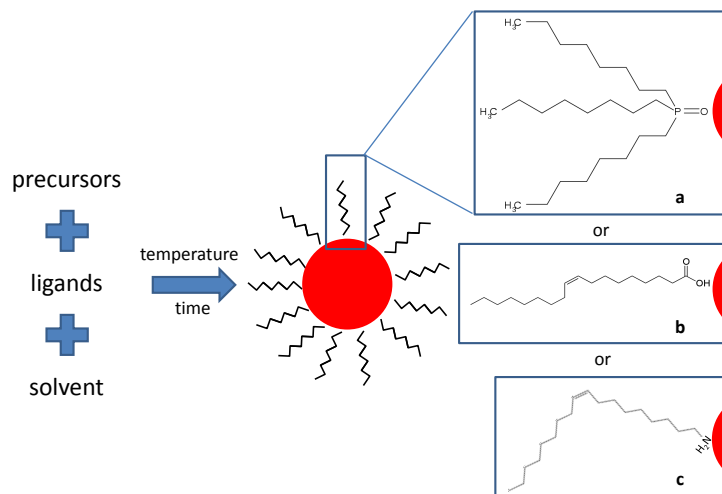


**Figure 2.9: Scheme of nanoparticle synthesis** - The main components of synthesis, resulting nanoparticle covered by organic ligands such as TOPO (a), oleic acid (b), or oleylamine (c) as an example.

play an important role in each stage. They influence the activity of the "monomer" (reactive molecular species) in the nucleation stage. Yu et al. [45] described this as an interplay of three effects. First, a strong coordination bond between ligands and monomers will decrease the reactivity of monomers. As a result, a small amount of monomers will be consumed in the nucleation stage and, thus, a small amount of nuclei will be formed. Next, ligands with longer hydrocarbon chains will reduce the reactivity of monomers. Finally, a high ligand concentration will suppress the monomer reactivity. The last two effects are caused by steric factors. The reaction temperature influences also the stability and configuration of complexes on the nucleation stage.

During the growth stage the ligands can affect the shape of the nanocrystals. The elongated nanocrystals need a high monomer activity and a high remaining concentration of monomers, but a low nuclei concentration. The latter can only be achieved by the use of low activity monomers. Thus, the solution of this contradiction can be the choice of monomers with the medium level of activity, or the use of several different ligands.

Some stabilizers can be used also as a solvents. They are called coordinating solvents (e.g. oleylamine). Sometimes a good choice is the use of a stabilizer being not a

solvent and a non-coordinating solvent (e.g. 1-octadecene). The last will only be the medium, should exhibit low reactivity to other reaction components as well as dissolve the compounds, and be suitable for the reaction temperatures.

The nanoparticles grow with time. When they reach the desired size, the reaction can be stopped through cooling of the reaction vessel or through separation of nanoparticles from the solution. That can be carried out by centrifugation with a suitable solvent. The nanoparticles covered with ligands precipitate, while the by-products, unreacted starting materials, excess of stabilizers and the solvent remain in the supernatant. After the synthesis and the following cleaning of the nanoparticles, they can be treated for the further application. For example, the surface properties can be changed through a ligand exchange [46].

In summary, by optimization of the synthesis route through the variation of the reaction conditions described above, materials of high quality can be produced.

### 2.2.2 Formation mechanism of spherical nanoparticles

The nanoparticle formation takes place in two steps: nucleation and growth stage. The theoretical description of this process dates back to investigations of LaMer and Dinegar [47, 48] who proposed the "burst nucleation" concept, which based on simultaneous generation of nuclei followed by their growth. In other words, the nucleation and growth stages must be separated, so that the generated nuclei will grow under equal conditions and without additional nucleation [9]. This is essential to control the nanoparticle size distribution.

The LaMer-diagram (figure 2.10) demonstrates the nanoparticle formation process with homogeneous nucleation which occurs in absence of any foreign particles or ions (in contrast to heterogeneous nucleation) [9]. As a first step (I) the increase of the monomer concentration is illustrated. Due to the decomposition of the precursors during the reaction, the solution becomes supersaturated ( $S > 1$ ), but that is not enough for nucleation. In the case of homogeneous nucleation, the system changes from the homogeneous to the heterogeneous phase. Such transition has a high energy barrier [49]. So, the supersaturation is expected to reach a critical value ( $S = S_c$ ) to overcome the energy barrier for nucleation. Next, the nucleation takes place (step II), caused the consumption of monomers. Their concentration decreases. In step III the growth stage occurs.

## 2. THEORETICAL BACKGROUND

---

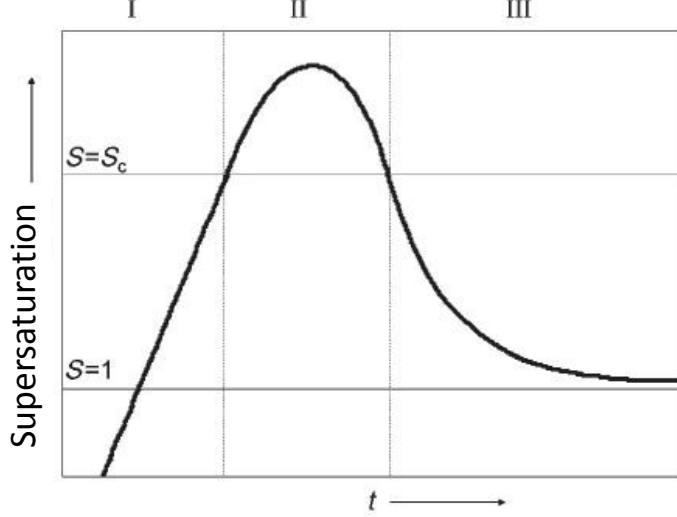


**Figure 2.10: LaMer-diagram** - Degree of supersaturation changes with time (taken from [9]).

In this case, only the growth of the generated nuclei is responsible for the monomer consumption. The nanoparticles grow as long as the solution is supersaturated.

### Nucleation stage

The nucleation is a thermodynamic process taking place when the solution is supersaturated. The change of free energy during the process of homogeneous nucleation is interpreted as follows:

$$\Delta G = \Delta G_S + \Delta G_V = 4\pi r^2 \gamma + \frac{4}{3}\pi r^3 \Delta G_\nu, \quad (2.6)$$

where  $\Delta G$  is the Gibbs free energy of spherical crystal formation with the sphere radius  $r$ ,  $\Delta G_S$  the surface free energy,  $\Delta G_V$  the volume free energy,  $\gamma$  the surface free energy per unit area,  $\Delta G_\nu$  the free energy change between the monomers in the solution and unit volume of bulk crystal. The first term ( $\Delta G_S$ ) is always positive (because  $\gamma > 0$  [9]). The second term ( $\Delta G_V$ ) is negative in a supersaturated solution, because:

$$\Delta G_\nu = \frac{-RT \ln S}{V_m} < 0, \quad (2.7)$$

where  $R$  is the gas constant,  $T$  temperature,  $S$  supersaturation,  $V_m$  the molar volume of the bulk crystal. Since the two terms on the right hand side of equation (2.6) have



opposite sign and both depend on  $r$ , a plot of  $\Delta G$  versus  $r$  has a maximum (figure 2.11). The value of  $r$  at which  $\Delta G$  is at maximum is the minimum radius of a nucleus

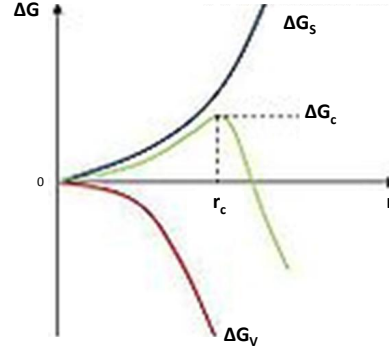


**Figure 2.11: Free energy diagram** - Explanation of the nucleation [50].

that can grow spontaneously in the supersaturated solution (called the critical radius  $r_c$  [9]). This can be determined as follows:

$$\frac{d\Delta G}{dr} = 8\pi r\gamma + 4\pi r^2\Delta G_v = 0, \quad (2.8)$$

therefore

$$r_c = \frac{-2\gamma}{\Delta G_v} = \frac{2\gamma V_m}{RT \ln(S)}. \quad (2.9)$$

Equation (2.9) is the first necessary condition for supersaturation with homogeneous nucleation. The particles smaller than  $r_c$  will dissolve, while the particles bigger than  $r_c$  will grow to reduce free energy. With increasing the supersaturation  $S$ , the critical radius  $r_c$  decreases, thus smaller particles (with  $r \geq r_c$ ) will grow. Equations (2.6) and (2.9) give the critical free energy  $\Delta G_c$ , which is the free energy necessary to form a stable nucleus:

$$\Delta G_c = \frac{16\pi\gamma^3}{3\Delta G_v^2} = \frac{16\pi\gamma^3 V_m^2}{3(RT \ln S)^2}. \quad (2.10)$$

If the rate of increase of the particle number  $N$  is defined as the rate of nucleation, it can be written in the Arrhenius form in terms of  $\Delta G_c$  [9].

$$\frac{dN}{dt} = A \exp\left(-\frac{\Delta G_c}{kT}\right) = A \exp\left(-\frac{16\pi\gamma^3 V_m^2}{3k^3 T^3 N_A^2 (\ln S)^2}\right), \quad (2.11)$$

## 2. THEORETICAL BACKGROUND

---

where  $k = R/N_A$  is the Boltzmann constant,  $N_A$  the Avogadro constant, and  $A$  the pre-exponential factor. Thus,

$$\ln(S) = \sqrt{\frac{16\pi\gamma^3V_m^2}{3k^3T^3 \ln(A/N_t)}}, \quad (2.12)$$

where  $N_t = dN/dt$ . Equation (2.12) is another necessary condition for degree of supersaturation. The nuclei can form or dissolve generally at each concentration, but at high supersaturation the nuclei generation occurs faster than their dissolution.

In the calculations demonstrated above the two parameters  $\gamma$  and  $\Delta G_v$  are assumed to be constant, but they are strongly size-dependent in the case of nanoparticles [51]. Thus, such thermodynamic model has some limitations with respect to nanocrystals.

### Separation between nucleation and growth

There are several synthetic techniques for the separation of nucleation and growth stages. In the heterogeneous nucleation the seed-mediated growth method is used [9]. In this case, previously prepared nuclei are introduced as seeds into the reaction. The monomers precipitate on the nuclei surface. To avoid the homogeneous nucleation the monomer concentration is kept low during growth. So, nucleation is physically separated from growth. Note that the seeds need to be of high quality to produce monodisperse nanocrystals. This method can be used for the preparation of homogeneous particles [52] as well as heterogeneous structures [43] (The details are described in the section 2.2.4).

For the homogeneous nucleation there are two techniques for the separation of nucleation and growth of nanoparticles in the organic solutions [9]: "hot-injection" [53] and "heating-up" [54] methods. In the case of the hot-injection technique the supersaturation is achieved through the fast injection of solution with one precursor into the solution with another precursor at high temperature. During the nucleation the monomer concentration decreases dramatically. Then the growth follows. The biggest hindrance of this method, particularly for the industrial use, is the high temperature [9].

In the heating-up methods all reaction components are mixed at the beginning and heated until a certain temperature. The starting materials begin to decompose. The monomer concentration increases until the supersaturation of the solution is enough for

nucleation. In other words, the decomposition of the precursor species induces a short burst of nucleation, which is subsequently followed by growth of the initially formed seeds [55]. The size distribution of as-prepared nanoparticles is often comparable to the ones obtained by the hot-injection method [56]. This method is advantageous for large-scale production, because it is simple and provides a high yield.

### Growth stage

For an isolated particle dispersed in a homogeneous solution of monomer, growth takes place in two steps: diffusion of monomers to the particle surface and the reaction or dissolution of these monomers [57]. The first theoretical model "Growth by diffusion" proposed by Reiss [58] describes the dependence of the growth rate ( $dr/dt$ ) of spherical particles on the flux of the monomers supplied to the particles ( $J$ ) [9]:

$$J = \frac{4\pi r^2}{V_m} \frac{dr}{dt} \quad (2.13)$$

When each particle is treated independently, a consequence is the existence of a concentration gradient around the particle which allows the use of Fick's law which describes the flux  $J$  of the monomers diffusing through the surface of a sphere enclosing the particle:

$$J = 4\pi x^2 D \frac{dC}{dx}, \quad (2.14)$$

where  $D$  is the diffusion coefficient,  $C$  is the concentration, and  $x(\geq r)$  is the distance from the center of the particle. The boundary conditions for the integration of equation (2.14) are that at  $x = \infty$  the concentration of monomer is equal to the value in the bulk solution ( $C = C_{bulk}$ ) and that at  $x = r$  the concentration of the monomer is equal to the interfacial concentration ( $C = C_s$ ). Also, under steady-state conditions  $J$  is a constant independent of  $x$ . After the integration, the flux of a monomer to the surface of the particle is interpreted as following [57]:

$$J = 4\pi r D (C_{bulk} - C_s). \quad (2.15)$$

Equation (2.16) follows from equations (2.13) and (2.15):

$$\frac{dr}{dt} = \frac{V_m D}{r} (C_{bulk} - C_s). \quad (2.16)$$

Therefore, the smaller nanoparticle is, the faster it grows, when the  $C_{bulk}$  and  $C_s$  are constant for all particles.

## 2. THEORETICAL BACKGROUND

---

On the second step of the growth stage the monomers reaching the particle through diffusion may react with the particle (become incorporated into the lattice) or desorb from the particle (particle dissolution) [57], that can be explained in terms of the Gibbs-Thomson effect. The change in chemical potential of a spherical crystal with a radius  $r$  with respect to that of the bulk crystal can be described by the Gibbs-Thomson equation [9]:

$$\Delta\mu = \frac{2\gamma V_m}{r}. \quad (2.17)$$

The assess of the chemical potential change ( $\Delta\mu$ ) on the precipitation and dissolution reactions with the reaction rate constants  $k_p$  and  $k_d$ , respectively is expressed through equations (2.18) and (2.19):

$$k_p = k_p^\circ \exp\left(-\alpha \frac{\Delta\mu}{RT}\right) = k_p^\circ \exp\left(-\alpha \frac{2\gamma V_m}{rRT}\right), \quad (2.18)$$

$$k_d = k_d^\circ \exp\left((1-\alpha) \frac{\Delta\mu}{RT}\right) = k_d^\circ \exp\left((1-\alpha) \frac{2\gamma V_m}{rRT}\right), \quad (2.19)$$

where  $\alpha$  is the transfer coefficient and  $k^\circ$  is the rate constant for the bulk crystal ( $r = \infty$ ). Thus, the small particles have a high chemical potential, so they dissolve easier. That contradicts the Reiss model [9].

For combination of this effect and the model of Reiss, the assumption of  $C_s$  to be constant for all particles should be changed. In this case, the fluxes of the monomers toward the surface of a particle by precipitation and dissolution ( $J_p$  and  $J_d$ , respectively) as well as the net flux  $J$  are given by equations (2.20), (2.21), and (2.22).

$$J_p = 4\pi r^2 k_p^\circ C_s \exp\left(-\alpha \frac{2\gamma V_m}{rRT}\right), \quad (2.20)$$

$$J_d = -4\pi r^2 k_d^\circ \exp\left((1-\alpha) \frac{2\gamma V_m}{rRT}\right), \quad (2.21)$$

$$J = J_p + J_d = 4\pi r^2 k_p^\circ C_s \exp\left(-\alpha \frac{2\gamma V_m}{rRT}\right) - 4\pi r^2 k_d^\circ \exp\left((1-\alpha) \frac{2\gamma V_m}{rRT}\right). \quad (2.22)$$

Taking into account equation (2.15),  $C_s$  can be determined as following:

$$C_s = \frac{k_d^\circ r \exp\left((1-\alpha) \frac{2\gamma V_m}{rRT}\right) + DC_{bulk}}{k_p^\circ r \exp\left(-\alpha \frac{2\gamma V_m}{rRT}\right) + D}. \quad (2.23)$$

Then, to consider both the mass transport and the reaction kinetics the equation (2.16) combined with equation (2.23) results in equation (2.24):

$$dr/dt = V_m D C_{s,eq}^{\circ} \frac{S - \exp(2\gamma V_m / rRT)}{r + (D/k_p^{\circ}) \exp(\alpha 2\gamma V_m / rRT)}, \quad (2.24)$$

where  $C_{s,eq}^{\circ}$  is the equilibrium surface concentration of the bulk crystal ( $r \rightarrow \infty$ ).

### Simulation of nucleation and growth processes

To understand the processes of nucleation, growth, and their separation, these stages of nanoparticle formation were simulated. The homogeneous nucleation was simulated by using a numerical method similar to that reported by De Smet et al. [59]. The values of parameters in this simulation fitted the typical experimental conditions used to synthesize CdSe nanocrystals. In particular, the nucleation rate was calculated from equation (2.11), where  $V_m = 3.29 \times 10^{-5} m^3 mol^{-1}$  [9]. Other parameters (S, T,  $\gamma$ , A) were varied for different simulations. In the case with constant temperature (T = 523K) and high beginning supersaturation (S = 100), the particle concentration increases rapidly during the first two seconds. These generated nuclei grew fast. That consumed the monomers in solution and the supersaturation of the solution rapidly fell. Therefore, the nucleation process stops within the next second. The time evolutions of the particle concentration for various levels of initial supersaturation, temperature, and surface free energy values were also simulated. The increase of the initial supersaturation, the temperature and the decrease of the surface free energy lead to an increase of the maximum particle concentration and a decrease of the time required to reach this maximum [9].

A numerical simulation of the time evolution of the particle size in an ensemble applying the Monte Carlo method was demonstrated by Talapin et al. [60]. The growth rate for an individual particle was calculated from equation (2.24). Analysis of the particle size distribution during the time revealed two steps in the growth process [9]. In the first step the supersaturated solution facilitates the rapid growth of the particles and the size distribution narrows down. That is the "focusing of size distribution". In the second step, the supersaturation is low, so the growth rate declines sharply and the size distribution broadens. That is the "defocusing". In this period, Ostwald ripening occurs. Smaller particles dissolve and larger particles grow by receiving the monomers

## 2. THEORETICAL BACKGROUND

---

from the dissolving particles. This process leads to a broad size distribution and should therefore be avoided.

The good resemblance between these simulations and the experimental results [9] shows the validity of the theoretical model.

### 2.2.3 Shape control of nanoparticles

As it was described above the properties of nanoparticles depend also on their shape. Therefore, shape control of nanoparticles during the synthesis is an important research area. Inorganic bulk materials crystallize in material-specific crystal lattices, what determine the shape of the crystals. In the case of nanoparticles, due to their large surface to volume ratio the resulting shape depends directly on the surface with the material-specific facets and their energies.

The shape of the nanoparticles can be influenced already in the nucleation stage. The crystallographic structure of the nuclei determines the following nanoparticle growth. For materials, which can crystallize in different phases, the crystal structure of nuclei can be controlled by changing of the reaction temperature [61, 62, 63]. For example, cadmium sulfide crystallizes at low temperatures in the wurtzite structure, facilitating formation of rod-shaped particles, but at high temperatures the zincblende structure occurs, which determines branched particles [64].

In the growth stage the surface energy of the generated nuclei is crucial. The different facets have different energy. The energy-rich facets grow faster [65]. In this case, control is possible, when the stabilizers can adsorb only on certain facets on the nanoparticle surface [66, 67, 68, 69]. That slows down the growth rate of this facet [70]. The variation of the stabilizer concentration lead to divers shapes [71]. CdSe nanorods can be synthesized in the presence of hexylphosphonic acid, because of its selective adhesion on several facets, that facilitate the growth of rods. In the absence of this stabilizer, the CdSe NCs become spherical-shaped [6]. Besides employing different stabilizers, the monomer concentration and the growth temperature are also significant reaction parameters for the shape control. The high temperature and low monomer concentration are responsible for the thermodynamic control. The thermodynamic product is generally a stable isotropic structure. In contrast, the kinetic control involves low temperature and high monomer concentration [3]. For example the PbS nanorods can be synthesized using a kinetic control, while truncated cubes occur due to the

thermodynamic control [72]. That is shown in the energy diagram of the PbS growth process (figure 2.12(a,b)). The thermodynamic growth is realizable with excess thermal energy. The shape control by the diffusion flux of monomers was proposed for CdSe

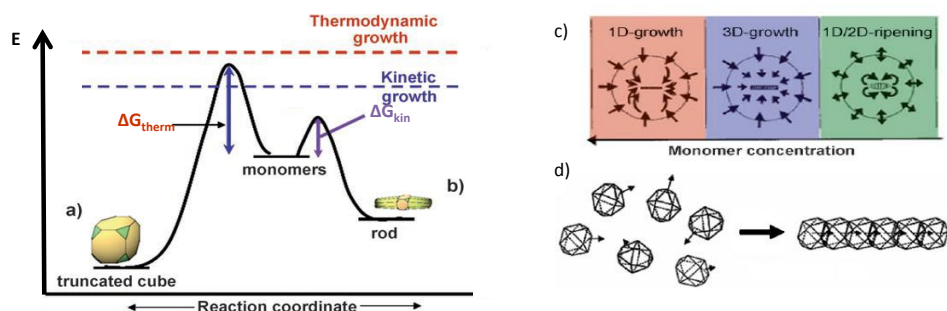


**Figure 2.12: Shape control** - a) Thermodynamic and b) kinetic control for PbS NCs, c) influence of the monomer concentration on the shape of CdSe nanocrystals, d) oriented attachment: the initial 0D nanocrystals come together along their dipole direction (modified reproduction from [3]).

NCs [73]. A high diffusion flux of monomers into the diffusion layer facilitates the 1D growth of monomers on the highest energy surface of the CdSe nanocrystal (figure 2.12 (c)). A lower monomer concentration promotes a 3D growth of the nanocrystals. With a further decrease of the diffusion flux the system reaches an equilibrium by dissolution and re-growth of the monomers from the face with highest energy onto other faces (the 1D to 2D ripening stage). At low monomer concentrations, the nanocrystals grow by an interparticular Ostwald ripening process [3].

After the formation of the nanocrystals their agglomeration can occur, in order to minimize the surface energy. Besides uncontrolled agglomeration which is usually avoided, self-assembly (figure 2.12(c)) leads to various structures (e.g. nanowires, zigzags, helices, branches, and rings [74, 75]). The concept of "oriented attachment" was proposed by Banfield et al. [74] for  $\text{TiO}_2$  nanocrystals which formed necklace-shaped nanocrystals, when there is a sufficient thermal energy in the system.

In summary, the nanoparticles appear in different shapes, either due to the minimization of surface energy or because of the growth kinetics. The final shape of nanoparticles is determined by the following parameters: the crystallographic phase of the nuclei, the surface energy, the growth rate, surface-specific molecules as well as the temperature, that can be controlled during the synthesis [3].

## 2. THEORETICAL BACKGROUND

---

### 2.2.4 Synthesis of hybrid nanostructures

As it was shown above the hybrid nanoparticles are more complicated nanostructures consisting out of two or more different materials (figure 2.7). Thus, the synthesis of such nanostructures requires the combination of these different materials into one system. This is a challenge for colloidal synthesis, because the chemical and structural compatibility between the different components is generally not expected [10].

An already mentioned synthesis technique, the seed-mediated method, is widely applied for the synthesis of hybrid nanostructures. The pre-existed nanocrystals ("seeds") serve as centers for accommodating a secondary material upon reaction of its precursor. The energy barrier for this heterogeneous nucleation of a second phase onto a seed particle ( $\Delta G_{het}^*$ ) is lower than the activation energy for homogeneous nucleation of a given material ( $\Delta G_{hom}^*$ ) [76]:

$$\Delta G_{het}^* = f(\Theta)\Delta G_{hom}^*, \quad (2.25)$$

where  $f(\Theta)$  ( $0 < f(\Theta) < 1$ ) is the function depending on the system geometry. The barrier for the growth of the domain nucleated heterogeneously is much lower than both  $\Delta G_{hom}^*$  and  $\Delta G_{het}^*$  [76].

The required chemical potential of the solution monomer for heterogeneous nucleation ( $\Delta\mu_{het}$ ) is smaller in comparison to the homogeneous nucleation ( $\Delta\mu_{hom}$ ):

$$\Delta\mu_{het} < \Delta\mu_{hom}. \quad (2.26)$$

The creation of the inorganic interface between two materials [76] can be thermodynamically described as follows:

$$\Delta G_S = \gamma_1 - \gamma_2 + \gamma_{1,2}, \quad (2.27)$$

where  $\Delta G_S$  is total Gibbs free surface energy change function,  $\gamma_1$  and  $\gamma_2$  are the solid/solution interfacial energies associated with pre-existing one material (seeds) and the second material growing onto its surface, respectively,  $\gamma_{1,2}$  is the solid/solid interfacial energy. The latter depends on the degree of crystallographic compatibility between the two materials and their bonding strength. The other two terms ( $\gamma_1$  and  $\gamma_2$ ) can be changed by the use of various ligands or monomers. In figure 2.13 the hybrid nanoparticle formation possibilities are presented together with the sketch of formation



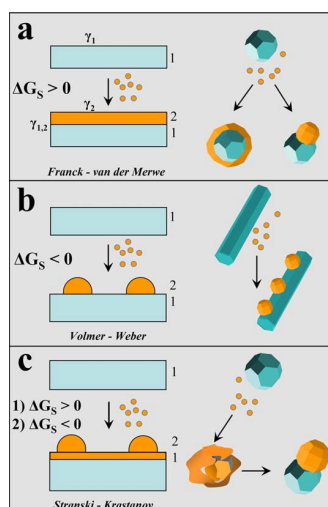


**Figure 2.13: A scheme illustrating heterogeneous deposition modes for material "2" from its precursor onto a seed substrate of material "1" - a) Franck - van der Merwe mode; b) Volmer - Weber mode; c) Stranski - Krastanov regime (taken from [76]).**

of thin-film heterostructures onto substrates. Heterogeneous deposition on a highly faceted NC seed ( $\gamma_2 < \gamma_1$ ) can lead to a continuous shell (core-shell hybrid nanostructures) or can develop into a discrete section (heterodimers of NCs) (figure 2.13a). On the other hand, if  $\gamma_2 > \gamma_1$ , multiple domains of the foreign material occur (figure 2.13b). A transformation from a metastable core-shell architecture to a heterodimer heterostructure could occur as an intermediate case (figure 2.13c).

The influence of the reaction parameters might complicate the mechanism described. Examples for the interplay of such processes are described in Chapter 6.

## 2.3 Characterization methods

### 2.3.1 Electron microscopy

The most common electronic characterization methods are scanning electron microscopy (SEM) and transmission electron microscopy (TEM) [77]. They are based on the interaction of electrons with specimen, what causes secondary effects, which can be detected. These instruments are usually coupled to other types of analytical tools, such as energy-dispersive x-ray analysis (EDX). The SEM analytical value includes raster imaging, topology, and morphology. Since the TEM is able to analyze extremely small

## 2. THEORETICAL BACKGROUND

---

particles, this method is the most significant to nanoscience.

### Transmission electron microscopy

TEM allows imaging of nanoparticles, determination of their shape and size as well as statistical analysis of the size and shape distribution of nanoparticles. The high resolution of this instrument originates from its high-energy electron beam.

An electron gun (figure 2.14) produces the electrons and accelerates them. The electron beam passes through a condenser lens system and is focused on the sample which needs to be thin to be transparent for the beam. As a result of the interaction

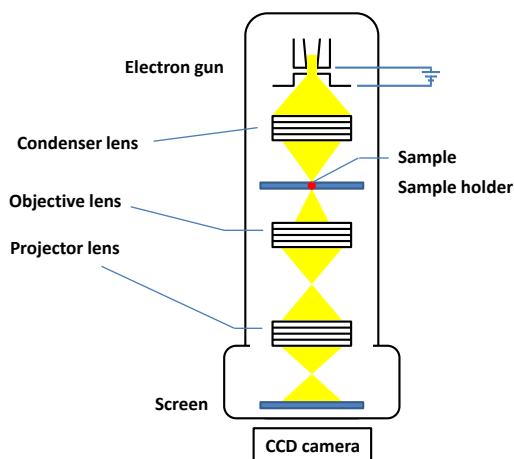


**Figure 2.14:** A schematic representation of transmission electron microscope - The resolving power of such instruments is in the range of 0.05 nm (modified reproduction from [77]).

between the electron beam and the sample, several effects are observed, such as transmission of electrons through the material, or their scattering as well as the emission of characteristic x-rays. Transmitted electrons are focused by an objective lens and projected by a projector lens onto the screen. A CCD (charge-coupled device) camera captures the image.

Besides the characteristic x-rays used by the EDX analysis which will be described below, the other secondary effects can also be used to gain additional information about nanoparticles. Elastically scattered electrons (deflected with no loss of energy) can be

used for generating electron diffraction patterns, which carry informations on crystal structure and orientation of the sample. Inelastically scattered electrons lose energy by interactions with the sample. This electron loss value is typical for each element. This effect is used by electron energy loss spectroscopy (EELS), which provides information on elemental composition of nanomaterial. For such additional measurements, TEMs are often equipped with special detectors [78].

Although this characterization method has several limitations (e.g. altering of the sample under exposure of electrons, or costliness of operation and maintenance of high-vacuum system), the high resolution and the ability to image any type of sample (electrically insulating, semiconducting, conducting) make TEM important for nanoscience.

### 2.3.2 X-ray characterization methods

X-ray techniques are another nanorelevant analysis, such as x-ray diffraction (XRD) which is used for gaining structural information and energy-dispersive x-ray (EDX) which is applied for chemical analysis.

#### X-ray diffraction

X-ray diffraction (XRD) is used to obtain information about the structure of crystalline materials. Atoms in the crystal are configured in regular arrays. The spacing between atoms and planes of atoms is in the order of the wavelength of the x-rays. Thus, the result of scattered x-rays from atoms is diffraction, which is described by Bragg's law:

$$n\lambda = 2d \sin \Theta, \quad (2.28)$$

where  $\lambda$  is the incident wavelength of x-rays,  $d$  is the spacing between the planes in the atomic lattice,  $\Theta$  is the angle between the incident waves and the scattering planes, and  $n$  is an integer (figure 2.15(a)).

The x-ray diffraction of a sample results in a pattern characterized by reflections (peaks in intensity) at certain positions. Besides the crystalline structure, these XRD data can provide information about crystallite size using the Debye-Scherrer equation [79]:

$$d = \frac{40,9\lambda}{3 B \cos \Theta}, \quad (2.29)$$

## 2. THEORETICAL BACKGROUND

---

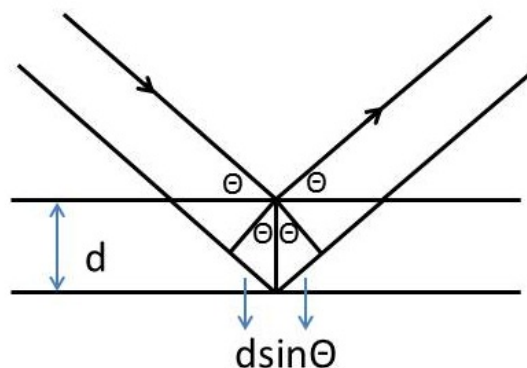


**Figure 2.15: X-ray diffraction - Bragg's law explaining.**

where  $d$  is the diameter of the crystallite,  $\lambda$  is the wavelength of the x-rays,  $B$  is the full width at half maximum of the peak, and  $\Theta$  is the is the Bragg's angle of diffraction. If the sample is nanocrystalline, the reflections of its XRD pattern will be broadened. However the width of the reflections can be determined not only by the crystallite size, but also by deformations of the lattice. To consider that, an analysis of the XRD data called Rietveld refinement is used. The Rietveld method is applied to refine a theoretical line profile until it matches the measured profile including the height, width and position of the reflections in XRD pattern.

### **Energy dispersive X-ray spectroscopy**

The energy dispersive x-ray spectroscopy enables elemental analysis of materials based on the detection of X-rays emitted by the sample after being hit by an electron beam. In particular, such interaction causes electron vacancies, which will be filled by an electron with higher energy (figure 2.16). As a result x-rays are emitted [77], which are specific for each element. So, EDX spectroscopy is used for the elemental qualitative and quantitative analysis of the material: The spectra deliver the elements present in the sample as well as their ratio. This method is very important especially for materials consisting of more than one element (e.g. ternary or quaternary CIS NPs [80]), and also hybrid nanomaterials. When the EDX detector is coupled with a high-resolution transmission electron microscope (HRTEM), the element composition of a single particle can be measured, in particular the element distribution in one particle, or the proof of core/shell particle formation.

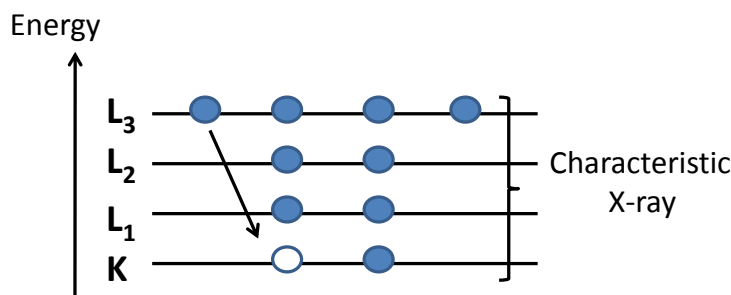


Figure 2.16: Energy dispersive X-ray spectroscopy - Working principle.

### 2.3.3 Optical studies

Ultraviolet-visible (200-800nm) and near-infrared (800-2500 nm) spectroscopy are the most familiar types of spectroscopic characterization methods, which base on absorption or emission of photons and mainly involve electron transitions.

#### Ultraviolet-visible and near-infrared absorption spectroscopy

As it was described above (Chapter 2.1) the semiconductor nanoparticles exhibit size-dependent optical properties (figure 2.3). Thus, the absorption spectroscopy is an extremely relevant method for the characterization of nanomaterials. By the interaction of nanocrystals with photons, the light can be transmitted, absorbed, or reflected. By absorption of the photon, the electron transition from HOMO (highest occupied molecular orbitals) to LUMO (lowest unoccupied molecular orbitals) can occur [81]. So, the band gap can be directly measured. The data plots, generally shown as absorbance versus wavelength, reveal information concerning the size of nanoparticles (according to the position of maximum absorption) as well as size distribution (according to the peak width or even the appearance of several peaks). In the study of the nanoparticle formation mechanism (Chapter 2.2), the information about the nanoparticle concentration was determined from the absorption spectra [9], using the Beer-Lambert law:

$$A = -\lg \frac{I}{I_0} = \epsilon cd, \quad (2.30)$$

where  $A$  is the optical density,  $I$  is the intensity of light after interaction with the sample,  $I_0$  is the intensity of the incident light,  $\epsilon$  is the molar absorptivity ( $\text{L}\cdot\text{mol}^{-1}\cdot\text{cm}^{-1}$ ),  $c$

## 2. THEORETICAL BACKGROUND

---

is the concentration of the compound in the solution, and  $d$  is the path length of the sample (cm) [81].

### Photoluminescence spectroscopy

Photoluminescence (PL) is the emission of photons from a material after its excitation by light. By the excitation the electron transfers from its ground state to an excited state. Then this electron falls back to the ground state, causing the light emission. The energy of this light corresponds to the difference of the energy levels [81].

Since, the bandgap in the semiconductors can be determined, his method is useful for nanoscience, where the size of particles tunes their optical properties. Additionally, the core/shell nanostructures can be studied, because the nanoparticles consisted the material only from core show different luminescence to compare with these having shell from different material surround [30]. Furthermore, the defects can be also detected by PL spectroscopy [82].

### 2.3.4 Thermodynamic characterization methods

The thermodynamic characterization methods base on changes in temperature, pressure, phase, or volume. As an example, the thermal gravimetric analysis (figure 4.12)

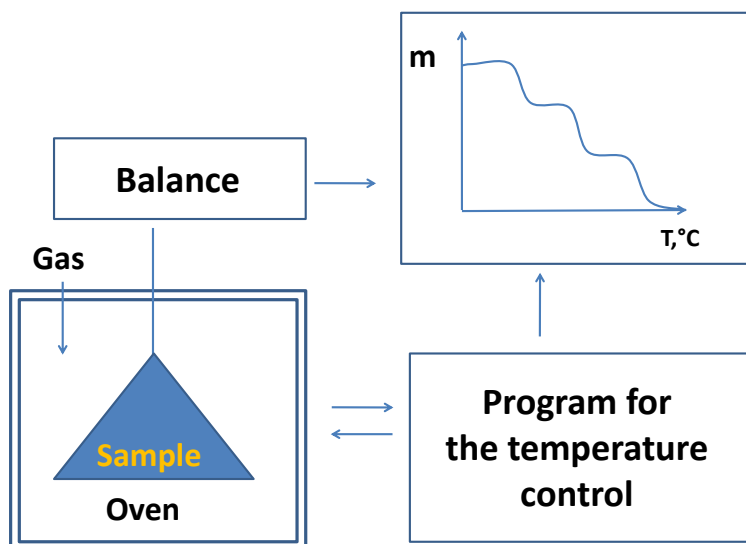


Figure 2.17: Thermal gravimetric analysis - Scheme of working principle.

## 2.3 Characterization methods

---

measures the mass loss of a sample as a function of temperature. The resulting data plot represents a percent weight loss versus temperature and reveals information on thermal stability or composition of material [77]. In the case of nanoparticles, this characterization method is used to gain information about the ligand coverage of the nanoparticles. Various organic molecules might be bound to the nanoparticle surface with different bonding strength. Thus, the mass loss is observed at different temperature, which can be associated with the kind of ligands.

## 2. THEORETICAL BACKGROUND

---



## Chapter 3

# Experimental part

Three synthesis techniques described already in the theoretical part were used in this thesis, in particular hot-injection and non-injection methods based on homogeneous NP nucleation as well as seed-mediated method with heterogeneous NP nucleation. The latter was used for hybrid nanoparticle preparation.

### 3.1 Synthesis of lead chalcogenide nanocrystals

The PbE NCs were synthesized on the basis of method previously reported for CdE NCs [46, 83]. A typical procedure of a PbSe synthesis uses two precursor solutions prepared separately: First, the Se precursor solution (1M) was obtained under nitrogen atmosphere in a standard glovebox: 0.4 ml of trioctylphosphine (TOP) and 0.4 mmol of Se powder were deposited in a separate flask and permanently stirred until selenium was completely dissolved. The preparation of a Pb precursor solution was carried out under inert conditions: 0.4 mmol of PbO and 0.6 mmol of oleic acid (OA) were mixed with 10 ml of octadecene (ODE) by permanent stirring and heating to 100°C under vacuum for 30 minutes until the precursors were completely dissolved. Further on, the system was connected to an argon flow and heated up to 300°C (figure 3.1).

After the first observation of a dark precipitate, a 1M (0.4 ml) TOPSe solution was rapidly injected into the reaction mixture under vigorous stirring. This corresponds to a molar ratio of Pb:Se of 1:1. The colour of the solution immediately turned to deep black. The reaction temperature was then reduced to 250°C for the growth of NCs. To

### 3. EXPERIMENTAL PART

---

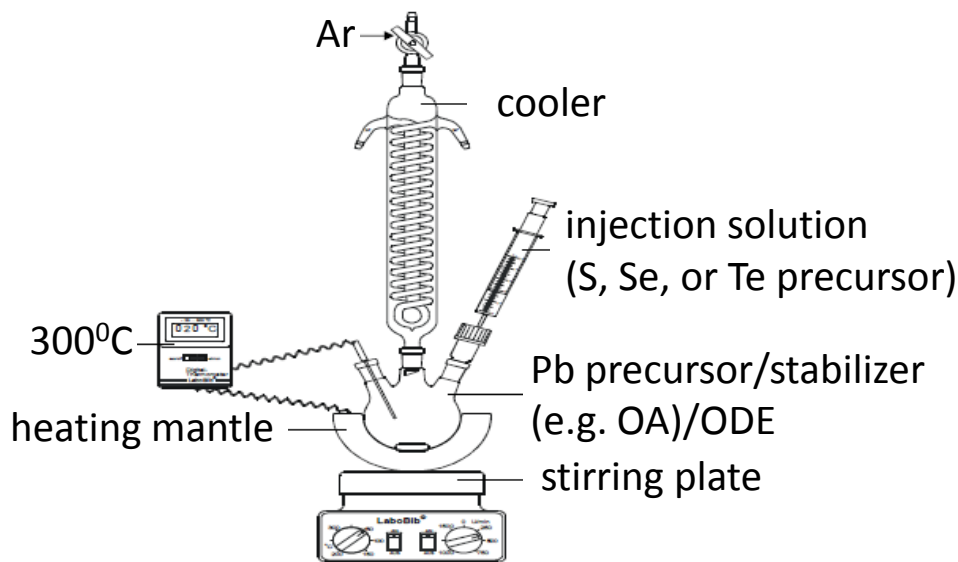


**Figure 3.1:** Scheme of the experimental set-up for colloidal nanoparticle preparation using a hot-injection method - Synthesis of lead chalcogenide nanocrystals.

stop the reaction, the heating mantle was then removed, and the reaction vessel rapidly cooled to room temperature.

For the sake of cleaning, the sample was centrifugated immediately, in order to separate the nanocrystal solution from the precipitate. Then the dark solution was mixed with a hexane / methanol blend, containing 3 ml of hexane and 7 ml of methanol, and then centrifugated again. The colored nanoparticle phase was separated and mixed with excess acetone to precipitate the nanocrystal products. The NCs were isolated through centrifugation. Afterwards, the precipitated NCs were dissolved in a small amount of hexane and precipitated again with excess acetone several times for further cleaning. The final product could be dissolved in the solvents such as toluene, chlorobenzene, or hexane.

In the syntheses of other lead chalcogenide NCs, the procedure is similar as described above. The differences consist in the use of other precursors and a variation of their molar ratios. We used lead acetate ( $\text{Pb}(\text{Ac})_2$ ) instead of  $\text{PbO}$ ; hexadecylamine (HDA)/OA mixture instead of OA; tellurium, selenium, or sulfur powder dissolved in TOP, tributylphosphine (TBP), or ODE instead of TOPSe. The solutions with ODE

## 3.2 Synthesis of indium oxide nanoparticles

were heated to dissolve the powder in the precursor preparation step.

### 3.1.1 Hexylamine treatment of original PbSe nanocrystals

PbSe NCs synthesized with an initial molar ratio of Pb/Se = 1:1 and TOPSe as a Se precursor were subjected to ligand exchange with hexylamine, using a procedure which is similar to the one reported previously [84]. A typical PbSe ligand exchange is performed by dissolving the washed NCs in excess hexylamine and sonicating them for 30 minutes. Then, the NCs were precipitated with excess ethanol and isolated by centrifugation. This procedure was done several times. The NCs were then redissolved in chlorobenzene.

## 3.2 Synthesis of indium oxide nanoparticles

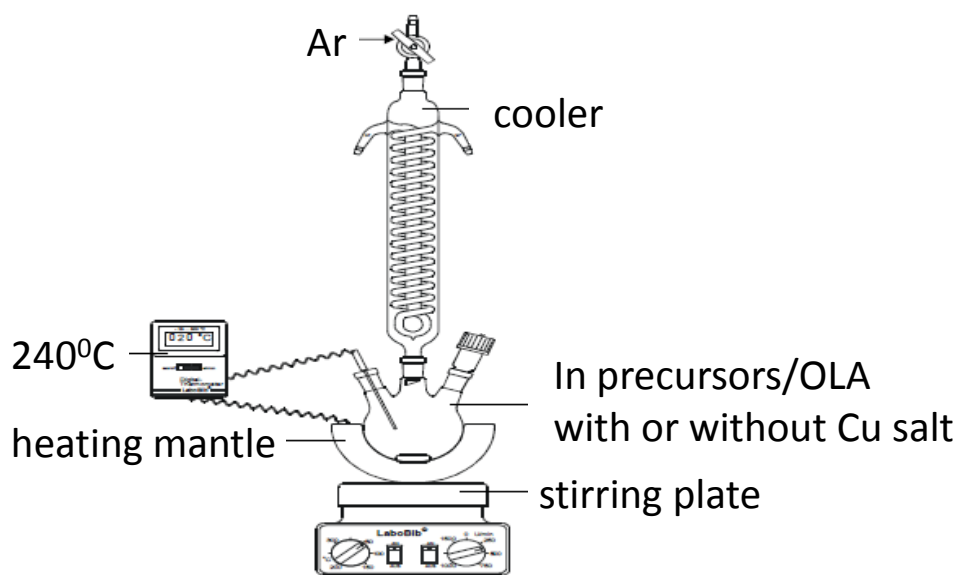


**Figure 3.2:** Scheme of the experimental set-up for colloidal nanoparticle preparation using a non-injection technique - Synthesis of indium oxide nanoparticles.

### 3. EXPERIMENTAL PART

---

#### 3.2.1 Synthesis of flower-shaped $\text{In}_2\text{O}_3$ nanocrystals

In a typical reaction 1.5 mmol (0.438g) of indium acetate ( $\text{Inac}_3$ ) was mixed with 15 mmol (5ml) of oleylamine (OLA) in a three-neck round-bottom flask, and the solution was evacuated at room temperature for 30 min (figure 3.2). Then the mixture was heated to 240°C under argon flow for 30 min. The  $\text{In}_2\text{O}_3$  nanoparticles were isolated by cooling the reaction mixture to room temperature and, subsequently, centrifuging at 5000 rpm for 5 min. The white-yellowish solid product was washed with ethanol and then dispersed in hexane.

#### 3.2.2 Synthesis of $\text{In}_2\text{O}_3$ nanocrystals employing organic ligand molecules

##### Oleic acid

0.1 mmol (0.0292g) of  $\text{Inac}_3$  was dissolved in a mixture contained 3 mmol (1ml) oleic acid (OA) and 7.6 mmol (2.5ml) OLA at room temperature and kept under vacuum for 30 min. Then the solution was heated to 240°C under argon atmosphere for 30min (figure 3.2).

##### Trioctylphosphine oxide

0.1 mmol (0.0292g) of  $\text{Inac}_3$  was dissolved in the mixture contained 10 mmol (4.2ml) of trioctylphosphine oxide (TOPO) and 7.6 mmol (2.5ml) OLA at room temperature under vacuum for 30 min. Then the solution was heated to 240°C under argon atmosphere for 30min (figure 3.2).

The cleaning procedure is similar to the one described above.

#### 3.2.3 Synthesis of quasi-spherical $\text{In}_2\text{O}_3$ nanocrystals

In a typical experimental procedure 0.1 mmol (0.0292g) of indium acetate ( $\text{Inac}_3$ ), 0.1 mmol of a copper salt (0.0128g of copper (I) acetate ( $\text{Cuac}$ ), 0.0182g of copper (II) acetate ( $\text{Cu}(\text{ac})_2$ ), 0.0262g of copper (II) acetylacetonate ( $\text{Cu}(\text{acac})_2$ ), or 0.01g of copper (I) chloride ( $\text{CuCl}$ ), and 7.6 mmol (2.5ml) of OLA were mixed in a three-neck flask, and the solution was evacuated at room temperature for 30 min. Then the mixture was heated to 240°C under argon flow for 30 min (figure 3.2). The  $\text{In}_2\text{O}_3$  nanoparticles were isolated by cooling the reaction mixture to room temperature and,

### 3.3 Synthesis of CIS and CIS/Au hybrid nanoparticles

subsequently, centrifugating at 5000 rpm for 5 min. The yellowish liquid product was centrifugated with ethanol, and the resulting solid product was dispersed in hexane.

#### 3.2.4 Synthesis of elongated $\text{In}_2\text{O}_3$ nanocrystals

Indium chloride ( $\text{InCl}_3$ ) (0.1mmol, 0.0221g) and Cuac (0.1mmol, 0.0123g) were mixed with 7.6 mmol (2.5ml) of OLA at room temperature under vacuum for 30 min and then heated to  $240^\circ\text{C}$  under argon flow for 30 min (figure 3.2). The  $\text{In}_2\text{O}_3$  nanoparticles were isolated by cooling the reaction mixture to room temperature and, subsequently, centrifugating at 5000 rpm for 5 min. The yellowish liquid product was centrifugated with ethanol, and the resulting solid product was dispersed in hexane.

### 3.3 Synthesis of CIS and CIS/Au hybrid nanoparticles

#### 3.3.1 Synthesis of CIS nanoparticles

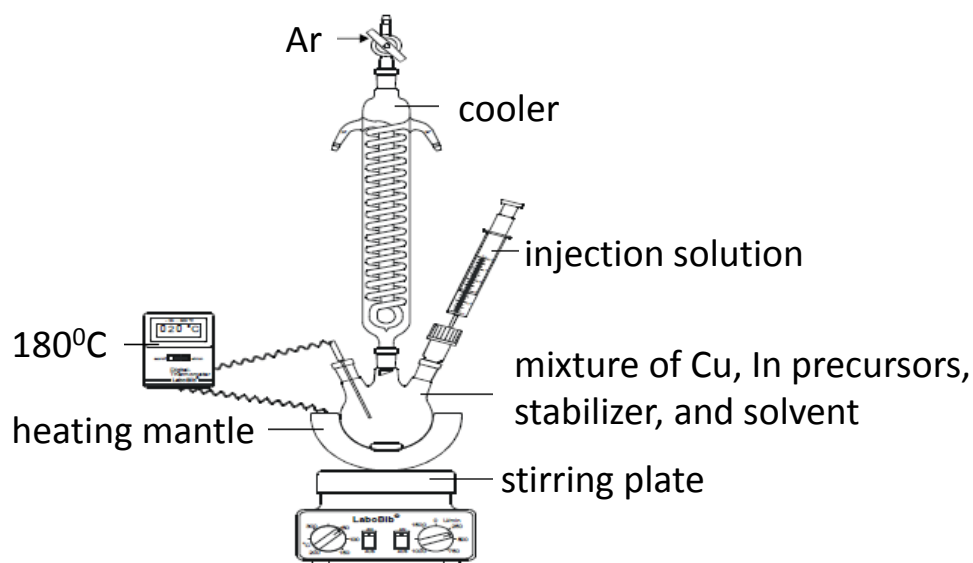


**Figure 3.3:** Scheme of the experimental set-up for colloidal seed preparation using a hot-injection technique - Synthesis of CIS nanoparticles.

The  $\text{CuInSSe}$  nanoparticles were synthesized using a modification of a previously reported method [85]. In brief,  $\text{CuCl}$  (0.1 mmol) and  $\text{InCl}_3$  (0.1 mmol) were mixed with dodecanethiol (DDT) (1 ml) and ODE (2ml) at room temperature. Afterwards, the

### 3. EXPERIMENTAL PART

---

solution was heated to 180°C, a Se solution in TOP (0.2 mmol Se dissolved in 0.2 ml TOP) was injected into the reaction mixture, and then the reaction temperature was kept at 180°C for an hour (figure 3.3. After the reaction mixture was cooled to room temperature, 10 ml acetone was added to precipitate the nanocrystalline product. The precipitated nanocrystals were washed with  $\text{CHCl}_3/\text{CH}_3\text{OH}$  (1:3, v/v) three times and then dissolved in toluene to get the nanocrystal solution.

The  $\text{CuInS}_2$  nanoparticles were prepared by Marta Kruszynska using the method published recently [80].

#### 3.3.2 Synthesis of CIS/Au hybrid nanoparticles

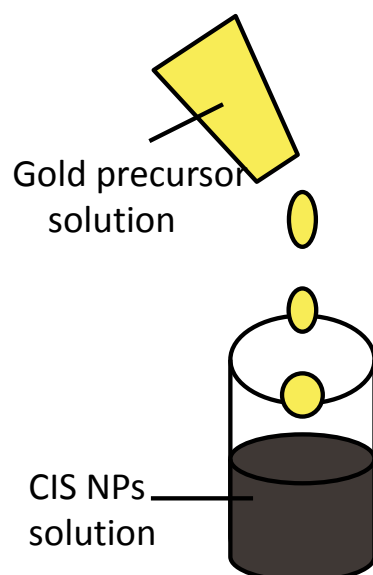


**Figure 3.4:** Scheme of the experimental set-up for colloidal preparation of hybrid nanostructures using a seed-mediated method - Synthesis of CIS/Au nanostructures.

The procedure of growth of Au NCs is similar to a previously reported procedure for CdSe NCs [44]. Briefly, a gold precursor solution was prepared by dissolving  $\text{AuCl}_3$  (12.5 mg), dodecylamine (DDA) (73 mg) and didodecyldimethylammonium bromide (DDAB) (41.7 mg) in toluene (3.125 ml) by sonication. This gold growth solution was added dropwise to a solution of  $\text{CuInS}_2$  NPs in toluene at room temperature while vigorously stirring (figure 3.4). The reaction was stopped by precipitating the

hybrid nanocrystals with methanol. The nanocrystals were redissolved in toluene for characterization.

The synthesis of CuInS<sub>2</sub>-based nanostructures was conducted in the same way.

## 3.4 Materials

Lead (II) oxide yellow (PbO, puriss. p.a.,  $\geq 99,0\%$  kT), tellurium powder (Te, purum p.a.), hexylamine (purum,  $\geq 98\%$  (GC)), octylamine (purum,  $\geq 98\%$  (GC)), tridodecylamine (techn,  $\sim 85\%$  (GC)) were purchased from Fluka; oleic acid (OA, tech., 90%), tri-n-octylphosphine (TOP, 90%), tributylphosphine (TBP), chloroform-d (CDCl<sub>3</sub>, 99.8 atom % D (containing 0.1% (v/v) tetramethylsilane (TMS))), sulphur (S, puriss.), copper (I) acetate (Cuac, 97%), copper (II) acetate (Cu(ac)<sub>2</sub>, 98% trace metals basis), copper (II) acetylacetonate (Cu(acac)<sub>2</sub>, 97%), copper (I) chloride (CuCl), indium (III) chloride (InCl<sub>3</sub>, 98%), 1-dodecanethiol (DDT, 98%), gold (III) chloride (AuCl<sub>3</sub>, 99%), didodecyldimethylammonium bromide (DDAB, 90%) were delivered from Aldrich; selenium powder (Se, 99.99%) was purchased from ChemPur; 1-octadecene (ODE) was ordered from Merck; oleylamine (OLA,  $\sim$  C18-content 80-90%), and dodecylamine (DDA, 98%) were purchased from Acros Organics; indium (III) acetate (Inac<sub>3</sub>, 99.99%, metal basis), and trioctylphosphine oxide (TOPO, 98%) were delivered from Alfa Aesar. All chemicals were used without further purification.

## 3.5 Characterization

### Transmission electron microscopy (TEM)

The TEM images were taken on a Zeiss EM 902A transmission electron microscope with an acceleration voltage of 80 kV. High resolution transmission electron microscopy (HRTEM) measurements were performed on a FEI Tecnai F20 S-TWIN microscope with an acceleration voltage of 200 kV. The specimens were prepared by deposition a drop of a solution of NCs on a carbon-coated copper or nickel grid and drying at room temperature.

### 3. EXPERIMENTAL PART

---

#### **Energy dispersive X-ray analysis (EDX)**

The integral stoichiometry of PbSe, CuInSSe, and CuInSSe/Au NPs was obtained by the EDAX detector integrated into a FEI Quanta 200 3D scanning electron microscope. The samples were prepared by putting a solution of the NCs onto an Al plate.

The EDX analysis of In<sub>2</sub>O<sub>3</sub> NPs was carried out by the EDAX r-TEM EDX-Detektor mit S-UTW Fenster integrated into FEI Tecnai F20 S-TWIN high-resolution transmission electron microscope. The sample were prepared by deposition a drop of a solution of NCs on a carbon-coated nickel grid.

#### **Powder X-ray diffraction (XRD)**

Powder X-ray diffraction (XRD) was measured with a PANalytical X'Pert PRO MPD diffractometer operating with Cu K $\alpha$  radiation, Bragg-Brentano  $\Theta$ - $2\Theta$  geometry, a goniometer radius of 240 mm, and variable slits. The samples were prepared by dropping colloidal solution on low-background silicon substrates. The XRD data was analyzed using the X'Pert HighScore Plus software in conjunction with the ICDD database, version 2.0902. Rietveld refinement of the diffraction patterns was conducted using the program MAUD [86]. The patterns were fitted using a polynomial background and default instrument line broadening from the MAUD software. The anisotropic size-strain model developed by Popa [87] was used to account for anisotropic crystallite shapes, while texture effects were included by the harmonic texture model [88].

#### **UV-Vis absorption spectroscopy**

Absorption spectra were recorded on a Carry 5000 for In<sub>2</sub>O<sub>3</sub> NPs and Carry 100 for CuInSSe and CuInSSe/Au NPs absorption spectrophotometer (Varian), using 1 cm path length quartz cells.

#### **Photoluminescence spectroscopy**

Photoluminescence spectra were measured at room temperature on Fluorolog3 FL322 fluorescence spectrophotometer. The nanoparticles were dissolved in hexane.



#### **Nuclear magnetic resonance (NMR)**

The NMR spectra were recorded on a Bruker DRX 500 NMR spectrometer operating at 500 MHz. The  $^1\text{H}$  and  $^{13}\text{C}$  NMR analyses for synthesis study of PbSe NCs were carried out by dissolving the NCs (or samples taken from reaction solution) in  $\text{CDCl}_3$ . In the case of synthesis study of  $\text{In}_2\text{O}_3$  NPs the NMR analysis was carried out by dissolving in  $\text{CDCl}_3$  the liquid part of sample taken from the reaction which was separated from  $\text{In}_2\text{O}_3$  NPs by centrifugation.

The  $^{13}\text{C}$  NMR spectra were referenced to an internal  $\text{CDCl}_3$  reference at  $\delta$  77.0. The  $^1\text{H}$  NMR spectra were referenced to tetramethylsilane (TMS) at  $\delta_H$  0.0.

#### **Thermogravimetric analysis (TGA)**

The measurement was performed under Ar atmosphere on a Simultane TG-DTA/DSC Apparatur (STA 449 F3 Jupiter) from NETZSCH, using a heating rate of  $2.5^\circ\text{C}/\text{min}$  up to a temperature of  $600^\circ\text{C}$ .

### 3. EXPERIMENTAL PART

---

## Chapter 4

# Hot-injection synthesis of lead chalcogenide nanocrystals: Influence of synthesis mechanism on the nanocrystal surface properties

### 4.1 Motivation

Colloidal semiconductor nanocrystals, such as lead sulfide (PbS), lead selenide (PbSe) and lead telluride (PbTe), are of high interest because of their unique size-dependent properties, what offers a wide range of applications in low cost photodetectors [89, 90], photovoltaics [23, 26, 28], optical modulators [91], and optical sources [89]. Due to the quantum size effect, the synthetic control of shape and size by variation of reaction conditions enables controlled tuning of their optical properties [23].

Due to the large Bohr radius of lead chalcogenides (PbE, E = S, Se, Te) [92], the band gap energy and, therefore, also the size-dependent absorption and photoluminescence can be tuned over a wide range covering the near-infrared spectral region [28]. The large dielectric constant [26, 93], efficient multiple exciton generation [23, 28], and high carrier mobility [91] make the Pb compounds attractive for use as photoactive material in solar cells.

#### 4. HOT-INJECTION SYNTHESIS OF LEAD CHALCOGENIDE NANOCRYSTALS: INFLUENCE OF SYNTHESIS MECHANISM ON THE NANOCRYSTAL SURFACE PROPERTIES

---

In so-called hybrid solar cells, inorganic semiconducting nanocrystals (NCs) which serve as electron acceptors are blended with an organic semiconductor, normally a conjugated polymer like regio-regular poly(3-hexylthiophene) (P3HT), which acts as an electron donor [94]. The charge separation between donor and acceptor can be studied by electron spin resonance (ESR) spectroscopy [46, 95, 96], which detects the unpaired spin of polarons, and by photoinduced absorption (PIA) spectroscopy [84], which monitors the change in the transmission of an NC/polymer blend due to optical transitions involving polaronic states. Reports on the absolute energetic position of the energy levels of PbSe nanocrystals suggest a possible charge separation between P3HT and sufficiently small PbSe NCs in hybrid films [23]. However, a recent PIA study of blends of small PbSe NCs and P3HT did not show a sign for successful charge separation at the donor/acceptor interface [84]. Thus, there is still a controversial discussion, and it remains unclear, why PbSe/polymer bulk heterojunction solar cells have achieved a power conversion efficiency of only 0.1%, so far [23, 84].

The lack in the understanding of the principle problems of these solar cells pushes forward fields of nanochemistry, such as the development of new synthetic routes and the modification of the nanoparticle surface. Improved knowledge on synthesis methods, their mechanisms as well as post-synthetic cleaning and surface-modification procedures might be the key to more efficient devices. The high-temperature solution phase synthesis appears to be the most suitable method to synthesize nearly monodisperse PbE NCs [97, 98, 99, 100], but the existence of a ligand shell surrounding NCs is often a major hindrance for their further application [46]. Thus, ligand exchange is used to improve the surface properties of the NCs, but the organic ligands are often strongly bound to the surface. Consequently, the procedure of the surface modification can be more complicated as it may appear. For example, in the case of CdSe, it was recently shown that common stabilizers such as oleic acid cannot be completely removed when applying a ligand exchange with pyridine [46] or alkylamines [96]. In the case of lead chalcogenide nanocrystals, there are just a few reports on ligand exchange procedures [101, 102].

In this chapter, an alternative hot-injection synthetic route is presented, providing high-quality PbE NCs with narrow size distribution and different shapes, which includes the occurrence of *in situ* formed Pb<sup>0</sup> particles. The size and shape control by systematic variation of the materials employed (precursors and stabilizers) and their

## 4.2 Size and shape control of lead chalcogenide nanoparticles

concentrations is demonstrated. Oleic acid was used as a stabilizer in the synthesis, but in view of application of PbSe NCs in solar cells, a ligand exchange procedure with hexylamine was also developed and investigated with nuclear magnetic resonance (NMR) and thermogravimetric analysis (TGA). Finally, results from ESR and PIA measurements on blends of PbSe NCs in a P3HT matrix are shown, in order to bring more light into the controversial discussion on charge separation in the material system considered.

### 4.2 Size and shape control of lead chalcogenide nanoparticles

Reactions with systematic variations of parameters have been investigated, in order to study the impact on the resulting NCs and to optimize the synthesis conditions. Different types of Pb and E (S, Se, Te) precursors, as well as stabilizers, and their dif-

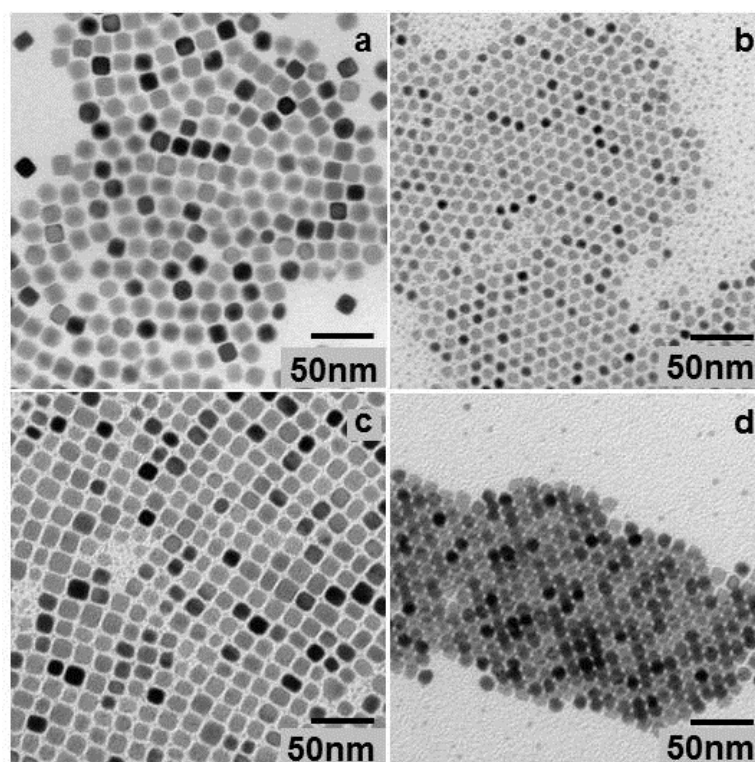


**Figure 4.1:** TEM images of lead chalcogenide nanocrystals - a) PbS NCs, b) PbSe NCs, c) PbTe NCs , d) a PbSe super-crystal.

#### 4. HOT-INJECTION SYNTHESIS OF LEAD CHALCOGENIDE NANOCRYSTALS: INFLUENCE OF SYNTHESIS MECHANISM ON THE NANOCRYSTAL SURFACE PROPERTIES

---

ferent concentrations have been used to study their influence. The size and morphology of as-synthesized nanomaterials were characterized by TEM. Figures 4.1-4.5 present a selection of TEM images of nanoparticle samples produced under different conditions. Additional results are summarized in Table 4.1. Figure 4.1a-c shows the TEM images

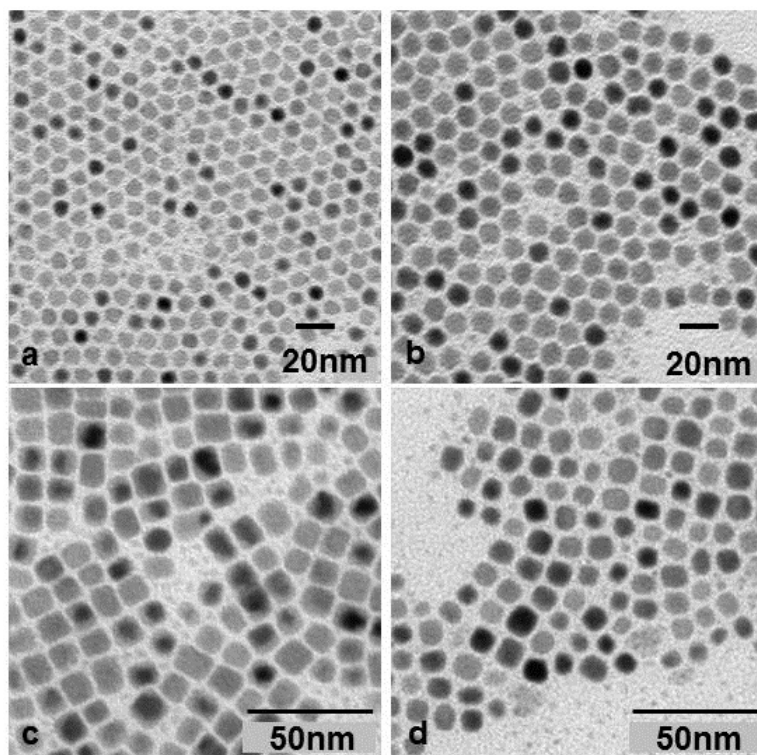


**Figure 4.2:** TEM images of spherical PbSe and cubic PbTe NCs illustrating the size control - a) and b) PbSe NC size depends on using of different Se precursors: TBPSe (a) and TOPSe (b); c) and d) PbTe NC size depends on using of different Pb:Te ratio: (c) 4:1 and (d) 1:1.

of as-synthesized PbS, PbSe, and PbTe NCs. The NCs are uniform both in shape and size. Different materials, such as PbS, PbSe, and PbTe NCs, can be obtained by the above synthesis route, and it is possible to employ various E precursors like E/ODE, TBPE, and TOPE. In figure 4.1a, S/ODE was used for PbS NCs, in figure 4.1b, TBPSe for PbSe, and in figure 4.1c, TOPTe for PbTe. Additionally, we observed that the NCs dried on a TEM grid do not only form well-ordered two-dimensional superlattices, but even small faceted colloidal 3D-supercrystals, what indicates a relatively narrow size distribution of the NCs. Figure 4.1d shows an example for a three-dimensional

## 4.2 Size and shape control of lead chalcogenide nanoparticles

superlattice of PbSe NCs.

The size control achieved for PbSe NCs is illustrated in figure 4.2a,b. These NCs were prepared under the same conditions, except for the Se precursor. The NCs

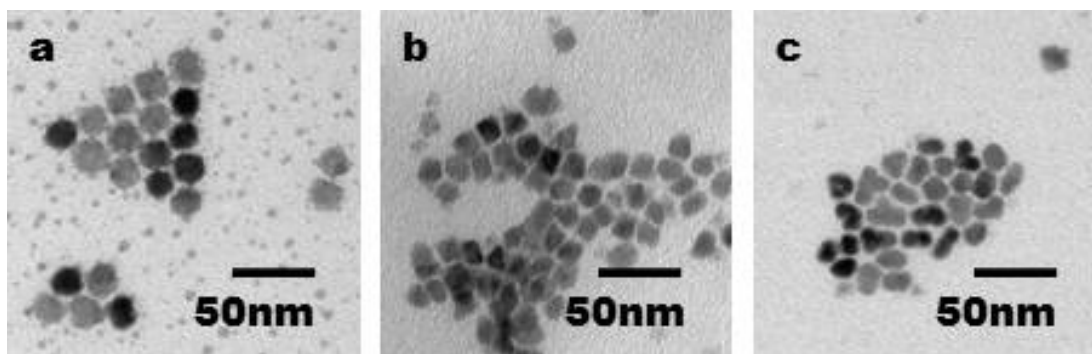


**Figure 4.3:** TEM images of PbSe NCs demonstrating the shape control - a)  $\text{Pb}(\text{ac})_2$  was used as Pb precursor, b) octylamine was used as stabilizer, and c) tridodecylamine was used as stabilizer.

synthesized with TBPSe are smaller ( $8.9 \pm 0.3 \text{ nm}$ ) than NCs synthesized with TOPSe ( $12.8 \pm 0.4 \text{ nm}$ ), although the growth time was the same. The TBPSe is known as more

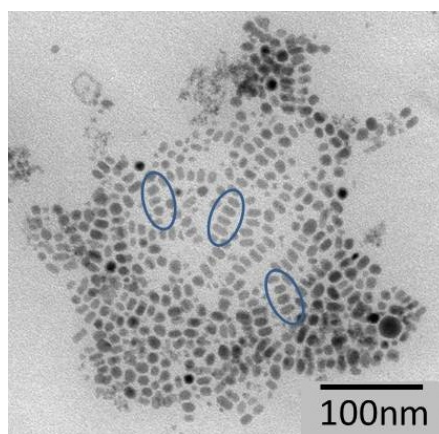


**Figure 4.4:** TEM images of PbS nanorods - Hexadecylamine was used for stabilization.

reactive compound compared to TOPSe. After addition of Se, the nucleation occurs much faster in the presence of TBP, consequently, more nuclei appear which consume the Pb and Se monomers. In the case of TOP, the number of nuclei is lower, thus, they can have more material available to grow.

#### 4. HOT-INJECTION SYNTHESIS OF LEAD CHALCOGENIDE NANOCRYSTALS: INFLUENCE OF SYNTHESIS MECHANISM ON THE NANOCRYSTAL SURFACE PROPERTIES

---

Similar result have been achieved for PbTe NCs shown in figure 4.2c,d. The ratio Pb precursor (PbO) to Te precursor (TOPTe) decreases, so the size of nanoparticles become smaller (from  $8.6\pm 0.6$  nm to  $6.6\pm 0.5$  nm). The amounts of PbO and OA (stabilizer) are the same, but the amount of TOPTe solution is different. The monomer activity is suppressed, when the concentration of TOPTe is lower, that causes the smaller size of nanoparticles (figure 4.2d).

In figure 4.3, the shape control based on PbSe NCs is shown. The star-shaped PbSe NCs were synthesized using  $\text{PbAc}_2$  as a Pb precursor (figure 4.3a), that is in good agreement with Houtepen's experiments [103]. The latter showed that the presence of acetate in the reaction leads to starlike NPs formed by oriented attachment. The quasi cubic PbSe NCs (figure 4.3b) appear due to the presence of octylamine. The elongated NCs were synthesized using tridodecylamine as a stabilizer. For the preparation of spherical PbSe NCs, using OA and PbO is necessary (figure 4.1b and figure 4.1d). The

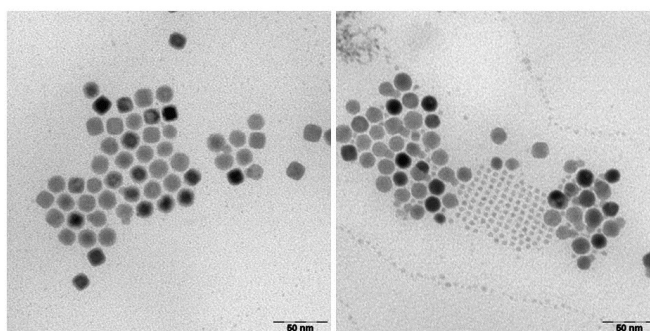


**Figure 4.5: TEM images of PbS NCs demonstrating the shape control - a) Cubic PbS NCs, b) spherical PbS NCs.**

PbS nanorods are synthesized using hexadecylamine for stabilisation (figure 4.4). The tendency to self-organization can be observed. Additionally, the changing of the PbS NC shape from cubic to spherical could be observed during the reaction (figure 4.5). The cubic particles become smaller and disappear while the spherical particles become slightly bigger.

To summarize, the changes of different parameters of this synthesis enable the control over size and shape of as synthesized PbE NCs.



## 4.2 Size and shape control of lead chalcogenide nanoparticles

**Table 4.1:** Synthesis and product parameters of lead chalcogenide nanoparticles

Material	Size,nm	Shape	Precursors	Pb:Se	Stabilizer	Growth time
PbS (fig.4.1a, 4.5a)	14.5±0.6	cubic	PbO+S/ODE	4:1	OA	10min
PbS (fig.4.5b)	15.6±0.7	spherical	PbO+S/ODE	4:1	OA	20min
PbS (fig.4.4)	14.2(±2.4) ×6.9(±1.9)	nanorods	PbAc <sub>2</sub> +S/ODE	4:1	OA/HDA	3min
PbSe	8.4±0.5	spherical	PbO+Se/ODE	2:1	OA	10min
PbSe (fig.4.1b,4.2a)	8.9±0.3	spherical	PbO+TBPSe	4:1	OA	2min
PbSe(SL)	6.4±0.3	spherical	PbO+TBPSe	2:1	OA	2min
PbSe	6.8±0.3	spherical	PbO+TBPSe	1:1	OA	2min
PbSe(SL) (fig.4.1d,4.2b)	12.8±0.4	spherical	PbO+TOPSe	4:1	OA	2min
PbSe(SL)	10.7±0.3	spherical	PbO+TOPSe	2:1	OA	2min
PbSe	14.4±0.4	spherical	PbO+TOPSe	1:1	OA	2min
PbSe(SL)	8.8±0.4	spherical	PbO+TOPSe	1:2	OA	30min
PbSe (fig.4.3b)	10.8±1.0	cubic	PbO+TOPSe	4:1	Octyl-amine	10min
PbSe	11.8±2.6	cubic	PbO+TOPSe	4:1	DDA	5min
PbSe (fig.4.3c)	14.2(±2.7) ×8.7(±0.9)	elongated	PbO+TOPSe	4:1	tridodecyl-amine	5min
PbSe	13.4±1.4	stars	PbO+TOPSe	4:1	HDA	5min
PbSe	8.3±0.4	spherical	PbO+TOPSe	4:1	OA:HDA= 1:1	3min
PbSe (fig.4.3a)	17.6±1.5	stars	PbAc <sub>2</sub> +TOPSe	4:1	OA:HDA= 1:1	3min
PbTe (fig. 4.2c)	8.6±0.6	cubic	PbO+TOPTe	4:1	OA	2min
PbTe (fig.4.1c)	11.9±1.0	cubic	PbO+TOPTe	2:1	OA	2min
PbTe	12.6±0.9	cubic	PbO+TOPTe	2:1	OA	20min
PbTe (fig. 4.2d)	6.6±0.5	cubic	PbO+TOPTe	1:1	OA	2min

## 4. HOT-INJECTION SYNTHESIS OF LEAD CHALCOGENIDE NANOCRYSTALS: INFLUENCE OF SYNTHESIS MECHANISM ON THE NANOCRYSTAL SURFACE PROPERTIES

---

### 4.3 Reaction mechanism and product characterisation

For the synthesis of PbE NCs, the Pb precursor was produced by heating the mixture of Pb precursor, stabilizer, and ODE under inert conditions until 300°C. Using PbO and OA, the solution becomes transparent indicating formation of lead oleate and then slightly dark. To investigate the dark precipitate, an XRD analysis has been carried out.

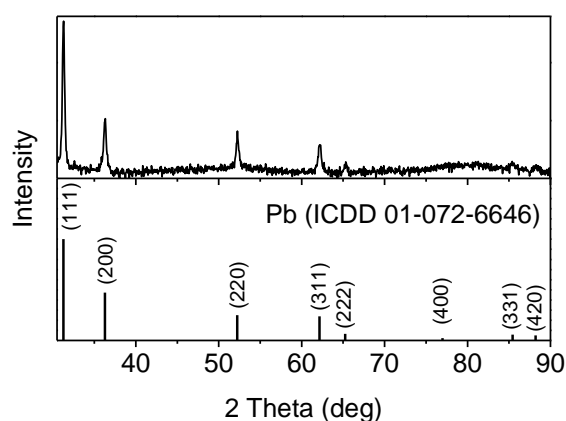


**Figure 4.6: XRD measurement of the Pb<sup>0</sup> precipitate** - The vertical lines below indicate the corresponding reference patterns from the ICDD database for comparison.

Figure 4.6 shows the XRD pattern obtained, which reveals the existence of crystalline Pb<sup>0</sup> nanoparticles. They form without addition of any reducing agent, most likely due to a disproportionation reaction of Pb<sup>2+</sup> ions (figure 4.7). Pb<sup>0</sup> particles might regulate the monomer supply for the growth of the PbE NCs and, therefore, influence the reaction kinetics, as it was proposed for CdTe NCs [83]. Taking into account that

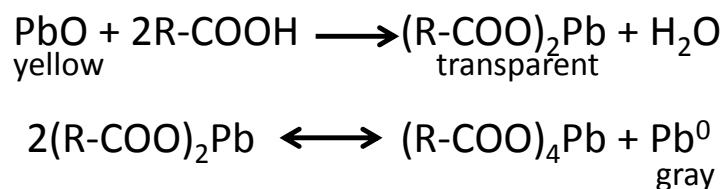


**Figure 4.7: Scheme of Pb precursor formation** - Disproportionation reaction of Pb<sup>2+</sup> ions.

### 4.3 Reaction mechanism and product characterisation

the  $\text{PbAc}_4$  belongs to hard oxidation agents [104, 105, 106, 107, 108, 109] e.g. for alcohols, and acids as well as for double bond, we assume that  $\text{Pb}(\text{OA})_4$  is likely to react with the oleic acid on the double bond and functional group as the oxidation agent. Since the OA could not be observed on the NP surface (details are discussed below), we suggest that the OA transforms into other organic compounds which can stabilize the NCs. This suggestion was proved by  $^{13}\text{C}$  NMR and  $^1\text{H}$  NMR study. The measurements of the reaction solution, taken after  $\text{PbO}$  and OA were mixed and heated until  $300^\circ\text{C}$ , are shown in figure 4.8 together with the spectra of nanocrystals and pure OA for comparison. The latter spectra were taken from Spectral Database for Organic Compounds SDBS. Every carbon atom for the  $^{13}\text{C}$  NMR measurement as

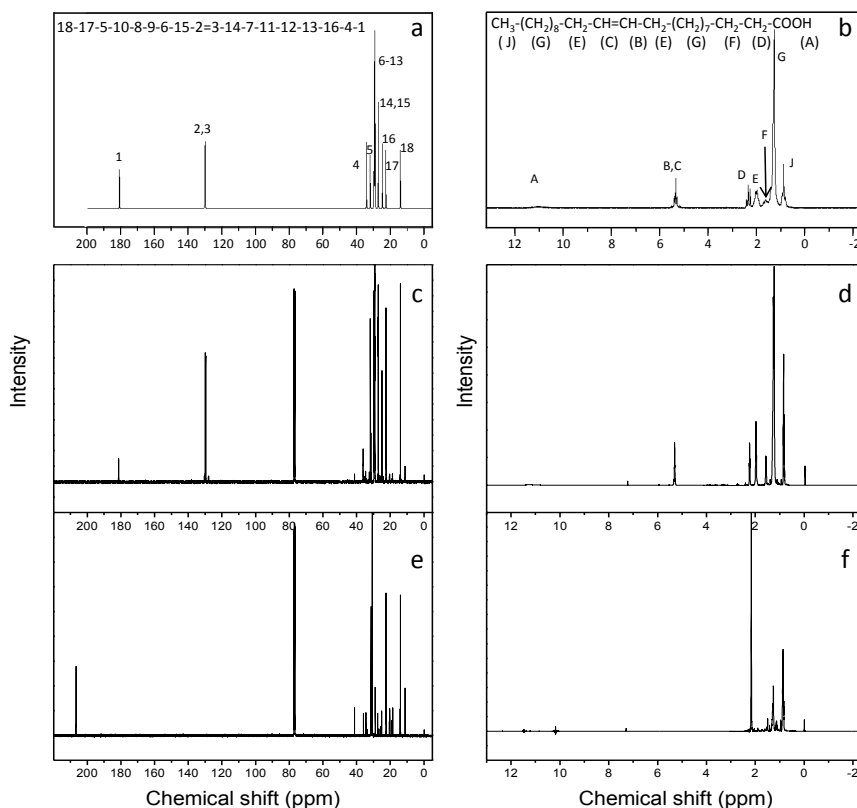


**Figure 4.8:** NMR measurements clarified reaction mechanism - a) and b) the  $^{13}\text{C}$  NMR (15.09 MHz) and  $^1\text{H}$  NMR (90 MHz) spectra taken from the SDBS, c) and d) the  $^{13}\text{C}$  NMR and  $^1\text{H}$  NMR spectra of the  $\text{PbO}$  mixed with OA at  $300^\circ\text{C}$ , e) and f) the  $^{13}\text{C}$  NMR and  $^1\text{H}$  NMR spectra of the  $\text{PbSe}$  NCs, respectively.

well as hydrogen atoms for  $^1\text{H}$  NMR are signed as numbers (e.g. "1" for  $-\text{COOH}$ , or

#### 4. HOT-INJECTION SYNTHESIS OF LEAD CHALCOGENIDE NANOCRYSTALS: INFLUENCE OF SYNTHESIS MECHANISM ON THE NANOCRYSTAL SURFACE PROPERTIES

---

2 and 3 for  $\text{-C=C-}$  (figure 4.8a)) or letters (e.g. "A" for  $\text{-COOH}$  (figure 4.8b)). It is clear to see, that the double bond and functional group are detectable in the mixture of PbO and AO at high temperature (figure 4.8c,d), but not on the nanoparticle surface (figure 4.8e,f). The strong peaks at 210 ppm and 30 ppm (figure 4.8e) as well as at 2.17 ppm (figure nmr1f) can be assumed as impurities after cleaning with acetone.

After the first observation of a dark precipitate, the solution with E precursor was injected. The color of the reaction mixture becomes deep dark immediately, indicating the formation of PbE nanocrystals.

To achieve a better understanding of the whole system, the PbSe NCs synthesized as described in the experimental section (Chapter 3) have been investigated. As-produced PbSe NCs were analyzed after removal of the  $\text{Pb}^0$  particles from the solution. A

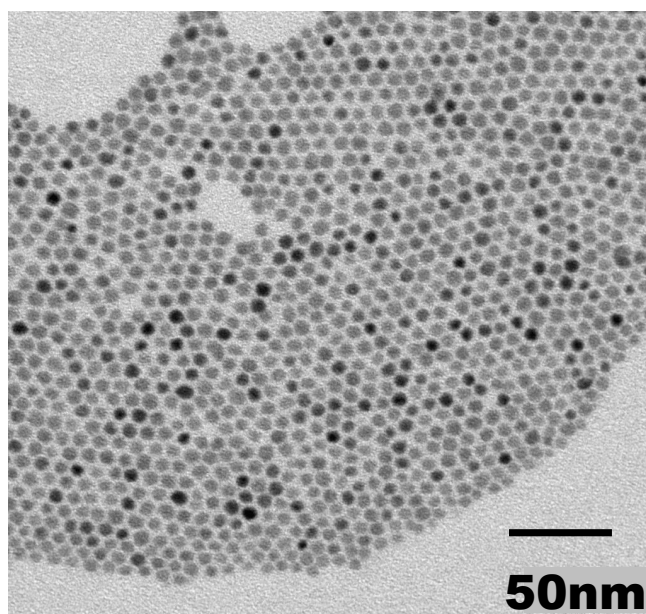


**Figure 4.9:** TEM image of as-synthesized PbSe NCs - The PbSe NCs are spherical shaped.

TEM image of PbSe NCs with  $6\pm 0.4$  nm diameter is given in figure 4.9, revealing the formation of spherically shaped NCs with a narrow size distribution. Figure 4.10 shows the corresponding XRD pattern, confirming the successful formation of PbSe. The reflections are broadened, indicating a nanocrystalline material. The mean diameter of the NCs calculated from the width of the XRD reflections by means of the Scherrer

### 4.3 Reaction mechanism and product characterisation

equation with  $K=1$  is 6.1 nm. The elemental composition was determined by EDX

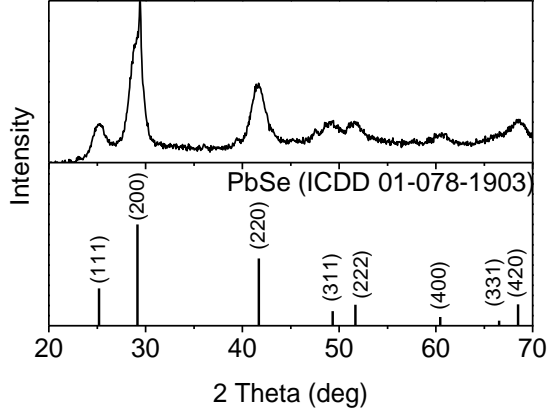


**Figure 4.10: XRD measurement of the PbSe NCs** - The vertical lines below indicate the corresponding reference patterns from the ICDD database for comparison.

measurements (figure 4.11). The ratio of Pb to Se is 1.5:1, although the particles were prepared with an initial Pb/Se molar ratio of 1:1. We estimated the fraction of surface Pb and Se atoms by calculating the overall number of surface atoms from the size of the nanoparticles and the lattice parameters of PbSe. From the literature [110] the number of Pb surface atoms ( $S_{surf}$ ) can be calculated:

$$S_{surf} = \frac{(4/3\pi r^3 - 4/3\pi(r-d)^3)N}{V}, \quad (4.1)$$

where  $r$  is the radius of the PbSe nanoparticle,  $d$  is the Pb-Se bond length ( $d = 0.4$  nm),  $N$  is the number of PbSe units per unit cell ( $N = 4$ ), and  $V$  is the volume of a PbSe unit cell (with radius of 0.61 nm). To calculate the whole number of Pb units (on the surface and in the core) equation (4.1) must be modified [46]:

$$S_{surf+core} = \frac{(4/3\pi r^3)N}{V}. \quad (4.2)$$

The number of Pb units in the core is given by

$$S_{core} = S_{surf+core} - S_{surf} \quad (4.3)$$

Then, taking into account the results of the EDX measurements and assuming a stoichiometric nanocrystal core surrounded by a non-stoichiometric outer layer, the fraction

#### 4. HOT-INJECTION SYNTHESIS OF LEAD CHALCOGENIDE NANOCRYSTALS: INFLUENCE OF SYNTHESIS MECHANISM ON THE NANOCRYSTAL SURFACE PROPERTIES

---

of surface Pb and Se atoms was calculated as following:

$$N_{Se} = \frac{2S_{surf+core}}{1 + 1.5}, \quad (4.4)$$

where  $N_{Se}$  is number of all Se atoms, and the magnitude 1.5 is the EDX result for this PbSe NCs. Respectively, the number of all Pb atoms is given by

$$N_{Pb} = 2S_{surf+core} - N_{Se}. \quad (4.5)$$

The number of Se or Pb atoms placed on the surface is expressed as follows:

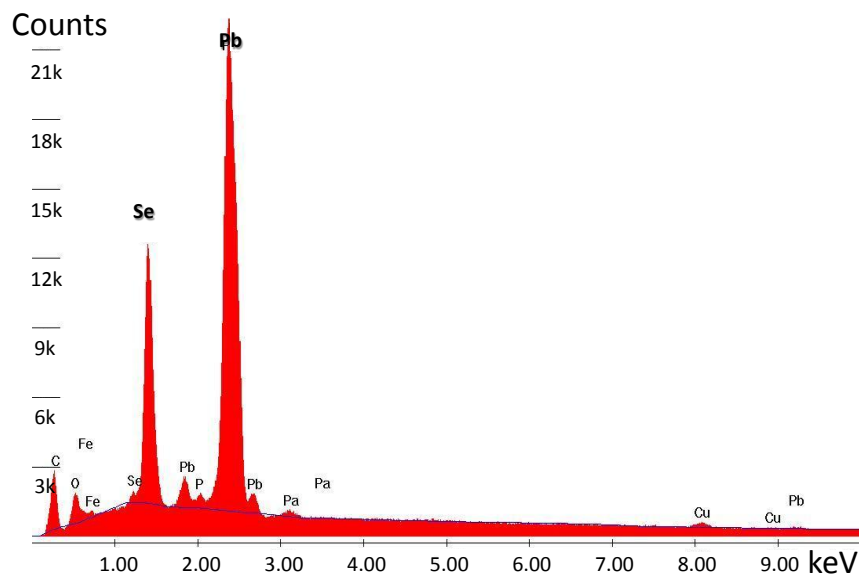


**Figure 4.11: EDX measurement of the PbSe NCs - The ratio of Pb to Se is 1.5:1.**

$$N_{Se}^{surf} = N_{Se} - S_{core}, \quad (4.6)$$

$$N_{Pb}^{surf} = N_{Pb} - S_{core}, \quad (4.7)$$

Finally, the percentage of Pb and Se surface atoms can be calculated:

$$X(\%)_{Se}^{surf} = \frac{N_{Se}^{surf}}{N_{Se}^{surf} + N_{Pb}^{surf}} 100\% \quad (4.8)$$

$$X(\%)_{Pb}^{surf} = 100\% - X(\%)_{Se}^{surf} \quad (4.9)$$

Our results ( $\sim 80\%$  Pb and  $\sim 20\%$  Se surface atoms) are consistent with experiments on PbSe by Moreels et al. [111], who supposed a stoichiometric PbSe core and a Pb-terminated surface shell.

## 4.4 Surface investigation

To investigate the surface of the PbSe NCs, the NMR measurement was carried out. As it was already mentioned, the spectra (figure 4.8e,f) did not show a sign for the presence of OA on the PbSe surface. In  $^1\text{H}$ -NMR spectrum there is no sign at 5.5 ppm for a double bound, neither at 2.3 ppm for  $\text{CH}_2\text{-COOH}$  or at 2.0 ppm for  $\text{CH}_2\text{-C=C}$ . In  $^{13}\text{C}$ -NMR spectrum the signs for a double bound (130ppm) and for  $\text{CH}_2\text{-COOH}$  (180ppm) are not found. Nevertheless the NCs are stable in colloidal solution. In figure 4.9 the TEM image of these NCs do not show any agglomeration. So, the absence of oleic acid on the nanoparticle surface is caused by the mechanism of the reaction (figure 4.7): The  $\text{Pb}(\text{OA})_4$  reacts with the oleic acid on the double bound and functional group. Under this reaction conditions, the OA transforms into other organic compounds which can stabilize the NCs.

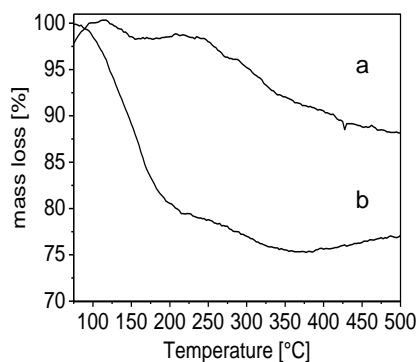


**Figure 4.12: Thermogravimetric analysis of original and hexylamine-treated PbSe NCs** - a) TGA data obtained for original PbSe NCs (slight increase in TGA curve in the beginning due to thermal inhomogenities in oven) and b) hexylamine-treated PbSe NCs [112].

Thermal gravimetric analysis (TGA) of the corresponding sample confirms that there is an organic shell of probably strongly binding ligands left, because there is a weight loss starting at  $\sim 250^\circ\text{C}$  and extending to rather high temperatures near  $500^\circ\text{C}$

#### 4. HOT-INJECTION SYNTHESIS OF LEAD CHALCOGENIDE NANOCRYSTALS: INFLUENCE OF SYNTHESIS MECHANISM ON THE NANOCRYSTAL SURFACE PROPERTIES

---

(figure 4.12a). The study shows that it is not always sufficient to assume that the ligands used as starting materials in the synthesis will also be present on the surface at the end.

The same NCs were treated with hexylamine, in order to study the charge transfer in blends of PbSe NCs and P3HT. The TEM image of hexylamine-treated PbSe NCs is shown in figure 4.13b, where one clearly recognizes the agglomeration tendency compared to original NCs (figure 4.13a). Additionally, the NMR spectra confirm the

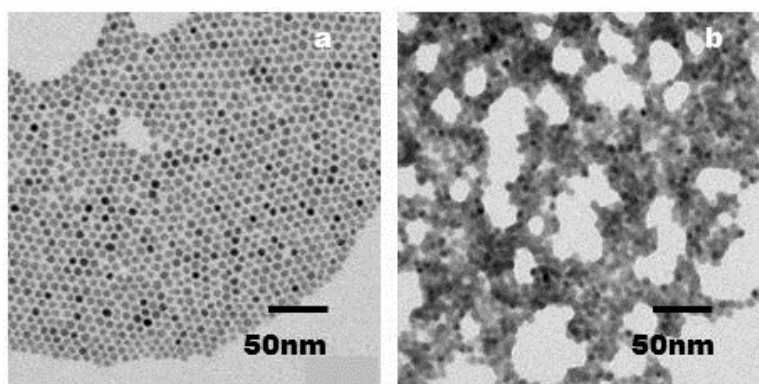


**Figure 4.13:** TEM images of original and hexylamine-treated PbSe NCs - a) Original PbSe NCs and b) hexylamine-treated PbSe NCs.

presence of hexylamine on the surface (figure 4.14b): The signal at 3.7 ppm is indicative for impurities after cleaning with ethanol; The signal at 2.8 ppm is slightly shifted with respect to the signal expected for  $-\text{CH}_2\text{-N}$ ; The signal at 0.9 ppm corresponds to  $\text{CH}_3$  groups; The peaks between 1 ppm and 2 ppm are attributed to  $\text{CH}_2$  groups from amine and ethanol, as well as to the  $\text{NH}_2$  group.

The TGA measurements demonstrate a clear difference between the ligand shell of the original NCs and the one obtained after treatment with hexylamine (figure 4.12b). In the case of the hexylamine-treated PbSe particles, the weight loss appears in the range of 100-200°C, what is in good agreement with the boiling point of hexylamine (132°C). We estimated the surface coverage by organic ligands for the hexylamine-treated NCs, using the method described in references [46] and [110]. The mass fraction of organic material is given by

$$X_{org} = \frac{S_{surf}M_{org}\gamma}{S_{surf}M_{org}\gamma + M_{core}}, \quad (4.10)$$



## 4.4 Surface investigation

where  $S_{surf}$  is the number of Pb surface atoms (see equation (4.1)),  $M_{org}$  is the mass of the organic ligands,  $\gamma$  is so-called "packing factor", the fraction of surface Pb atoms which are bound to coordinating species, and  $M_{core}$  is the mass of the PbSe core. Solving (4.10) for  $\gamma$  gives

$$\gamma = \frac{X_{org}M_{core}}{S_{surf}M_{org} - X_{org}S_{surf}M_{org}}. \quad (4.11)$$

The  $S_{surf}$  term can be calculated as it was described previously (equation (4.1)), the  $X_{org}$  is weight loss during the TGA experiment, and the term  $M_{core}$  is given by

$$M_{core} = \frac{4/3\pi r^3 N MW_{PbSe}}{V N_A}, \quad (4.12)$$

where N is the number of PbSe units per unit cell ( $N = 4$ ),  $MW_{PbSe}$  is the molecular weight of PbSe, V is the volume of a PbSe unit cell,  $N_A$  is Avogadro constant.

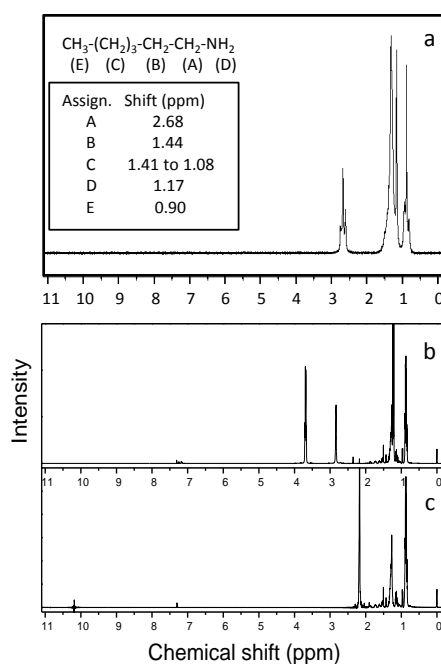


**Figure 4.14: NMR measurement of PbSe NCs** - a) the <sup>1</sup>H NMR (90 MHz) spectrum taken from the SDBS, b) and c) the <sup>1</sup>H NMR spectra of the PbSe after and before ligand exchange, respectively.

Comparison of the overall amount of surface atoms (Pb and Se) with the number of hexylamine per NC yields a surface coverage  $\gamma$  of  $\sim 90\%$ . The latter is comparable with butylamine-treated CdSe NCs [96].

#### 4. HOT-INJECTION SYNTHESIS OF LEAD CHALCOGENIDE NANOCRYSTALS: INFLUENCE OF SYNTHESIS MECHANISM ON THE NANOCRYSTAL SURFACE PROPERTIES

---

In summary, this treatment (of only 30 minutes duration) appears to be a suitable way to obtain PbSe NCs with a high degree of passivation of surface atoms. In contrast to OA-capped CdSe [96], direct ligand exchange from the original ligand shell to alkylamines is possible here, without the necessity to use an exchange with pyridine as an intermediate step [96]. The difference with respect to the CdSe system is probably related to the finding that the initial ligand shell does not consist of intact OA molecules in the case of our PbSe nanocrystals.

#### 4.5 Study of charge transfer in blends of PbSe nanocrystals and P3HT

To characterize the photophysical properties of the hexylamine-treated PbSe particles (figure 4.13b) in a poly-3-hexylthiophene matrix, the samples were investigated by light induced electron spin resonance (l-ESR) and photo-induced absorption spectroscopy (PIA). These results are shown in details in the PhD thesis of Florian Witt (see [8]).

So far, the existence of photo generated charges in such blends was questionable [84]. In figure 4.15, a PIA spectrum taken at 80 K is presented. The main signal

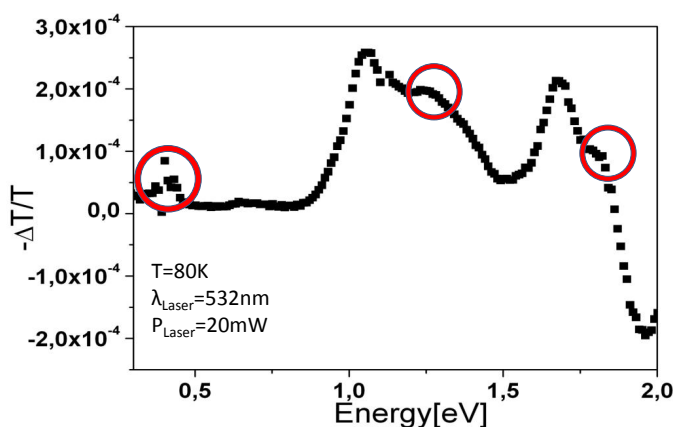


**Figure 4.15: Photoinduced absorption spectrum of a P3HT/PbSe bulk heterojunction film** - Red circles: PIA signature of polaronic transitions in P3HT (taken from [8]).

at 1.1 eV derives from triplet-triplet excitations in P3HT [113]. Alternatively, it was

## 4.5 Study of charge transfer in blends of PbSe nanocrystals and P3HT

---

assigned to interchain singlet excitons in pure P3HT [114]. The feature at about 1.7 eV originates from the photoluminescence of the sample. Additionally, pronounced features at 0.4 eV and 1.25 eV occur. According to previous experiments, these peaks correspond to polaron states in the P3HT phase [114]. The shoulder at 1.8 eV correlates with the signal of delocalized polaron states in the crystalline phase of P3HT. This demonstrates the existence of photoexcited polarons in hybrid blends of P3HT and hexylamine-treated PbSe nanoparticles, however, the ratio between the peak at 1.1 eV and the polaron peaks suggest that large domains of pure P3HT are present. It can be explained by the not optimized intermixing of polymer and nanoparticles as well as by the comparable low amount of PbSe in the film investigated. Note that in typical active layers for hybrid photovoltaics, ten times more particles are used. The signal intensity of the polaron peaks is smaller but in the same order of magnitude as in P3HT/CdSe blends, a system which is commonly used in hybrid photovoltaics as reference [115]. So a sufficiently high amount of charges is already generated in this not yet optimized blend. A possible explanation why in present work, in contrast to reference [84], a charge generation is observed, might be the higher pump laser energy which can be used in our setup. Moreover, our experiment was performed at low temperatures, which increases the charge carrier lifetime and, thus, enhances the experiment's sensitivity.

For further characterization, light induced electron spin resonance spectroscopy at low temperature was performed. Here, the observed spectra are qualitatively similar to the one of the well investigated P3HT:CdSe system [46, 95, 96, 115]. Figure 4.16a shows the l-ESR spectrum of P3HT/PbSe. A pronounced peak related to the polaron signal in P3HT is visible already without light excitation. Upon laser excitation, the signal increases and, after the laser excitation, relaxes back to a level between the dark and the excited spectra. The details are shown in figure 4.16b, where the maximum of the ESR signal is mapped over time. These findings correspond to the results obtained in P3HT/CdSe systems [95], where the large dark signal was interpreted as deep trap states which cannot be depleted with an annealing step at 100°C. In the recombination regime after the excitation, polarons as well as charges from shallow traps recombine, while some intermediate traps do not release charges at 80 K.

Both, l-ESR and PIA studies suggest that a light induced charge transfer occurs at the interface of P3HT and hexylamine-treated PbSe NCs. It is noteworthy in this

#### 4. HOT-INJECTION SYNTHESIS OF LEAD CHALCOGENIDE NANOCRYSTALS: INFLUENCE OF SYNTHESIS MECHANISM ON THE NANOCRYSTAL SURFACE PROPERTIES

---

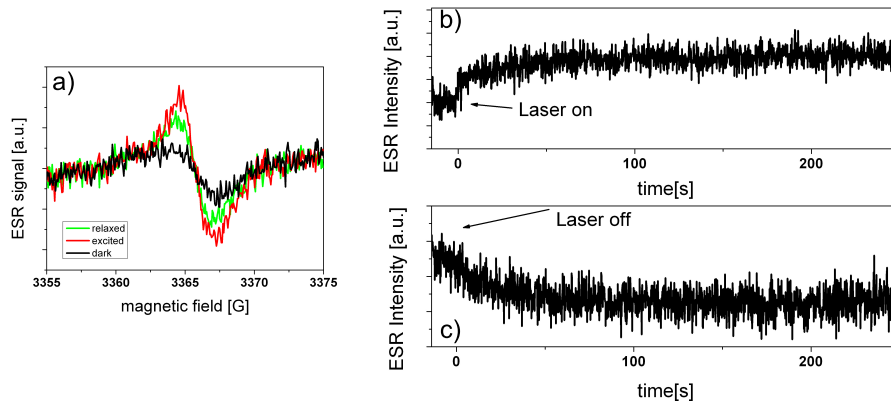


**Figure 4.16: Light induced electron spin resonance spectra of a P3HT/PbSe bulk heterojunction film** - a) Black line: Spectrum taken of relaxed sample in the dark, red line: Sample after 5 min. with laser excitation ( $\lambda_{Laser} = 532$  nm with  $P_{Laser} = 20$  mW), green line: 5min. after ending the laser excitation; b) time dependence of the polaron spin resonance signal under illumination, laser excitation started at 0s.; c) decay dynamics of the same signal. Laser excitation ended at 0s (taken from [8]).

place that I-ESR provided evidence for charge separation, even when blending PbSe NCs surrounded by the original ligand shell with P3HT. This is another indication that the initial ligand shell does not consist of intact OA molecules, but of smaller molecules originating from the decomposition of OA.

In comparison to the CdSe NCs/P3HT system, the signal intensity, meaning the numbers of charge carriers, is smaller in both measurements for PbSe NCs. Here, it should be mentioned that several influencing factors present in the latter system have not been investigated and optimized, yet. Especially, the morphology of the bulk heterojunction layer which was not considered here as well as a not optimized polymer-to-nanoparticle ratio may lead to lower charge generation efficiency. With the help of further blend optimization, e.g., a higher particle concentration, it is expected that the efficiency of charge separation in P3HT/PbSe blends can be improved to compete with other hybrid blends for photovoltaics.

## 4.6 Conclusion

In summary, a colloidal synthesis of nearly monodisperse PbE NCs involving *in situ* formed  $Pb^0$  particles has been introduced. Optimization of the synthesis route has

been performed through the variation of parameters, like the choice of the type of precursors and their concentrations. The mechanism of the synthesis as well as the surface properties were investigated in more detail for PbSe. As an important finding, oleic acid molecules used in the synthesis as stabilizers were finally not detected on the nanocrystal surface. They seem to be decomposed during the synthesis, so that smaller molecules passivate the surface. Nevertheless, the particles are stable in colloidal solution, and all TEM images show well separated NCs. Next, a ligand exchange with hexylamine was applied, and its success was verified by NMR and TGA. Towards the application of the PbSe nanocrystals in hybrid photovoltaics, the charge transfer process between P3HT and PbSe was examined. The ESR and PIA studies of PbSe NCs/P3HT blends suggest that separated charges are successfully produced by photoinduced charge transfer. This makes the NCs promising candidates for using them as electron acceptor component in the active layer in hybrid solar cells.

**4. HOT-INJECTION SYNTHESIS OF LEAD CHALCOGENIDE  
NANOCRYSTALS: INFLUENCE OF SYNTHESIS MECHANISM ON  
THE NANOCRYSTAL SURFACE PROPERTIES**

---

## Chapter 5

# Non-injection synthesis of $\text{In}_2\text{O}_3$ nanoparticles and their shape control

### 5.1 Motivation

Indium oxide is an important n-type transparent semiconductor with a wide direct band gap of about 3.6 eV [36]. It finds application in solar cells [116, 117], highly sensitive gas sensors [33, 34], and optoelectronic devices [118] such as lasers, fluorescent lamps, display devices, and infrared reflectors. Because of the high surface to volume ratio of nanocrystalline materials, sensors using  $\text{In}_2\text{O}_3$  nanocrystals exhibit superior performance, compared with that of thin film devices. In particular nanostructured sensors show higher sensitivity and shorter response time, furthermore they can be operated at much lower temperatures. Because the properties of materials in the nanometer range strongly depend on their size, synthesis of well-defined indium oxide nanoparticles is of considerable interest for both fundamental studies and technological applications. Up to now, various methods have been developed for the synthesis of indium oxide nanoparticles ( $\text{In}_2\text{O}_3$  NPs), like thermal evaporation, calcinations process, laser ablation in liquids technique, thermolysis, hot-injection technique, solvothermal, and hydrothermal methods [37, 82, 119, 120, 121, 122, 123, 124]. The thermolysis of metal-organic precursors is one of the solution-based synthetic routes in producing  $\text{In}_2\text{O}_3$  NPs. Spherical  $\text{In}_2\text{O}_3$  NPs have been synthesized by decomposition of indium

## 5. NON-INJECTION SYNTHESIS OF $\text{In}_2\text{O}_3$ NANOPARTICLES AND THEIR SHAPE CONTROL

---

acetylacetonate in oleylamine [56]. A modified method has been used to produce the octahedral  $\text{In}_2\text{O}_3$  NPs capped with oleic acid [82]. Other works have reported on using a long chain alcohol with or without carboxylic acids [37, 125].

In this chapter a simple and fast non-injection synthesis of  $\text{In}_2\text{O}_3$  NPs is reported that involves indium acetate ( $\text{Inac}_3$ ) decomposition in oleylamine under inert atmosphere. Furthermore, two different strategies of shape control of  $\text{In}_2\text{O}_3$  NPs were studied. The first one involves the use of additional organic ligand molecules, to change the reactivity of the In precursor and to better passivate the surface of the nanocrystals, which is a widely used approach in colloidal chemistry. The other strategy does not affect the reactivity of the In precursor, but changes mainly the growth process of the nanocrystals, by the adsorption of additional cations on the surface of the emerging particles.

### 5.2 Synthesis investigation and characterization of flower-shaped $\text{In}_2\text{O}_3$ nanoparticles

Synthesis of indium oxide nanoparticles can lead to a variety of particle shapes through changes of the reaction conditions. The flower-shaped  $\text{In}_2\text{O}_3$  NPs shown in figure 5.1

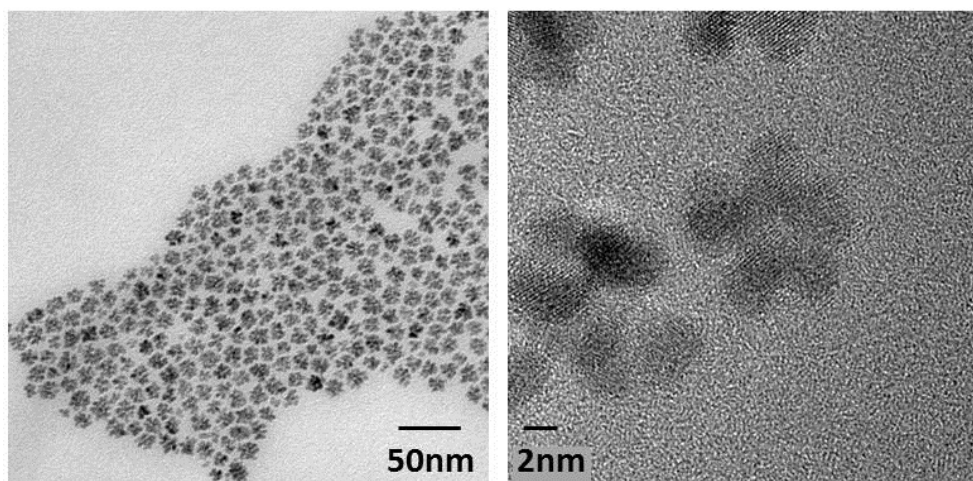


**Figure 5.1:** TEM and HRTEM images of the  $\text{In}_2\text{O}_3$  NPs produced by the reaction of indium (III) acetate with oleylamine - The nanoparticles have flower shape.

were produced by heating indium acetate in oleylamine.



## 5.2 Synthesis investigation and characterization of flower-shaped $\text{In}_2\text{O}_3$ nanoparticles

The x-ray diffraction pattern of the flower-shaped nanoparticles is shown in figure 5.2 together with the results of its Rietveld refinement. The pattern can be assigned

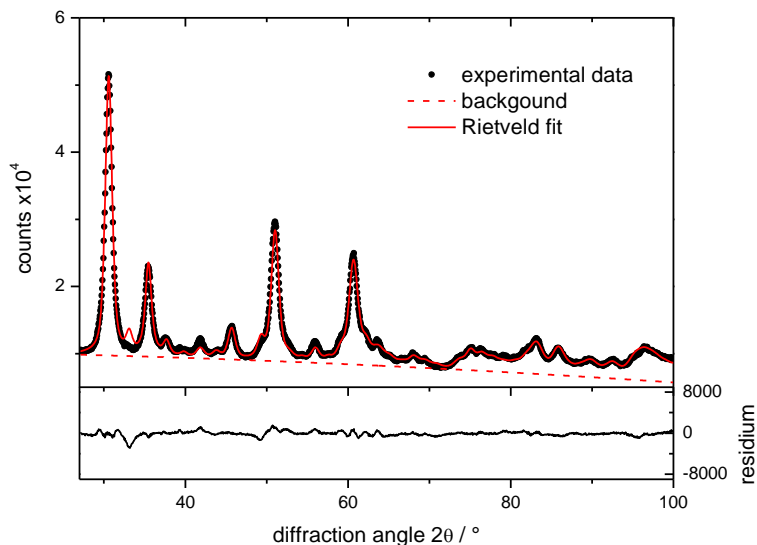


**Figure 5.2:** Powder X-ray diffraction patterns of flower-shaped  $\text{In}_2\text{O}_3$  nanoparticles produced by heating indium (III) acetate with oleylamine - The pattern can be assigned to cubic  $\text{In}_2\text{O}_3$ .

to cubic  $\text{In}_2\text{O}_3$ . The lattice parameter was refined to  $10.127 \text{ \AA}$ , which is in agreement with the bulk value. The reflections are broadened, indicating the nanocrystalline nature of the sample. The morphology of the nanocrystals and their preferred orientation was estimated using size/shape, and texture models. Using an anisotropic model for the spatial extension of the crystallites resulted in some differences for the size along different crystallographic directions. Because of the irregular shape of the nanoflowers, it is, however, difficult to assign these results to certain structural characteristics of the nanocrystals. A mean value of  $\sim 10 \text{ nm}$  ( $\pm 1 \text{ nm}$  for different crystallographic directions) obtained from these calculations is smaller than the diameter of the nanoflowers obtained from the analysis of the TEM images ( $17 \pm 4 \text{ nm}$ ). It is, however, larger than the size of the arms of the flower shaped particles. This indicates that the small

## 5. NON-INJECTION SYNTHESIS OF $\text{In}_2\text{O}_3$ NANOPARTICLES AND THEIR SHAPE CONTROL

---

nanocrystals forming the nanoflowers are not randomly oriented, but at least partly grown together to larger crystalline domains. Concerning texture effects, refinement indicated a tendency for (100) planes to be preferentially oriented parallel to the sample holder.

At the beginning of the synthesis the mixture of indium acetate and oleylamine becomes transparent because indium precursor dissolves in solvent. Then yellowish color appears what indicates the formation of the  $\text{In}_2\text{O}_3$  NPs. During the reaction several samples were taken which were studied by transmission electron microscopy (TEM), nuclear magnetic resonance (NMR), absorption, and PL spectroscopy. The formation of  $\text{In}_2\text{O}_3$  nanocrystals with flower shape was observed after the temperature reached  $120^\circ\text{C}$ . According to the absorption spectra the concentration of the particles increases by heating (figure 5.3). The onset of the absorption spectra shifts to the red with the reaction time, due to the size quantization effect.

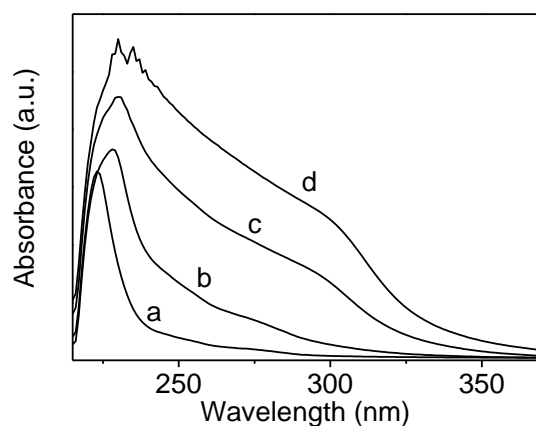


**Figure 5.3:** Absorption spectra of the samples taken from the reaction between indium acetate and oleylamine - a - at 2 min,  $116^\circ\text{C}$ ; b - at 3 min,  $190^\circ\text{C}$ ; c - at 4 min,  $240^\circ\text{C}$ , d - at 30 min,  $240^\circ\text{C}$  (this sample was diluted 16 times).

Photoluminescence (PL) of the as-synthesized  $\text{In}_2\text{O}_3$  NPs during the growth process was measured at room temperature. Bulk  $\text{In}_2\text{O}_3$  shows no detectable emission at room temperature [126]. For the nanoparticles, however, a luminescence maxima appear in a visible region as it is shown in figure 5.4. These peaks situated at 409nm, 422nm, 456nm, and 505nm are strongly red shifted compared with the absorption onset. That

## 5.2 Synthesis investigation and characterization of flower-shaped $\text{In}_2\text{O}_3$ nanoparticles

is why the emission is more likely due to defect states, then the bandgap recombination. This luminescence maxima appear due to oxygen vacancies, which is in accordance with other reports on PL observed in different  $\text{In}_2\text{O}_3$  nanostructures [82].

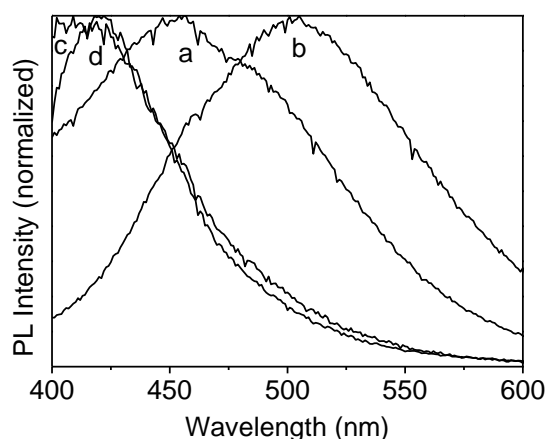


**Figure 5.4: PL spectra of the samples taken from the reaction between indium acetate and oleylamine** - a - at 2 min (excitation 275nm); b - at 3 min (excitation 275nm); c - at 4 min (excitation 350nm); d - at 30 min (excitation 350nm).

For a better understanding of the synthesis mechanism the reaction was followed by NMR analysis. Figure 5.5 shows the  $^{13}\text{C}$  NMR spectra of the samples taken during the reaction. Most of the peaks show the presence of pure oleylamine, but in the course of the synthesis there are a few changes. At the beginning of the reaction indium acetate  $(\text{CH}_3\text{COO})_3\text{In}$  can be detected (according to the peak at 178.83 ppm for  $-\text{COO}-$  (peak 1 in figure 5.5a)). After some time additional signals appear which indicate the formation of N-oleylacetamide  $\text{CH}_3-\text{CO}-\text{NH}-\text{CH}_2-\text{C}_{17}\text{H}_{33}$  (a peak at 170.28 ppm (1') for  $-\text{CO}-\text{NH}-$  and a peak at 40.01 ppm (2) for  $-\text{NH}-\text{CH}_2-$  (figure 5.5b)). In the end of the reaction the acetate disappears (figure 5.5c). The samples were also analyzed using  $^1\text{H}$  and 2D ( $^1\text{H}, ^1\text{H}$  and  $^{13}\text{C}, ^1\text{H}$ ) NMR spectroscopy which prove this interpretation of  $^{13}\text{C}$  NMR spectra. Based on the analysis of the NMR data we can conclude that oleylamine is converted to oleylamide during the nanoparticle formation:



Thus, oleylamine is not only a solvent, but it also plays a role in the formation of  $\text{In}_2\text{O}_3$  nanoparticles. Additionally, it serves as a stabilizer. Particles synthesized in a control

## 5. NON-INJECTION SYNTHESIS OF $\text{In}_2\text{O}_3$ NANOPARTICLES AND THEIR SHAPE CONTROL

---

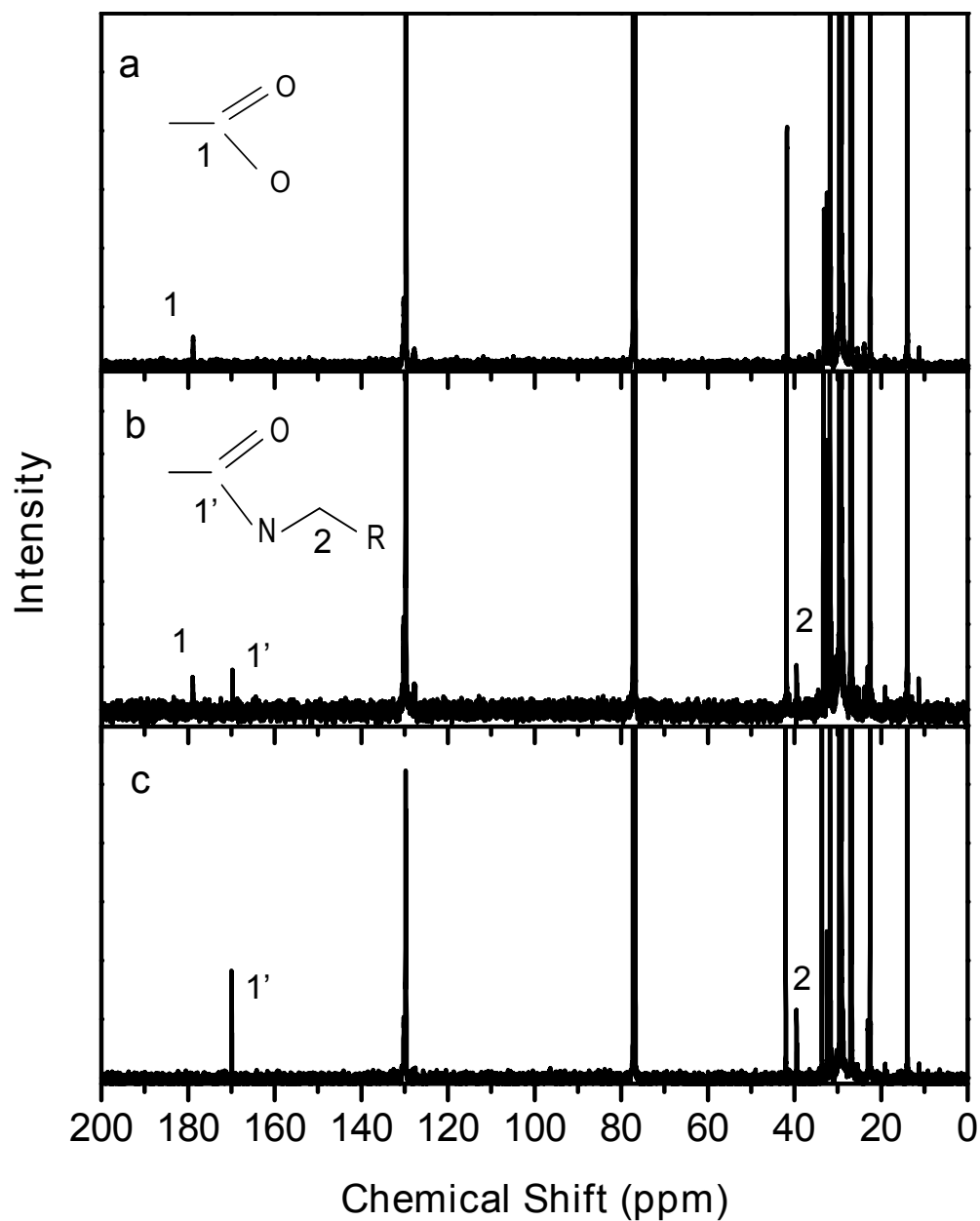


Figure 5.5: NMR spectra of the samples taken from the reaction between indium acetate and oleylamine - 1 - at 3min, 190°C; 2 - at 4min, 240°C; 3 - at 30 min, 240°C.

### 5.3 Shape control of $\text{In}_2\text{O}_3$ nanoparticles using organic ligand molecules

experiment with octadecene (a non-coordinating solvent) used instead of oleylamine did not form a stable colloidal solution.

### 5.3 Shape control of $\text{In}_2\text{O}_3$ nanoparticles using organic ligand molecules

In the next step the possibility to control the shape of  $\text{In}_2\text{O}_3$  NPs has been evaluated by employing additional stabilizers such as trioctylphosphine oxide (TOPO) and oleic acid (OA). Both molecules are hard Lewis bases and should affect the reactivity of the

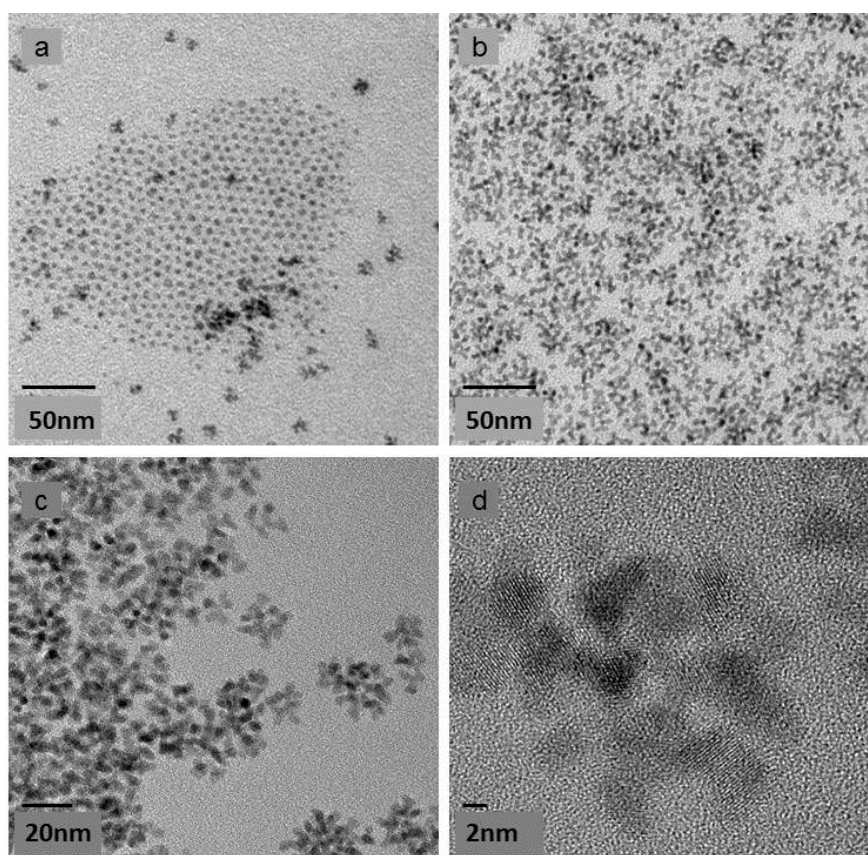


**Figure 5.6:** TEM image of  $\text{In}_2\text{O}_3$  NPs synthesized using organic ligand for stabilization - a) TOPO, b) OA with ODE as a non-coordinating solvent, c) and d) OA with OLA as a coordinating solvent.

indium precursor in the reaction. The addition of TOPO changed the shape of the nanocrystals, however the sample was not uniform and quasi-spherical particles were

## 5. NON-INJECTION SYNTHESIS OF $\text{In}_2\text{O}_3$ NANOPARTICLES AND THEIR SHAPE CONTROL

---

found together with flower-like nanocrystals (figure 5.6a). When the amount of TOPO was increased, indium hydroxide ( $\text{In}(\text{OH})_3$ ) was formed together with  $\text{In}_2\text{O}_3$  (figure 5.7).

Oleic acid turned out to reduce the branching of the nanoflowers (figure 5.6b-c). OA can also effectively stabilize  $\text{In}_2\text{O}_3$  NPs, which could be shown in an experiment with octadecene as solvent (figure 5.6b).

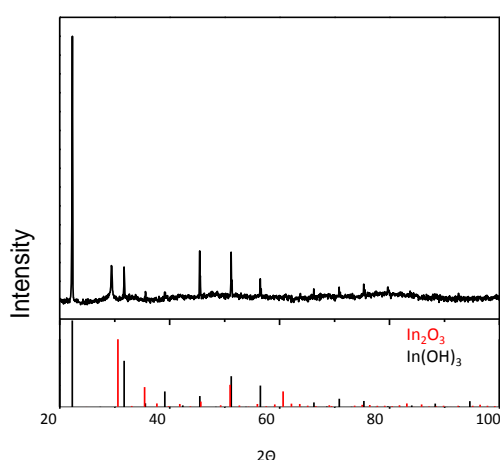


**Figure 5.7:** XRD of  $\text{In}_2\text{O}_3$  NPs synthesized with increased amount of TOPO - Indium hydroxide was formed.

Thus, reducing the activity of In cations by additional stabilizers can be applied, in order to control the shape of  $\text{In}_2\text{O}_3$  nanocrystals, however this method has some limitations: If the reactivity of the In precursor is too low,  $\text{In}(\text{OH})_3$  is formed instead of spherical  $\text{In}_2\text{O}_3$  nanocrystals.

### 5.4 Shape control of $\text{In}_2\text{O}_3$ nanoparticles using copper ions

In the next step another strategy of shape control was investigated. Instead of using organic molecules in order to slow down the growth process of nanocrystals, additional cations were applied in the synthesis. When copper salts such as copper (I) acetate ( $\text{Cuac}$ ), copper (II) acetate ( $\text{Cu}(\text{ac})_2$ ), copper (II) acetylacetonate ( $\text{Cu}(\text{acac})_2$ ), or copper (I) chloride ( $\text{CuCl}$ ) were employed in the synthesis of  $\text{In}_2\text{O}_3$ , nearly monodisperse quasi-spherical nanoparticles were produced (figure 5.8a-d).

#### 5.4 Shape control of $\text{In}_2\text{O}_3$ nanoparticles using copper ions

The reaction with Cuac was studied in more detail. During the reaction the color of the mixture changes from blue at the beginning, due to the presence of the copper ions, to green and subsequently yellow, indicating a complex formation between copper, indium and oleylamine [127]. When the temperature increases, the mixture darkens. That is explained by the decomposition of the complexes and the formation of indium oxide and copper nanoparticles.

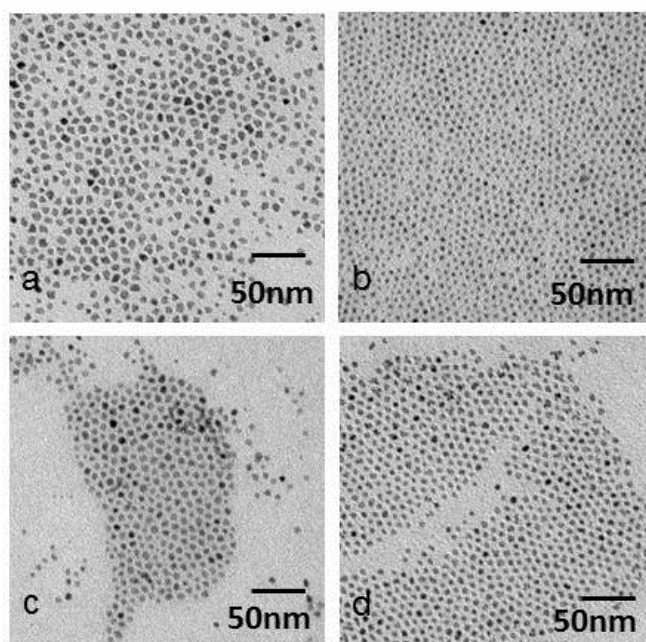


**Figure 5.8:** TEM images of  $\text{In}_2\text{O}_3$  nanoparticles synthesized using  $\text{Inac}_3$  and different copper salts - a) Copper (I) acetate, b) copper (II) acetylacetonate, c) copper (II) acetate, d) copper (I) chloride.

The XRD patterns show that the product of the reaction consists of two types of NPs: metallic copper and indium oxide nanoparticles (figure 5.9). No contribution of other phases, such as copper indium oxide, was observed. The Rietveld analysis of the diffraction pattern of this sample shows, that the presence of copper ions during the growth does not influence the crystallographic structure of the  $\text{In}_2\text{O}_3$  NPs. The refined value of the lattice parameter is 10.125 Å, which is almost the same as the value obtained for the flower-like particles synthesized without copper ions.

The yellowish color of the  $\text{In}_2\text{O}_3$  NPs can be observed only after the centrifugation of the reaction solution, which can be applied to separate the Cu particles (figure 5.10).

## 5. NON-INJECTION SYNTHESIS OF $\text{In}_2\text{O}_3$ NANOPARTICLES AND THEIR SHAPE CONTROL

---

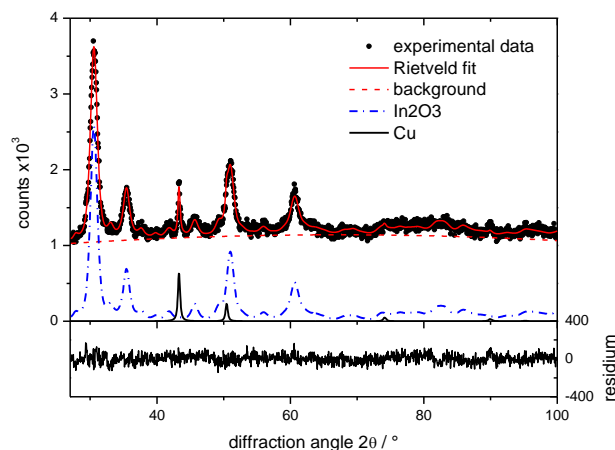


**Figure 5.9: X-ray diffraction pattern of the  $\text{In}_2\text{O}_3$  nanoparticles produced by employing of Cuac together with copper particles** - The XRD patterns show that the product of the reaction consists of two types of NPs.

The EDX measurement of the  $\text{In}_2\text{O}_3$  NPs was carried out after their separation from

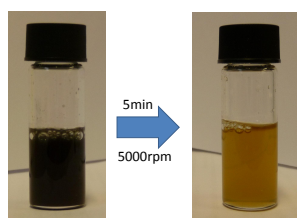


**Figure 5.10: Separation of  $\text{In}_2\text{O}_3$  and Cu NPs through centrifugation** - The flask with the solution after the synthesis is dark-red, but after centrifugation the solution is yellow.

Cu nanoparticles. It was found that  $\text{In}_2\text{O}_3$  NPs do not consist copper (figure 5.11).

Using an anisotropic model for the spatial extension of the crystallites resulted in some differences for the size along different crystallographic directions: values between 7 nm and 11 nm were found (figure 5.9). This is in good agreement with the results of the analysis of the TEM images (figure 5.8a). The particles have a slightly elongated shape, with an aspect ratio of  $1.3 \pm 0.2$ . The longer axis of the nanocrystals was found to be  $10.4 \pm 2$  nm, the shorter  $7.8 \pm 1.5$  nm.



## 5.4 Shape control of $\text{In}_2\text{O}_3$ nanoparticles using copper ions

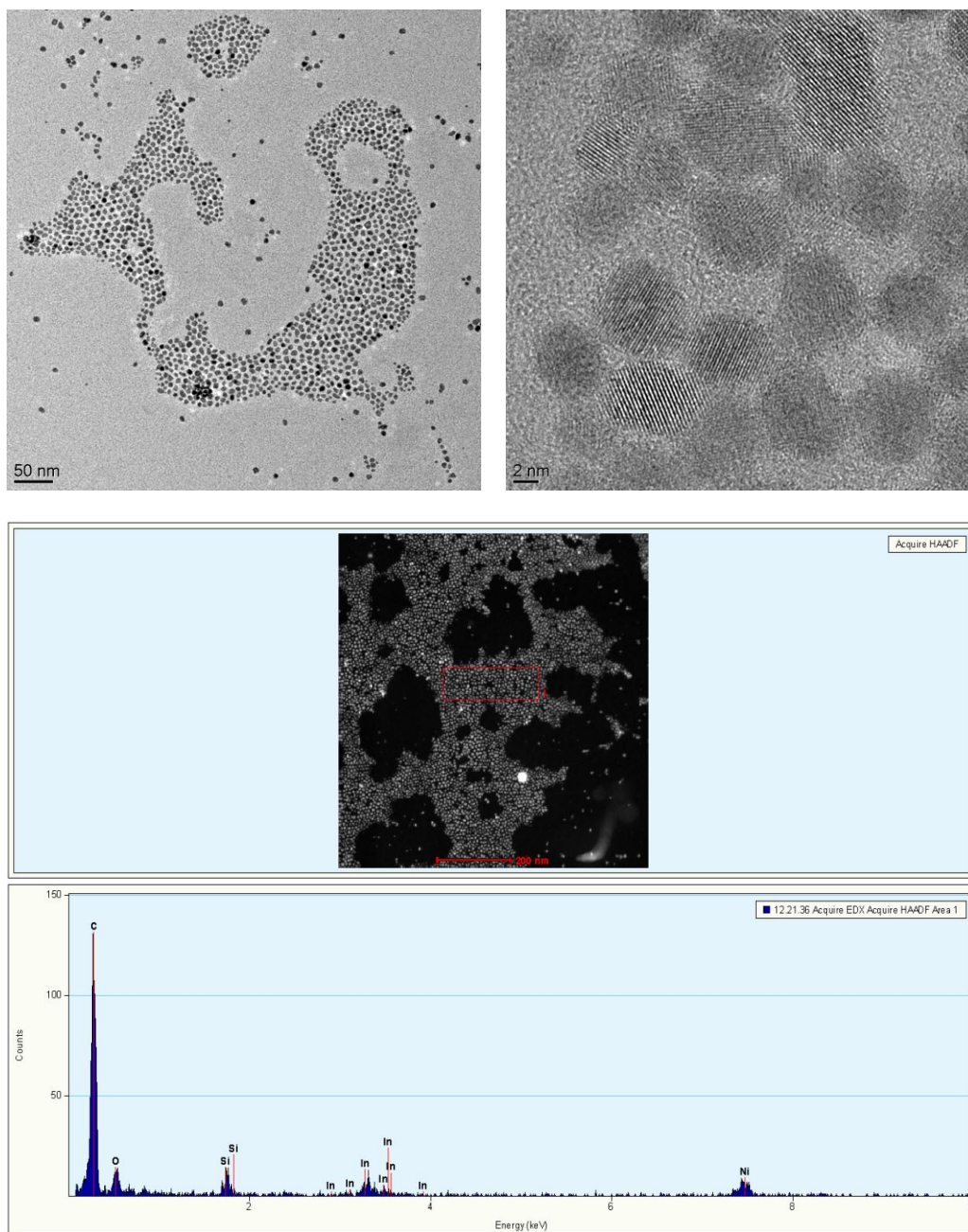
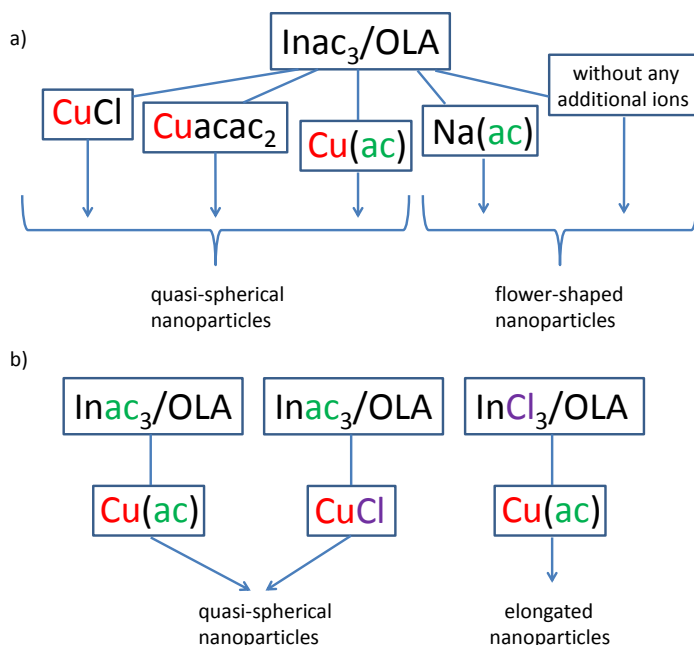


Figure 5.11: TEM and HRTEM images as well as EDX measurement of  $\text{In}_2\text{O}_3$  NPs -  $\text{In}_2\text{O}_3$  NPs do not consist copper.

## 5. NON-INJECTION SYNTHESIS OF $\text{In}_2\text{O}_3$ NANOPARTICLES AND THEIR SHAPE CONTROL



**Figure 5.12: Scheme of the reaction - Influence of copper ions.**

The presence of copper ions during the initial nucleation and growth process of the nanocrystals and their concentration play an important role in the synthesis. If a too low concentration of  $\text{Cuac}$  was employed, the formation of  $\text{In}_2\text{O}_3$  NPs with flower shape was observed. Changing the copper salt (copper (II) acetate, copper (II) acetylacetonate, copper (I) chloride) did not significantly affect the final shape or size distribution, it influenced, however, the size of the nanocrystals (figure 5.8a-d). In order to compare different samples we measured the area of the particles in the TEM images and calculated their diameter assuming a spherical shape. The smallest particles ( $3.7 \pm 0.6$  nm) were obtained with copper (II) acetylacetonate (figure 5.8b), the biggest with copper (I) and copper (II) acetate ( $8.1 \pm 1.5$  nm and  $5.4 \pm 1$  nm respectively) (figure 5.8a and c). When sodium acetate [128] was used in a control reaction, the resulting  $\text{In}_2\text{O}_3$  NPs were flower-shaped. This indicates that in the concentration range studied here the additional anions do not influence the shape of the resulting nanocrystals. So, the shape control mechanism involves the copper cations (figure 5.12). It has been shown by Farvid et al. [35] that the presence of  $\text{Cr}^{3+}$  or  $\text{Mn}^{3+}$  ions in the reaction mixture can influence the shape and the crystallographic structure of nanocrystals. The adsorption of the dopant to the surfaces of colloidal  $\text{In}_2\text{O}_3$  nanocrystals inhibits the nanocrystal

growth. We assume an analogous mechanism to be responsible for shape control under our reaction conditions.

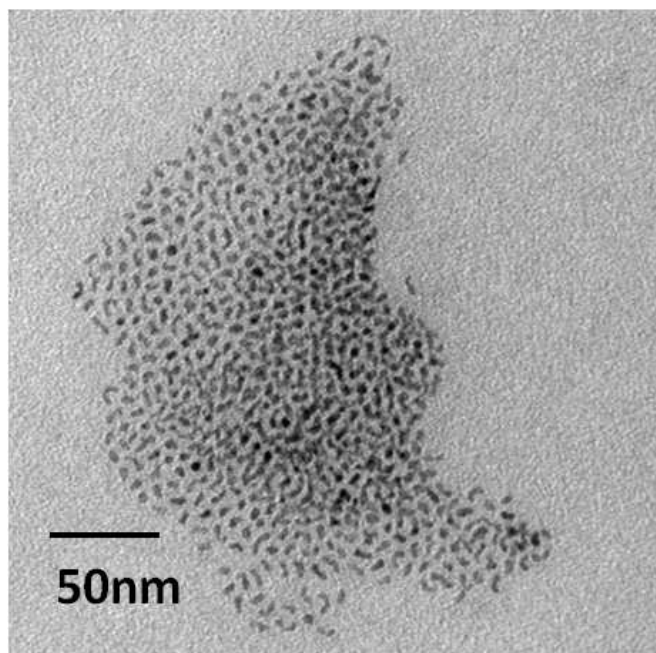


**Figure 5.13:** TEM image of the  $\text{In}_2\text{O}_3$  nanoparticles synthesized using copper (I) acetate and indium (III) chloride - Elongated  $\text{In}_2\text{O}_3$  particles.

When indium chloride was used as indium precursor in the synthesis employing copper (I) acetate, formation of elongated shapes was observed (figure 5.13). In this reaction the concentration of chloride ions is three times higher, then in the reaction of indium acetate with copper (I) chloride. Chloride ions strongly bind to both indium and copper atoms and reduce their activity. Thus, the shape control by copper ions is less pronounced, because less copper ions can bind to the surface of the growing  $\text{In}_2\text{O}_3$  NPs. On the other hand, the reactivity of the In ions is also lowered, compared with reactions with indium acetate only. This results in the generation of elongated particles instead of flower-shaped.

## 5.5 Conclusion

In summary, uniform, flower-shaped, branched  $\text{In}_2\text{O}_3$  nanocrystals were obtained by heating indium acetate in oleylamine. Oleylamine not only plays a role as solvent

## 5. NON-INJECTION SYNTHESIS OF $\text{In}_2\text{O}_3$ NANOPARTICLES AND THEIR SHAPE CONTROL

---

and stabilizer in this reaction, but it also takes an active part in the formation of indium oxide, as could be shown by NMR analysis of the reaction solution. This kind of a non-injection synthesis can be easily scaled up and is suitable for synthesizing large quantities of nanomaterials. The flower shaped nanocrystals have a large surface area, which makes them an interesting material for sensor applications. The degree of branching of the nanocrystals could be controlled by using additional organic ligands, which reduced the activity of the indium precursor. Apart from this classical approach of shape control of nanomaterials, we also studied the possibility to control the shape of  $\text{In}_2\text{O}_3$  nanocrystals by the addition of other cations. The presence of copper ions in the synthesis turned out to be suitable to influence the shape of the indium oxide nanocrystals, without changing their crystallographic structure.

## Chapter 6

# Synthesis and characterization of CIS/Au hybrid nanoparticles

### 6.1 Motivation

Hybrid nanostructures are of high interest in academic research. The presence of different materials in one system opens up many possibilities to change properties from these of each single component or of their physical blend [10, 42, 76, 129]. Due to such unique opportunity, hybrid nanomaterials find wide applications in physical, chemical, and biological research [31, 41, 42, 130, 131].

Metal-semiconductor hybrid nanostructures are one important class of these multifunctional materials. A direct contact between a metal nanocrystal and a semiconductor nanoparticle facilitates charge separation after exciton generation in the semiconductor [132], which might be useful for solar energy conversion [29] and heterogeneous catalysis [133]. The metal part can be used to apply an electrical contact to the hybrid structure and to increase the electrical conductance of nanomaterials, which is important for opto-electronic devices [134]. Directly connecting metal and semiconductor nanoparticles together gives an opportunity to influence the optical properties of both materials. The plasmon resonance of metal nanocrystals can be shifted [42], as well as the photoluminescence intensity of semiconductor nanoparticles can be changed [42, 44], the latter could be interesting for applications in biological detection. Furthermore, self-assembly methods already well developed for metal nanocrystals can be applied to form superstructures of semiconductor-metal hybrid materials [44]. Thus,

## 6. SYNTHESIS AND CHARACTERIZATION OF CIS/AU HYBRID NANOPARTICLES

---

hybrid nanostructures possess characteristics making them suitable building blocks for the development of nanomaterial-based devices.

The synthesis route of the growth of gold nanocrystals onto semiconductor nanoparticles was reported by Mokari et al. [44]. CdSe nanorods and tetrapods react with gold stock solution yielding CdSe/Au hybrid nanostructures. This simple synthetic method can be applied for many systems, such as CdS [134, 135], CdTe [42], PbS [29, 43, 136], PbSe [43] nanomaterials. The mechanism is shown in figure 6.1.

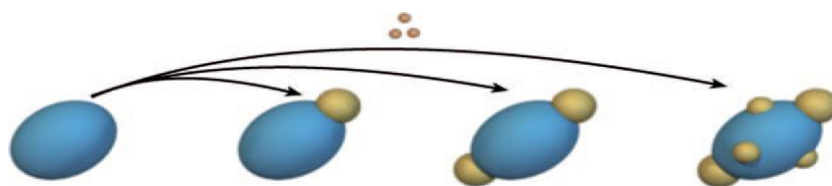


**Figure 6.1: Scheme of growth mechanism in the synthesis of hybrid nanostructures** - Surface nucleation and growth of metal onto semiconductor nanoparticle (taken from [55]).

The semiconductor nanoparticles serve as seeds, and the metal nanocrystals grow on their surface. The characteristic parameters of seeds are important already in the nucleation stage. Small nanoparticle is more reactive than the bigger one, because the latter has lower chemical potential according to the Gibbs-Thompson equation. Consequently, the metal phase grows faster onto the small semiconductor nanoparticle [10]. The shape of the seeds also influences the synthesis process. In the case of semiconductor nanorods the metal NCs grow on the nanorod tips first, because they have higher surface energy and, thus, higher reactivity to compare with nanorod sidewall [42, 44]. Furthermore, the ligand coverage of the nanorod tips is poor. So, the metallic monomer can achieve the seed surface there easier [73, 137]. Additionally, the seed surface facets determine where the metal nanocrystals will grow. So, the CdE nanorods have cadmium-rich facet on one end and chalcogenide-rich facet on the opposite end. Due to larger metalchalcogenide bond enthalpy, the growth of metal occurs preferably on the chalcogenide-rich tips [10, 42]. Besides these parameters, the surface defects provide high surface energy and, therefore, facilitate the metal growth there [42].

In the growth stage the concentration ratio of seeds to monomer is important. When the metal monomer concentration is high, the diffusion process similar to Ost-

wald ripening occurs e.g. during the CdSe/Au nanostructure synthesis, that leads to growth of bigger Au nuclei while the smaller disappear [138]. This experimental results could be reproduced by Monte Carlo simulation [138]: The nuclei grow equally at high concentration, then with decreasing concentration the ripening process leads to dissolving small particles and growing the big one.

Since the hybrid materials containing cadmium and lead chalcogenide as well as their synthesis mechanism are well studied, an investigation of the formation mechanism and properties of hybrid nanostructures based on ternary I-III-VI semiconductor nanocrystals was carried out in this work. In order to avoid the toxicity of cadmium and lead chalcogenides, the scientific research tends generally to alternative semiconductor materials such as ternary I-III-VI semiconductor nanocrystals [80, 139, 140, 141]. However, the formation of metal-I-III-VI-semiconductor hybrid materials has been reported just once (CIGS/Au), recently [142].

As it was described in Chapter 2 the ternary nanoparticles belong to more complicated materials compared with binary compounds. This influences not only their properties, but also the synthesis procedure, where more precursors need to be applied as well as stabilizers need to control the reactivity of each monomer in order to avoid the formation of binary nanoparticles, but also to produce the nanoparticles with different elemental composition. Due to many possibilities of the properties variation for ternary materials, their use as the seeds in the hybrid nanostructure synthesis opens the opportunity to study the mechanism of metal-I-III-VI-semiconductor hybrid nanomaterial formation that is of fundamental interest for the research in the emerging field of hybrid nanostructures.

In this work, experiments on the growth of gold nanocrystals (Au NCs) onto quaternary I-III-VI copper indium sulfide selenide nanoparticles (CuInSSe NPs) are presented and compared with results obtained with pure copper indium disulfide nanoparticles (CuInS<sub>2</sub> NPs). The growth behavior of gold nanocrystals as well as the structure and the optical properties of resulting nanostructures were studied by transmission electron microscopy (TEM), energy dispersive x-ray analysis (EDX), X-ray diffraction (XRD), and UV-Vis absorption spectroscopy.

## 6. SYNTHESIS AND CHARACTERIZATION OF CIS/AU HYBRID NANOPARTICLES

---

### 6.2 Synthesis and characterization of CuInSSe nanoparticles

The original semiconductor CuInSSe nanoparticles are shown in figure 6.2. They have trigonal pyramidal shape and an average size of  $5.5 \pm 0.8$  nm. The synthesis route was similar to the one for CuInSe<sub>2</sub> NPs developed by Zhong et al. [85], where CuCl and InCl<sub>3</sub> were used as copper and indium precursors, DDT as the ligand, and ODE as the non-coordinating solvent. Changing the concentration of DDT as well as the molar ratio of Cu (or In) to Se precursors leads to formation of CuInSSe NPs. Keeping the other

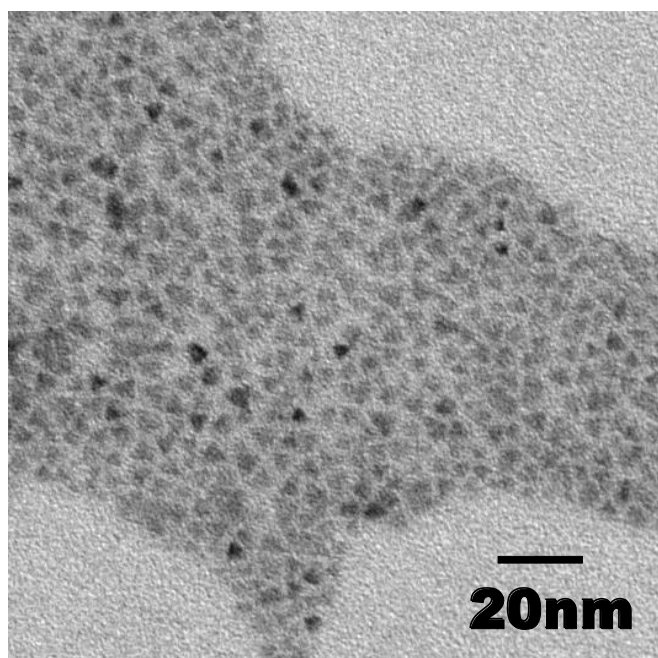


**Figure 6.2:** TEM image of the CuInSSe NPs - The nanoparticles have trigonal pyramidal shape.

conditions the same, the average size almost did not change; the CuInSe<sub>2</sub> NPs from ref. [85] had an average size of 6 nm. But the element ratio was changed. According to energy dispersive x-ray (EDX) analysis (figure 6.3), the ratio Cu:In:S:Se was found to be 0.86:1:0.65:1.35, while Zhongs nanoparticle composition was Cu<sub>1</sub>In<sub>1.1</sub>Se<sub>1.6</sub> according to inductively coupled plasma atomic emission spectroscopy (ICP-AES) [85]. Thus, in this reaction the thiols partly decompose and serve as a sulfur source for the reaction.

The structure and the composition of CuInSSe NPs were further investigated with



## 6.2 Synthesis and characterization of CuInSSe nanoparticles

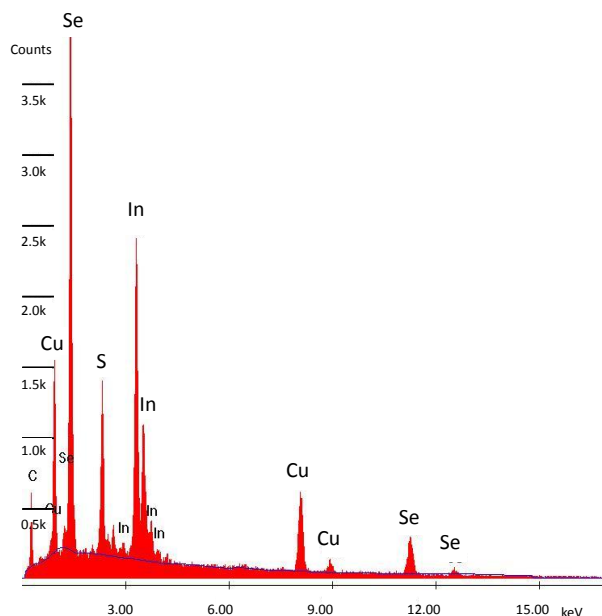


**Figure 6.3: EDX measurement of the CuInSSe NPs** - The ratio Cu:In:S:Se was found to be 0.86:1:0.65:1.35.

powder x-ray diffraction. At room temperature, bulk I-III-VI semiconductors crystallize in the chalcopyrite structure, which is a superstructure of the zinc blende type with a  $a/c$  ratio of 2 [143]. At higher temperatures, the cations disorder in the cation sublattice, and the chalcopyrite structure reverts to a zinc blende structure. In contrast to the bulk materials, nanocrystalline I-III-VI semiconductors form stable cation disordered polymorphs with zinc blende or wurtzite structure also at room temperature [144, 145, 146]. The Rietveld analysis of the XRD pattern of our CuInSSe NPs revealed that they crystallize in the zinc blende structure (figure 6.4). The lattice parameter was refined to 5.72 Å. This value lies between the lattice parameters for CuInS<sub>2</sub> and CuInSe<sub>2</sub> (5.52 Å and 5.78 Å, respectively). Assuming a linear dependence of the lattice parameters on the composition, we determined the fraction of the S atoms incorporated into the lattice of the CuInSSe particles to be 0.27. Such a value is smaller than the one obtained from EDX measurements (0.48), which gives an indication for a sulfur rich surface. The latter is a reasonable assumption, because of the presence of thiols (DDT) in the reaction solution which bind to the CuInSSe surface and form the ligand shell.

As is obvious from the TEM images, the particles do not have a preferential growth

## 6. SYNTHESIS AND CHARACTERIZATION OF CIS/AU HYBRID NANOPARTICLES

---

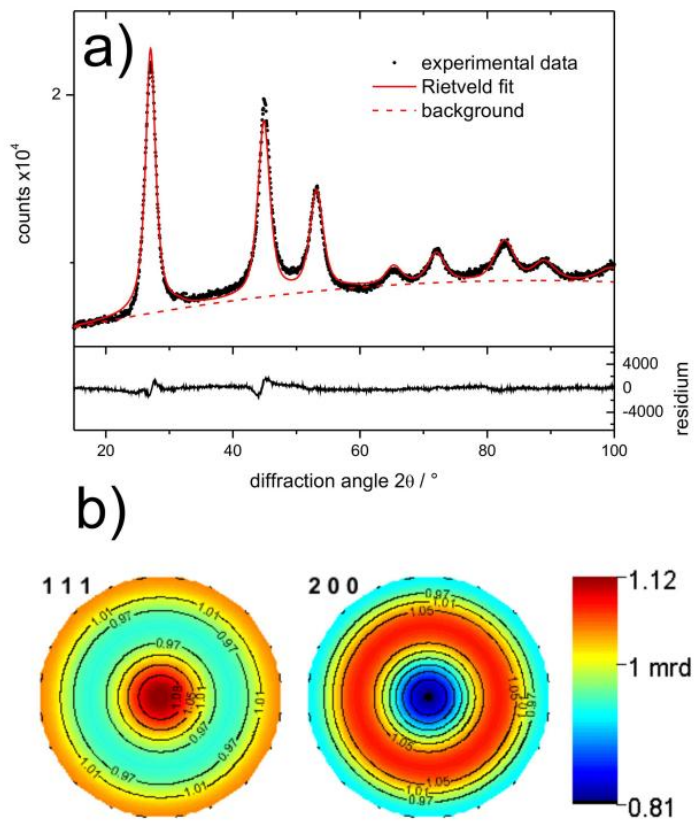


**Figure 6.4:** Powder X-ray diffraction patterns of the CuInSSe NPs - a) The experimental data (dots) is plotted together with a Rietveld fit (red line); b) Reconstructed pole figures resulting from refinement according to the applied texture model. The (111) planes have a high probability to be oriented parallel to the sample holder.

### 6.3 Synthesis and characterization of CuInSSe/Au hybrid nanostructures

direction. Thus, we used an isotropic model for determining the sizes of the crystallites. The value of 6.3 nm is in good agreement with the size obtained from TEM. Figure 6.4 shows a reconstructed pole figure deduced from the texture analysis of the sample. In the TEM images, the particles which have a tetrahedral shape lay on one of the (111) surfaces terminating the tetrahedron. This indicates that texture effects might be found in the XRD patterns. Indeed, the poles of the (111) lattice planes are found primarily in the center of the projection plane, indicating that the (111) planes are preferentially oriented parallel to the sample holder.

The absorption spectrum is shown in figure 6.5. Compared to the values for the

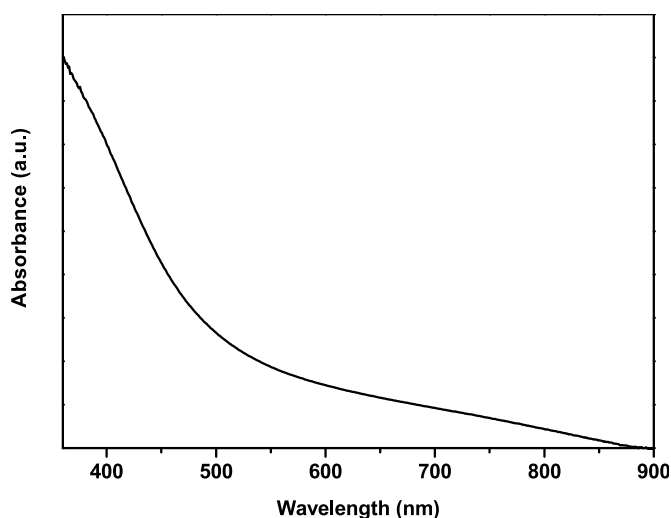


**Figure 6.5: Absorption spectrum of the original CuInSSe NPs** - The band gap of the CuInSSe NPs is blue-shifted due to the quantum confinement effect.

bulk materials (1.04 eV for CuInSe<sub>2</sub> [147] and 1.53 eV for CuInS<sub>2</sub> [127]) the band gap of our CuInSSe NPs is blue-shifted due to the quantum confinement effect.

### 6.3 Synthesis and characterization of CuInSSe/Au hybrid nanostructures

The resulting hybrid nanostructures are shown in figure 6.6. Comparison with the original CuInSSe NPs shows that the size and the shape of the nanocrystals did not significantly change after the reaction with gold, the size of the semiconductor part is  $4.2\pm 0.8$  nm. However, after the reaction between CuInSSe and gold precursor solution

## 6. SYNTHESIS AND CHARACTERIZATION OF CIS/AU HYBRID NANOPARTICLES

---

particles with a higher contrast can be found on the vertexes of pyramidal CuInSSe NPs. The size of these particles was estimated to be  $2.3\pm 0.4$  nm. Apparently Au NPs

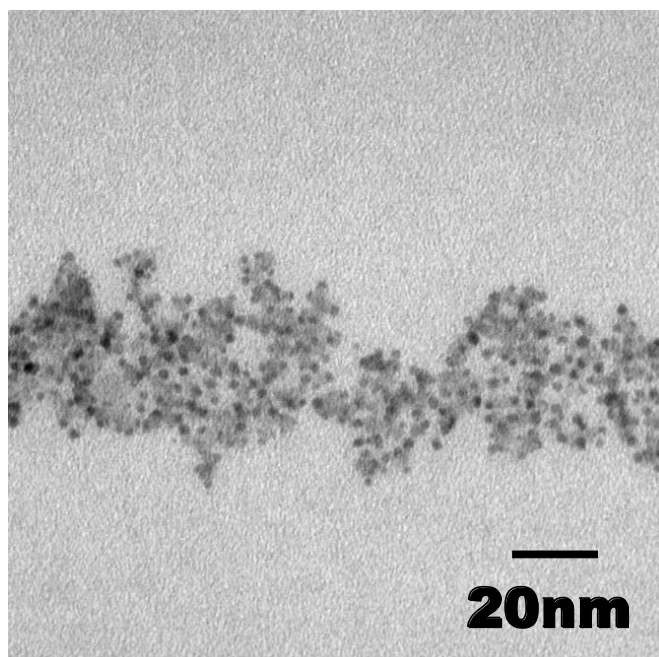


**Figure 6.6:** TEM image of the CuInSSe-based hybrid nanostructures - Au NCs grow onto CuInSSe NPs.

selectively grow onto vertexes of CuInSSe pyramids, which have a high surface energy and might be less efficiently protected by organic ligands. These two reasons [29, 44] facilitate selective growth of metal NCs onto semiconductor NPs.

We studied the structure of this hybrid material with x-ray diffraction. Figure 6.7 shows the diffraction pattern obtained, together with the results of the Rietveld analysis. All the reflections are significantly broadened indicating the nanocrystalline nature of the sample. The presence of some amount of an amorphous material also cannot be excluded. As expected, gold nanocrystals can be found in the hybrid material. Their size was calculated to be 4 nm, using an isotropic shape model. This value is larger than the size obtained from TEM images. The other phase that could be identified from the XRD measurement consists of small nanoparticles (1.5 nm) of elemental selenium. We found some texture effects for the selenium phase, using a harmonic texture model [88]. Interestingly, a comparison of the reconstructed pole figures shows some similarities for the (100) and (011) planes in selenium ( $3.24 \text{ \AA}$  and  $2.74 \text{ \AA}$ , respectively) and (111) and

### 6.3 Synthesis and characterization of CuInSSe/Au hybrid nanostructures

(200) planes in the original CuInSSe particles (3.30 Å and 2.86 Å, respectively). Even

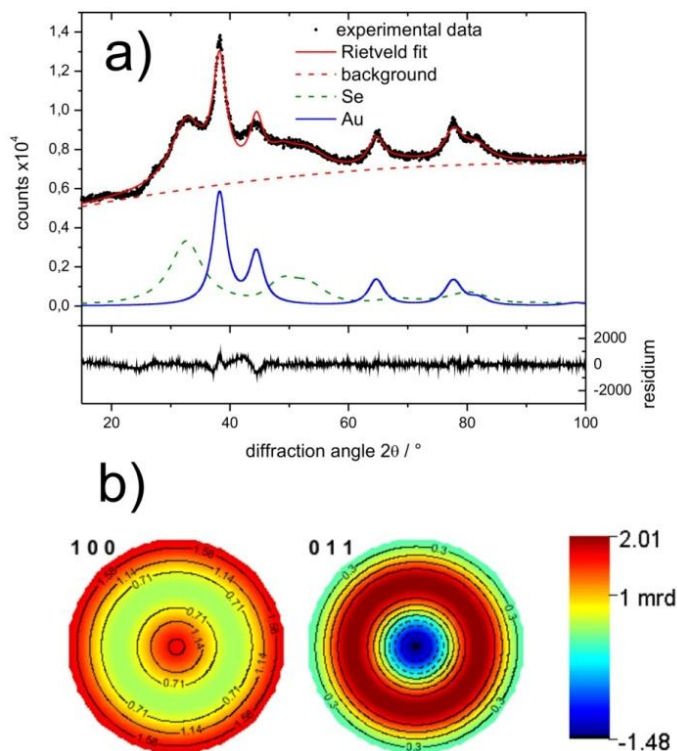


**Figure 6.7: Powder X-ray diffraction patterns of the hybrid nanostructures -** a) The experimental data (dots) is plotted together with a Rietveld fit (red line) and the deconvolution into two phases, selenium (green line) and gold (blue line); b) Reconstructed pole figures resulting from refinement according to the applied texture model. The (100) planes of selenium have a high probability to be oriented parallel to the sample holder.

though, we cannot find a crystalline CuInSSe phase in the diffraction pattern after the reaction with gold, selenium particles seem to have a preferred orientation, which is related to the preferred orientation of the CuInSSe tetrahedra used for this reaction. Thus, the reaction with gold converts some part of the CuInSSe nanoparticles to elemental selenium, this particle probably remains attached to the remaining CuInSSe part. However, we cannot distinguish between CuInSSe and Se in the TEM images, because both materials have similar contrast.

The UV-Vis-absorption spectrum of hybrid nanocrystals is shown in figure 6.8. The plasmon resonance of Au NPs [44] has not been observed, because of the relatively small

## 6. SYNTHESIS AND CHARACTERIZATION OF CIS/AU HYBRID NANOPARTICLES

---

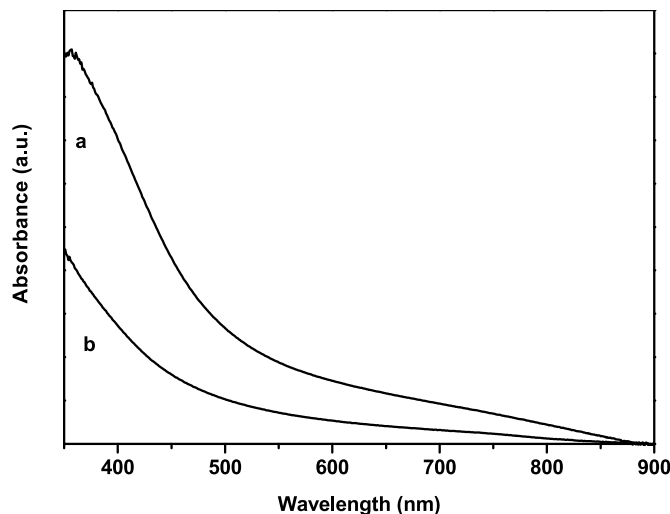


**Figure 6.8:** Comparison of the absorption of the semiconductor and resulting semiconductor-metal nanostructures - a) original CuInSSe NPs; b) hybrid CuInSSe-based nanostructures.

size of metallic nanocrystals [42]. The absorption offset of the hybrid nanostructure is blueshifted compared with the original CuInSSe NPs. One reason for the blue shift can be the reduced size of the semiconductor part of the hybrid material, compared with the original CuInSSe tetrahedra. We can, however, not exclude also changes in the composition of the CuInSSe nanocrystals.

The samples were characterized by EDX analysis (figure 6.9), in order to determine the composition of the nanocrystals after the reaction with gold. Compared with the original CuInSSe NPs, the resulting hybrid nanostructures have a different ratio between Cu, In, S and Se, furthermore, gold could be detected. We found a ratio of 1:1:1:5:14 for Cu:In:S:Se:Au. The element ratio in the semiconductor part can change after the reaction with the gold precursor [148], because the semiconductor material plays the role of the reducing agent for gold ions. This mechanism of the reaction proposed by Y. Khalavka et al. [148] for CdTe/Au nanostructures seems to hold also for our materials.



Gold reduction takes place on the surface of CuInSSe NPs. The change of the elemental ratio In:S:Se from 1:0.65:1.35 in initial CuInSSe NPs to 1:1:5 in the hybrid nanostructures is surprising at first, when taking into account the difference between the values

## 6.4 CuInS<sub>2</sub>/Au hybrid nanostructures: Difference in the synthesis mechanism

---

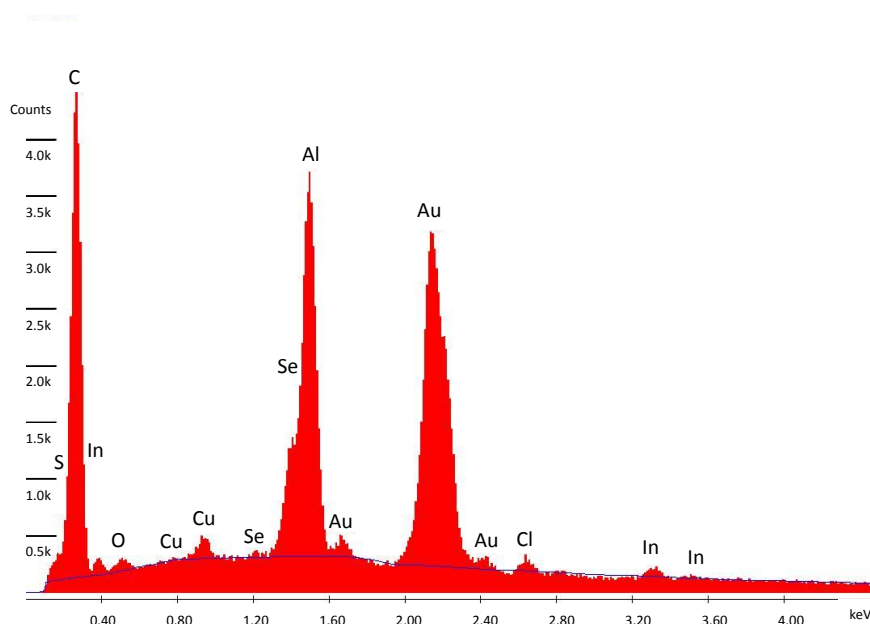


**Figure 6.9: EDX measurement of the CuInSSe/Au NPs** - The ratio Cu:In:S:Se:Au was found to be 1:1:1:5:14.

of the reduction potentials of selenium and sulfur ( $\text{Se}^{2-}$ : -0.92V,  $\text{S}^{2-}$ : -0.48V) [148]. Selenium oxidizes much faster than sulfur and should be used up more easily during the reaction. If selenium goes into solution after this reaction, sulfur rich particles should be obtained. Indeed, the ratio between In and S changes from 1:0.65 in the original sample to 1:1 in the hybrid material. Taking into account the results of the XRD measurements (figure 6.7), showing that elemental Se is present in the samples, also the increase of the Se content can be explained. Selenium remains partly in the sample, while some of the cations go into the solution. These changes of the composition of the sample are accompanied by changes in the crystallinity of the CuInSSe material.

## 6.4 CuInS<sub>2</sub>/Au hybrid nanostructures: Difference in the synthesis mechanism

It has been shown by the Banin group [42] that the heterogeneous growth behavior of Au nanocrystals on nanorods is significantly different for different cadmium chalcogenides, such as CdSe and CdS [42]. The CuInS<sub>2</sub> NPs were applied, synthesized according to

## 6. SYNTHESIS AND CHARACTERIZATION OF CIS/AU HYBRID NANOPARTICLES

---

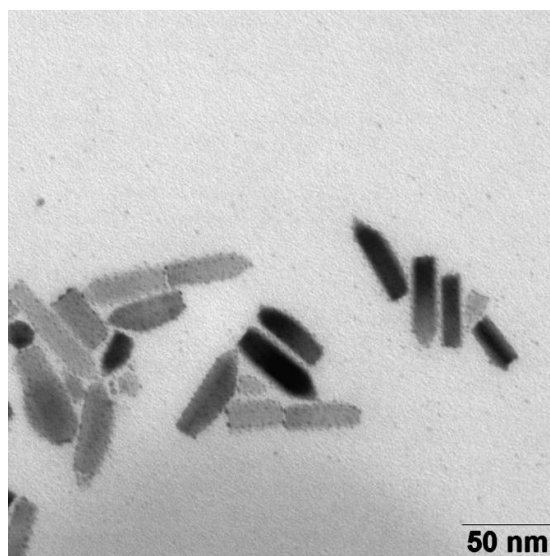


**Figure 6.10:** TEM image of the CuInS<sub>2</sub>/Au NPs - The reduction of Au takes place on the surface of the CuInS<sub>2</sub> NPs.

a method described previously [80], in order to find out, whether selective growth of gold nanocrystals is also possible on other I-III-VI NPs. In this reaction, the growth behavior of gold is different. The reduction of Au takes also place on the surface of the CuInS<sub>2</sub> NPs, but the selective growth was not observed. Although the CuInS<sub>2</sub> NPs chosen for this reaction possess regions of high surface curvature, relatively small gold particles appear at random places on the whole surface of the semiconductor (figure 6.10). According to other studies [42], defects also provide high energy sites for nucleation and growth of Au NCs. Also in this study, the presence of defects on the surface of CuInS<sub>2</sub> NPs is relatively likely, as can be seen from their low emission quantum efficiency (results not shown here). Thus, we conclude that growth of Au NCs on the surface of CuInS<sub>2</sub> NPs preferentially takes place on the surface defects.

The absorption spectra of the original CuInS<sub>2</sub> NPs and the CuInS<sub>2</sub>/Au hybrid nanoparticles are shown in figure 6.11. The absorption offset of hybrid NPs is red-shifted. As has been shown for other materials, the red shift originates from delocalization of the electrons over the whole semiconductor-metal nanohybrid material, and might be also due to the increase of the dielectric constant of the shell around the semiconductor in the presence of metal particles [44, 132]. It was not observed any changes in the shape and in the size of the CuInS<sub>2</sub> NPs, thus, the redshift of the absorption off-



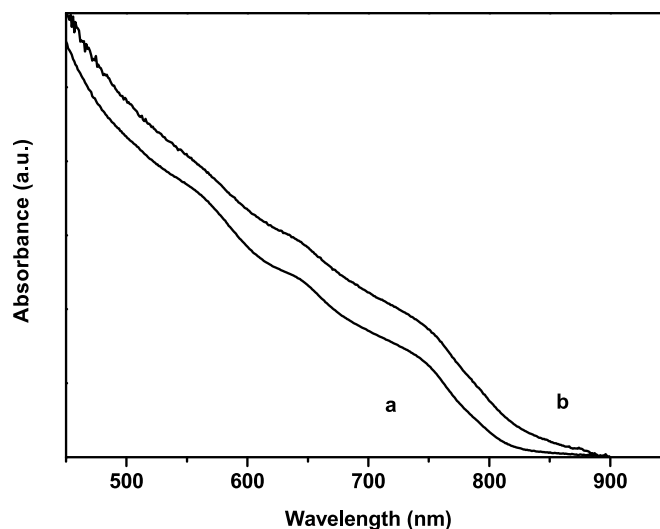


**Figure 6.11:** Comparison of the absorption spectra of the original  $\text{CuInS}_2$  NPs (a) and  $\text{CuInS}_2/\text{Au}$  hybrid nanostructures (b) - The absorption offset of hybrid NPs is red-shifted.

set indicates the formation of metal-semiconductor hybrid nanostructures in solution, and not later, e.g., under the beam in the transmission electron microscope.

## 6.5 Conclusion

In summary,  $\text{CuInSSe}/\text{Se}/\text{Au}$  nanostructures have been produced by the growth of Au NCs onto the previously prepared  $\text{CuInSSe}$  NPs. The mechanism of this reaction is based on a reduction of a gold precursor on the vertexes of  $\text{CuInSSe}$  pyramids (figure 6.12a), according to the results of the TEM and EDX analysis. The reaction leading to the formation of gold nanocrystals has a strong influence onto the structure of the semiconductor part of the hybrid material, because  $\text{CuInSSe}$  plays the role of the reducing agent for gold ions. Thus, heterostructure nanocrystals grow through the reaction of a sacrificial component of the semiconductor part. During this reaction, elemental selenium particles are formed (figure 6.12a), and the size and the crystallinity of the  $\text{CuInSSe}$  part of the hybrid nanostructure are reduced. However, the EDX measurements reveal that the particles still contain copper and indium, and, in spite of their lower crystallinity, absorption of the  $\text{CuInSSe}$  nanoparticles still can be observed. In contrast to these results, experiments with particles which do not contain selenium

## 6. SYNTHESIS AND CHARACTERIZATION OF CIS/AU HYBRID NANOPARTICLES

---

( $\text{CuInS}_2$  NPs), did not show any selectivity of the Au NCs growth (figure 6.12b), but also no changes in the size and shape of the semiconductor part of the hybrid structure were observed. These results show that semiconductor-metal hybrid nanostructures can

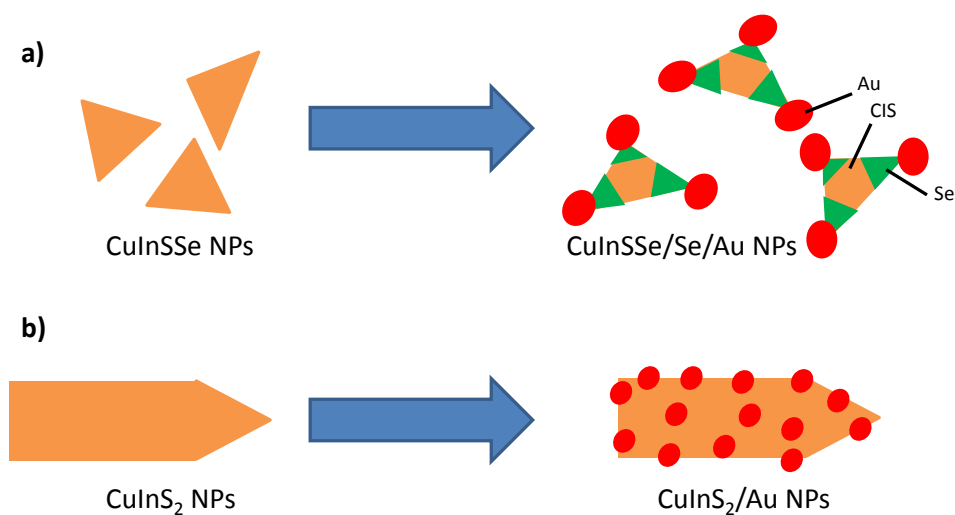


**Figure 6.12: Comparison of the mechanism of the formation of hybrid CIS/Au NPs** - a)  $\text{CuInSSe}$  NPs served as semiconductor part, b)  $\text{CuInS}_2$  NPs as semiconductor part.

be obtained from I-III-VI semiconductor nanocrystals, and gold particles preferentially grow on surface sites having high energy (defects, or places with high curvature). Comparison between the reactions of  $\text{CuInSSe}$  and  $\text{CuInS}_2$  NPs shows that the presence of selenium facilitates the growth of Au NCs and enhances the selectivity of the reaction.

## Chapter 7

# Summary

This thesis focuses on the colloidal synthesis of semiconductor nanoparticles and semiconductor-metal nanostructures as well as their characterization. The development and qualitative investigation of colloidal synthesis were carried out on lead chalcogenide and indium oxide nanoparticles as well as on hybrid CIS/Au nanostructures. Transmission electron microscopy, UV/Vis and photoluminescence spectroscopy, x-ray diffraction, energy dispersive x-ray spectroscopy and nuclear magnetic resonance spectroscopy were used in order to study the synthetic mechanism and to characterize properties of prepared nanoparticles.

Lead chalcogenide nanoparticles (PbE NPs) are a promising material for the application in photovoltaics. One of its advantages is the absorption in the near infrared region allowing the better use of solar light. The laboratory solar cells, however, show only a low power conversion efficiency [23, 84]. That pushes forward the research of synthesis and surface modification of lead chalcogenide nanoparticles. The PbS, PbSe and PbTe nanoparticles with different shapes and sizes have been synthesized via a standard hot-injection method. However, at high temperature metallic Pb<sup>0</sup> particles occurred. These might play an important role at the nucleation of nanoparticles. Furthermore, oleic acid used as stabilizer was considered to be oxidized under such conditions. Therefore resulting nanoparticles were stabilized with its oxidation product. That makes the ligand exchange easier, which is a necessary step for further physical application. The as-synthesized PbSe nanoparticles were used for the preparation of an active layer of hybrid solar cells which was studied by electron spin resonance and photoinduced absorption spectroscopy [8]. The results show the light-induced generation

## 7. SUMMARY

---

of charge carriers. There is further interest in the research of the nanoparticle surface, because of its importance in the application in the active layer of solar cells in future devices.

Indium oxide ( $\text{In}_2\text{O}_3$ ) is the next important material not only for photovoltaic but also in the preparation of gas sensors, monitors, and touchscreens. The devices show often a better efficiency by using  $\text{In}_2\text{O}_3$  as a nanomaterial. Although wet chemical synthesis is advantageous, there are just a few colloidal syntheses of  $\text{In}_2\text{O}_3$  nanoparticles. In this dissertation, the research was focused on developing an easy and fast colloidal synthesis for  $\text{In}_2\text{O}_3$  nanoparticles and their shape control. The synthesis is based on a non-injection method. Indium acetate was used as the indium precursor, while oleylamine acted as stabilizer and solvent simultaneously. As a result flower-shaped  $\text{In}_2\text{O}_3$  nanoparticles occurred. Apart from organic stabilizers usually used for nanoparticle shape control, copper ions were applied. With addition of different copper salts the shape of nanoparticles was changed to quasi spherical or prolonged. The mechanism of both shape control procedures was investigated.

The research on the nanomaterials and their synthesis was continued with hybrid semiconductor-metal nanoparticles. These materials are different to the single semiconductor nanoparticles with respect to their synthesis and properties. The ternary and quaternary semiconductor CIS nanoparticles were taken as a starting point for the synthesis of CIS/Au nanostructures in order to avoid the toxicity of Pb or Cd compounds, which is a major disadvantage for application of this materials. For this sake, the pyramidal CuInSSe nanoparticles were synthesized by a hot-injection method. The gold nanocrystals have been grown selectively onto the surface of CuInSSe nanoparticles. Additionally, the CuInS<sub>2</sub> nanoparticles were also applied for hybrid nanostructure synthesis as a semiconductor part instead of CuInSSe nanoparticles. The difference of these two synthesis mechanisms was investigated.

In conclusion, this dissertation demonstrates a study of several application relevant material systems including semiconductor and semiconductor-metal nanoparticles. During this research the knowledge of the different synthesis mechanisms have been gained and might be helpful for the design of nanoparticles having a high application potential in physics, chemistry, or biology. Thus, the colloidal nanoparticle preparation, being not completely explored in all variations, turned to be a promising strategy for device improvement.

## Appendix A

### H-phrases and P-phrases

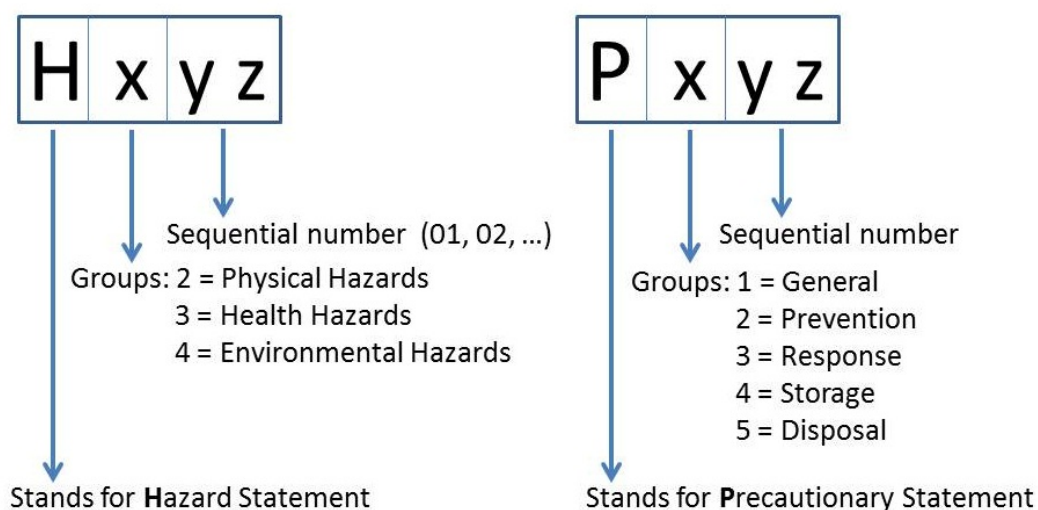


Figure A.1: Structure of the H- and P-Statements - according to the CLP-Regulation

#### A.1 Chemicals

**1-Dodecanethiol** Signal word: Danger

Hazard statements: H315-H318-H334-H335

Precautionary statements: P261-P280-P305 + P351 + P338-P342 + P311

**1-Octadecene** Signal word: Danger

## A. H-PHRASES AND P-PHRASES

---

Hazard statements: H304

Precautionary statements: P301 + P310-P331

**Chloroform-d** Signal word: Warning

Hazard statements: H302-H315-H351-H373

Precautionary statements: P281

**Copper (I) acetate** Signal word: Warning

Hazard statements: H315-H319-H335

Precautionary statements: P261-P305 + P351 + P338

**Copper (II) acetate** Signal word: Warning

Hazard statements: H302-H315-H319-H335-H400

Precautionary statements: P261-P273-P305 + P351 + P338

**Copper (II) acetylacetonate** Signal word: Warning

Hazard statements: H315-H319-H335

Precautionary statements: P261-P305 + P351 + P338

**Copper (I) chloride** Signal word: Warning

Hazard statements: H302-H410

Precautionary statements: P273-P501

**Didodecyldimethylammonium bromide** Signal word: Warning

Hazard statements: H315-H319-H335

Precautionary statements: P261-P305 + P351 + P338

**Dodecylamine** Signal word: Danger

Hazard statements: H302-H314-H410

Precautionary statements: P273-P280-P305 + P351 + P338-P310-P501

**Gold (III) chloride** Signal word: Warning

Hazard statements: H315-H319-H335

Precautionary statements: P261-P305 + P351 + P338

**Hexylamine** Signal word: Danger

Hazard statements: H226-H301-H311-H314

Precautionary statements: P280-P301 + P310-P305 + P351 + P338-P310

**Indium (III) acetate** Signal word: Warning

Hazard statements: H315-H319-H335

Precautionary statements: P261-P305 + P351 + P338

**Indium (III) chloride** Signal word: Danger

Hazard statements: H302-H314

Precautionary statements: P280-P305 + P351 + P338-P310

**Lead (II) oxide** Signal word: Danger

Hazard statements: H302-H332-H360Df-H373-H410

Precautionary statements: P201-P273-P308 + P313-P501

**Octylamine** Signal word: Danger

Hazard statements: H226-H302-H312-H314-H332-H400

Precautionary statements: P273-P280-P305 + P351 + P338-P310

**Oleic acid** Signal word: Warning

Hazard statements: H315

**Oleylamine** Signal word: Danger

Hazard statements: H314-H400

Precautionary statements: P273-P280-P305 + P351 + P338-P310

**Selenium** Signal word: Danger

Hazard statements: H301-H331-H373-H413

Precautionary statements: P261-P301 + P310-P311

**Sulfur** Signal word: Warning

Hazard statements: H228

Precautionary statements: P210

**Tellurium** Signal word: Danger

Hazard statements: H301

Precautionary statements: P301 + P310

**Tri-n-octylphosphine** Signal word: Danger

Hazard statements: H314

Precautionary statements: P280-P305 + P351 + P338-P310

## A. H-PHRASES AND P-PHRASES

---

**Tributylphosphine** Signal word: Danger

Hazard statements: H226-H250-H302-H312-H314

Precautionary statements: P222-P231-P280-P305 + P351 + P338-P310-P422

**Tridodecylamine** Signal word: Warning

Hazard statements: H315-H319-H335

Precautionary statements: P261-P305 + P351 + P338

**Trioctylphosphine oxide** Signal word: Danger

Hazard statements: H315-H318

Precautionary statements: P280-P305 + P351 + P338

### A.2 H-Statements

#### H200-Series: Physical hazards

**H200** Unstable explosive

**H201** Explosive; mass explosion hazard

**H202** Explosive; severe projection hazard

**H203** Explosive; fire, blast or projection hazard

**H204** Fire or projection hazard

**H205** May mass explode in fire

**H220** Extremely flammable gas

**H221** Flammable gas

**H222** Extremely flammable material

**H223** Flammable material

**H224** Extremely flammable liquid and vapour

**H225** Highly flammable liquid and vapour

**H226** Flammable liquid and vapour



**H228** Flammable solid

**H240** Heating may cause an explosion

**H241** Heating may cause a fire or explosion

**H242** Heating may cause a fire

**H250** Catches fire spontaneously if exposed to air

**H251** Self-heating; may catch fire

**H252** Self-heating in large quantities; may catch fire

**H260** In contact with water releases flammable gases which may ignite spontaneously

**H261** In contact with water releases flammable gas

**H270** May cause or intensify fire; oxidizer

**H271** May cause fire or explosion; strong oxidizer

**H272** May intensify fire; oxidizer

**H280** Contains gas under pressure; may explode if heated

**H281** Contains refrigerated gas; may cause cryogenic burns or injury

**H290** May be corrosive to metals

### **H300-Series: Health hazards**

**H300** Fatal if swallowed

**H301** Toxic if swallowed

**H302** Harmful if swallowed

**H304** May be fatal if swallowed and enters airways

**H310** Fatal in contact with skin

**H311** Toxic in contact with skin

## A. H-PHRASES AND P-PHRASES

---

**H312** Harmful in contact with skin

**H314** Causes severe skin burns and eye damage

**H315** Causes skin irritation

**H317** May cause an allergic skin reaction

**H318** Causes serious eye damage

**H319** Causes serious eye irritation

**H330** Fatal if inhaled

**H331** Toxic if inhaled

**H332** Harmful if inhaled

**H334** May cause allergy or asthma symptoms or breathing difficulties if inhaled

**H335** May cause respiratory irritation

**H336** May cause drowsiness or dizziness

**H340** May cause genetic defects (state route of exposure if it is conclusively proven that no other routes of exposure cause the hazard)

**H341** Suspected of causing genetic defects (state route of exposure if it is conclusively proven that no other routes of exposure cause the hazard)

**H350** May cause cancer (state route of exposure if it is conclusively proven that no other routes of exposure cause the hazard)

**H350i** May cause cancer by inhalation

**H351** Suspected of causing cancer (state route of exposure if it is conclusively proven that no other routes of exposure cause the hazard)

**H360** May damage fertility or the unborn child (state specific effect if known)(state route of exposure if it is conclusively proven that no other routes of exposure cause the hazard)

**H360F** May damage fertility

**H360D** May damage the unborn child

**H360FD** May damage fertility; may damage the unborn child

**H360Fd** May damage fertility; suspected of damaging the unborn child

**H360Df** May damage the unborn child; suspected of damaging fertility

**H361** Suspected of damaging fertility or the unborn child (state route of exposure if it is conclusively proven that no other routes of exposure cause the hazard)

**H361f** Suspected of damaging fertility

**H361d** Suspected of damaging the unborn child

**H361fd** Suspected of damaging fertility; suspected of damaging the unborn child

**H362** May cause harm to breast-fed children

**H370** Causes damage to organs (or state all organs affected, if known) (state route of exposure if it is conclusively proven that no other routes of exposure cause the hazard)

**H371** May cause damage to organs (or state all organs affected, if known) (state route of exposure if it is conclusively proven that no other routes of exposure cause the hazard)

**H372** Causes damage to organs through prolonged or repeated exposure (state all organs affected, if known) through prolonged or repeated exposure (state route of exposure if it is conclusively proven that no other routes of exposure cause the hazard)

**H373** May cause damage to organs through prolonged or repeated exposure (state all organs affected, if known) through prolonged or repeated exposure (state route of exposure if it is conclusively proven that no other routes of exposure cause the hazard)

## A. H-PHRASES AND P-PHRASES

---

### **H400-Series: Environmental hazards**

**H400** Very toxic to aquatic life

**H410** Very toxic to aquatic life with long lasting effects

**H411** Toxic to aquatic life with long lasting effects

**H412** Harmful to aquatic life with long lasting effects

**H413** May cause long lasting harmful effects to aquatic life

### **A.3 P-Statements**

#### **P100-Series: General**

**P101** If medical advice is needed, have product container or label at hand

**P102** Keep out of reach of children

**P103** Read label before use

#### **P200-Series: Prevention**

**P201** Obtain special instructions before use

**P202** Do not handle until all safety precautions have been read and understood

**P210** Keep away from heat/sparks/open flames/hot surfaces; no smoking

**P211** Do not spray on an open flame or other ignition source

**P220** Keep/Store away from clothing//combustible materials

**P221** Take any precaution to avoid mixing with combustibles

**P222** Do not allow contact with air

**P223** Keep away from any possible contact with water, because of violent reaction and possible flash fire

**P230** Keep wetted with

- P231** Handle under inert gas
- P232** Protect from moisture
- P233** Keep container tightly closed
- P234** Keep only in original container
- P235** Keep cool
- P240** Ground/bond container and receiving equipment
- P241** Use explosion-proof electrical/ventilating/lighting//equipment
- P242** Use only non-sparking tools
- P243** Take precautionary measures against static discharge
- P244** Keep reduction valves free from grease and oil
- P250** Do not subject to grinding/shock//friction
- P251** Pressurized container: Do not pierce or burn, even after use
- P260** Do not breathe dust/fume/gas/mist/vapours/spray
- P261** Avoid breathing dust/fume/gas/mist/vapours/spray
- P262** Do not get in eyes, on skin, or on clothing
- P263** Avoid contact during pregnancy/while nursing
- P264** Wash thoroughly after handling
- P270** Do not eat, drink or smoke when using this product
- P271** Use only outdoors or in a well-ventilated area
- P272** Contaminated work clothing should not be allowed out of the workplace
- P273** Avoid release to the environment
- P280** Wear protective gloves/protective clothing/eye protection/face protection

## **A. H-PHRASES AND P-PHRASES**

---

**P281** Use personal protective equipment as required

**P282** Wear cold insulating gloves/face shield/eye protection

**P283** Wear fire/flame resistant/retardant clothing

**P284** Wear respiratory protection

**P285** In case of inadequate ventilation wear respiratory protection

**P231+P232** Handle under inert gas; protect from moisture

**P235+P410** Keep cool; protect from sunlight

### **P300-Series: Prevention**

**P301** IF SWALLOWED:

**P302** IF ON SKIN:

**P303** IF ON SKIN (or hair):

**P304** IF INHALED:

**P305** IF IN EYES:

**P306** IF ON CLOTHING:

**P307** IF exposed:

**P308** IF exposed or concerned:

**P309** IF exposed or if you feel unwell:

**P310** Immediately call a POISON CENTER or doctor/physician

**P311** Call a POISON CENTER or doctor/physician

**P312** Call a POISON CENTER or doctor/physician if you feel unwell

**P313** Get medical advice/attention

**P314** Get medical advice/attention if you feel unwell

- P315** Get immediate medical advice/attention
- P320** Specific treatment is urgent (see on this label)
- P321** Specific treatment (see on this label)
- P322** Specific measures (see on this label)
- P330** Rinse mouth
- P331** Do NOT induce vomiting
- P332** If skin irritation occurs:
- P333** If skin irritation or rash occurs:
- P334** Immerse in cool water/wrap in wet bandages
- P335** Brush off loose particles from skin
- P336** Thaw frosted parts with lukewarm water; Do not rub affected area
- P337** If eye irritation persists:
- P338** Remove contact lenses, if present and easy to do; continue rinsing
- P340** Remove victim to fresh air and keep at rest in a position comfortable for breathing
- P341** If breathing is difficult, remove victim to fresh air and keep at rest in a position comfortable for breathing
- P342** If experiencing respiratory symptoms:
- P350** Gently wash with plenty of soap and water
- P351** Rinse cautiously with water for several minutes
- P352** Wash with plenty of soap and water
- P353** Rinse skin with water/shower
- P360** Rinse immediately contaminated clothing and skin with plenty of water before removing clothes

## A. H-PHRASES AND P-PHRASES

---

- P361** Remove/Take off immediately all contaminated clothing
- P362** Take off contaminated clothing and wash before reuse
- P363** Wash contaminated clothing before reuse
- P370** In case of fire:
- P371** In case of major fire and large quantities:
- P372** Explosion risk in case of fire
- P373** DO NOT fight fire when fire reaches explosives
- P374** Fight fire with normal precautions from a reasonable distance
- P375** Fight fire remotely due to the risk of explosion
- P376** Stop leak if safe to do so
- P377** Leaking gas fire: Do not extinguish, unless leak can be stopped safely
- P378** Use for extinction
- P380** Evacuate area
- P381** Eliminate all ignition sources if safe to do so
- P390** Absorb spillage to prevent material damage
- P391** Collect spillage
- P301+P310** IF SWALLOWED: Immediately call a POISON CENTER or doctor/physician
- P301+P312** IF SWALLOWED: Call a POISON CENTER or doctor/physician if you feel unwell
- P301+P330+P331** IF SWALLOWED: rinse mouth; DO NOT induce vomiting
- P302+P334** IF ON SKIN: Immerse in cool water/wrap in wet bandages
- P302+P350** IF ON SKIN: Gently wash with plenty of soap and water
- P302+P352** IF ON SKIN: Wash with plenty of soap and water



**P303+P361+P353** IF ON SKIN (or hair): Remove/Take off immediately all contaminated clothing; rinse skin with water/shower

**P304+P340** IF INHALED: Remove victim to fresh air and keep at rest in a position comfortable for breathing

**P304+P341** IF INHALED: If breathing is difficult, remove victim to fresh air and keep at rest in a position comfortable for breathing

**P305+P351+P338** IF IN EYES: Rinse cautiously with water for several minutes; remove contact lenses, if present and easy to do; continue rinsing

**P306+P360** IF ON CLOTHING: rinse immediately contaminated clothing and skin with plenty of water before removing clothes

**P307+P311** IF exposed: Call a POISON CENTER or doctor/physician

**P308+P313** IF exposed or concerned: Get medical advice/attention

**P309+P311** IF exposed or if you feel unwell: Call a POISON CENTER or doctor/physician

**P332+P313** If skin irritation occurs: Get medical advice/attention

**P333+P313** If skin irritation or rash occurs: Get medical advice/attention

**P335+P334** Brush off loose particles from skin; immerse in cool water/wrap in wet bandages

**P337+P313** If eye irritation persists: Get medical advice/attention

**P342+P311** If experiencing respiratory symptoms: Call a POISON CENTER or doctor/physician

**P370+P376** In case of fire: Stop leak if safe to do so

**P370+P378** In case of fire: Use for extinction

**P370+P380** In case of fire: Evacuate area

**P370+P380+P375** In case of fire: Evacuate area; fight fire remotely due to the risk of explosion

## A. H-PHRASES AND P-PHRASES

---

**P371+P380+P375** In case of major fire and large quantities: Evacuate area; fight fire remotely due to the risk of explosion

### **P400-Series: Storage**

**P401** Store

**P402** Store in a dry place

**P403** Store in a well-ventilated place

**P404** Store in a closed container

**P405** Store locked up

**P406** Store in corrosive resistant/ container with a resistant inner liner

**P407** Maintain air gap between stacks/pallets

**P410** Protect from sunlight

**P411** Store at temperatures not exceeding °C/ °F

**P412** Do not expose to temperatures exceeding 50°C/122°F

**P413** Store bulk masses greater than kg/ lbs at temperatures not exceeding °C/ °F

**P420** Store away from other materials

**P422** Store contents under

**P402+P404** Store in a dry place; store in a closed container

**P403+P233** Store in a well-ventilated place; keep container tightly closed

**P403+P235** Store in a well-ventilated place; keep cool

**P410+P403** Protect from sunlight; store in a well-ventilated place

**P410+P412** Protect from sunlight; do not expose to temperatures exceeding 50°C/122°F

**P411+P235** Store at temperatures not exceeding °C/ °F; keep cool

**P500-Series: Disposal**

**P501** Dispose of contents/container to

## A. H-PHRASES AND P-PHRASES

---

# Bibliography

- [1] Goesmann, H. and Claus, F. *Angewandte Chemie* **122**, 1402–1437 (2010).
- [2] Patzke, G. R., Zhou, Y., Kontic, R., and Conrad, F. *Angewandte Chemie* **123**, 852–889 (2011).
- [3] Jun, Y.-w., Choi, J.-s., and Cheon, J. *Angewandte Chemie* **118**, 3492–3517 (2006).
- [4] Niu, W., Li, Z.-Y., Shi, L., Liu, X., Li, H., Han, S., Chen, J., and Xu, G. *Crystal Growth & Design* **8**, 4440–4444 (2008).
- [5] Murray, C., Norris, D., and Bawendi, M. *Journal of the American Chemical Society* **115**, 8706–8715 (1993).
- [6] Peng, X., Manna, L., Yang, W., Wickham, J., Scher, E., Kadavanich, A., and Alivisatos, A. *Nature* **404**, 59–61 (2000).
- [7] Murphy, C., San, T., Gole, A., Orendorff, C., Gao, J., Gou, L., Hunyadi, S., and Li, T. *Journal of Physical Chemistry B* **109**, 13857–13870 (2005).
- [8] Witt, F. *Charakterisierung limitierender Faktoren in hybriden Donor-Akzeptor-Solarzellen*. PhD thesis, Universität Oldenburg, (2011).
- [9] Park, J., Joo, J., Kwon, S. G., Jang, Y., and Hyeon, T. *Angewandte Chemie* **119**, 4714–4745 (2007).
- [10] Costi, R., Saunders, A. E., and Banin, U. *Angewandte Chemie* **122**, 4996–5016 (2010).
- [11] Poole Jr., C. P. and Owens, F. J. *Introduction to nanotechnology*. Wiley, Hoboken (2003).
- [12] Brus, L. *Journal of Chemical Physics* **80**, 4403–4409 (1984).
- [13] Borchert, H. *Energy & Environmental Science* **3**, 1682–1694 (2010).
- [14] Li, L., Hu, J., Yang, W., and Alivisatos, A. *Nano Letters* **1**, 349–351 (2001).
- [15] Hu, J., Li, L., Yang, W., Manna, L., Wang, L., and Alivisatos, A. *Science* **292**, 2060–2063 (2001).
- [16] Tessler, N., Medvedev, V., Kazes, M., Kan, S., and Banin, U. *Science* **295**, 1506–1508 (2002).
- [17] Bruchez, M., Moronne, M., Gin, P., Weiss, S., and Alivisatos, A. *Science* **281**, 2013–2016 (1998).
- [18] Achermann, M., Petruska, M., Kos, S., Smith, D., Koleske, D., and Klimov, V. *Nature* **429**, 642–646 (2004).
- [19] Huynh, W., Dittmer, J., and Alivisatos, A. *Science* **295**, 2425–2427 (2002).
- [20] Gao, X., Cui, Y., Levenson, R., Chung, L., and Nie, S. *Nature Biotechnology* **22**, 969–976 (2004).
- [21] Ma, Q. and Su, X. *Analyst* **135**, 1867–1877 (2010).
- [22] Rogach, A. L., Eychmueller, A., Hickey, S. G., and Kershaw, S. V. *Small* **3**, 536–557 (2007).
- [23] Jiang, X., Schaller, R. D., Lee, S. B., Pietryga, J. M., Klimov, V. I., and Zakhidov, A. A. *Journal of Materials Research* **22**, 2204–2210 (2007).
- [24] Guo, Q., Kim, S. J., Kar, M., Shafarman, W. N., Birkmire, R. W., Stach, E. A., Agrawal, R., and Hillhouse, H. W. *Nano Letters* **8**, 2982–2987 (2008).
- [25] Talapin, D. V. and Murray, C. B. *Science* **310**, 86–89 (2005).
- [26] Urban, J., Talapin, D., Shevchenko, E., and Murray, C. *Journal of the American Chemical Society* **128**, 3248–3255 (2006).
- [27] Ziqubu, N., Ramasamy, K., Rajasekhar, P. V. S. R., Revaprasadu, N., and O'Brien, P. *Chemistry of Materials* **22**, 3817–3819 (2010).

## BIBLIOGRAPHY

---

- [28] Moreels, I., Fritzingler, B., Martins, J. C., and Hens, Z. *Journal of the American Chemical Society* **130**, 15081–15086 (2008).
- [29] Yang, J., Elim, H. I., Zhang, Q., Lee, J. Y., and Ji, W. *Journal of the American Chemical Society* **128**, 11921–11926 (2006).
- [30] Li, L., Daou, T. J., Texier, I., Chi, T. T. K., Liem, N. Q., and Reiss, P. *Chemistry of Materials* **21**, 2422–2429 (2009).
- [31] Gao, J., Gu, H., and Xu, B. *Accounts of Chemical Research* **42**, 1097–1107.
- [32] Cheek, G., Genis, A., Dubow, J., and Paivernerker, V. *Applied Physics Letters* **35**, 495–497 (1979).
- [33] Lu, X., Yu, Q., Wang, K., Shi, L., Liu, X., Qiu, A., Wang, L., and Cui, D. *Crystal Research and Technology* **45**, 557–561 (2010).
- [34] Qurashi, A., El-Maghraby, E. M., Yamazaki, T., Shen, Y., and Kikuta, T. *Journal of Alloys Compounds* **481**, L35–L39 (2009).
- [35] Farvid, S. S., Dave, N., Wang, T., and Radovanovic, P. V. *Journal of Physical Chemistry C* **113**, 15928–15933 (2009).
- [36] Jean, S.-T. and Her, Y.-C. *Crystal Growth & Design* **10**, 2104–2110 (2010).
- [37] Caruntu, D., Yao, K., Zhang, Z., Austin, T., Zhou, W., and O'Connor, C. J. *Journal of Physical Chemistry C* **114**, 4875–4886 (2010).
- [38] Kar, S. and Chaudhuri, S. *Chemical Physics Letters* **422**, 424–428 (2006).
- [39] Philip, J., Punnoose, A., Kim, B., Reddy, K., Layne, S., Holmes, J., Satpati, B., Leclair, P., Santos, T., and Moodera, J. *Nature Materials* **5**, 298–304 (2006).
- [40] Gurlo, A. *Angewandte Chemie* **122**, 5742–5744 (2010).
- [41] Kamat, P. V. *Journal of Physical Chemistry C* **112**, 18737–18753 (2008).
- [42] Saunders, A. E., Popov, I., and Banin, U. *Journal of Physical Chemistry B* **110**, 25421–25429 (2006).
- [43] Shi, W., Zeng, H., Sahoo, Y., Ohulchanskyy, T., Ding, Y., Wang, Z., Swihart, M., and Prasad, P. *Nano Letters* **6**, 875–881 (2006).
- [44] Mokari, T., Rothenberg, E., Popov, I., Costi, R., and Banin, U. *Science* **304**, 1787–1790 (2004).
- [45] Yu, W., Wang, Y., and Peng, X. *Chemistry of Materials* **15**, 4300–4308 (2003).
- [46] Lokteva, I., Radychev, N., Witt, F., Borchert, H., Parisi, J., and Kolny-Olesiak, J. *Journal of Physical Chemistry C* **114**, 12784 (2010).
- [47] Ford, G. and LaMer, V. *Journal of the American Chemical Society* **72**, 1959–1964 (1950).
- [48] Peng, Z. and Peng, X. *Journal of the American Chemical Society* **124**, 3343–3353 (2002).
- [49] Peng, X., Wickham, J., and Alivisatos, A. *Journal of the American Chemical Society* **120**, 5343–5344 (1998).
- [50] Jackson, K. *Kinetic Processes*. Wiley-VCH, Weinheim (2004).
- [51] Alivisatos, A. *Journal of Physical Chemistry* **100**, 13226–13239 (1996).
- [52] Gole, A. and Murphy, C. *Chemistry of Materials* **16**, 3633–3640 (2004).
- [53] Talapin, D., Rogach, A., Kornowski, A., Haase, M., and Weller, H. *Nano Letters* **1**, 207–211 (2001).
- [54] Park, J., An, K., Hwang, Y., Park, J., Noh, H., Kim, J., Park, J., Hwang, N., and Hyeon, T. *Nature Materials* **3**, 891–895 (2004).
- [55] Cozzoli, P. D., Pellegrino, T., and Liberato, M. *Chemical Society Reviews* **35**, 1195–1208 (2006).
- [56] Seo, W., Jo, H., Lee, K., and Park, J. *Advanced Materials* **15**, 795–797 (2003).
- [57] van Embden, J., Sader, J. E., Davidson, M., and Mulvaney, P. *Journal of Physical Chemistry C* **113**, 16342–16355 (2009).
- [58] Reiss, H. *Journal of Chemical Physics* **19**, 482–487 (1951).

## BIBLIOGRAPHY

- [59] De Smet, Y., Deriemaeker, L., and Finsy, R. *Langmuir* **13**, 6884–6888 (1997).
- [60] Talapin, D., Rogach, A., Haase, M., and Weller, H. *Journal of Physical Chemistry B* **105**, 12278–12285 (2001).
- [61] Jun, Y., Jung, Y., and Cheon, J. *Journal of the American Chemical Society* **124**, 615–619 (2002).
- [62] Kim, Y., Jun, Y., Jun, B., Lee, S., and Cheon, J. *Journal of the American Chemical Society* **124**, 13656–13657 (2002).
- [63] Hull, K., Grebinski, J., Kosel, T., and Kuno, M. *Chemistry of Materials* **17**, 4416–4425 (2005).
- [64] Jun, Y., Lee, S., Kang, N., and Cheon, J. *Journal of the American Chemical Society* **123**, 5150–5151 (2001).
- [65] Zhang, H., Huang, F., Gilbert, B., and Banfield, J. *Journal of Physical Chemistry B* **107**, 13051–13060 (2003).
- [66] Joo, J., Na, H., Yu, T., Yu, J., Kim, Y., Wu, F., Zhang, J., and Hyeon, T. *Journal of the American Chemical Society* **125**, 11100–11105 (2003).
- [67] Cozzoli, P., Manna, L., Curri, M., Kudera, S., Giannini, C., Striccoli, M., and Agostiano, A. *Chemistry of Materials* **17**, 1296–1306 (2005).
- [68] Murray, C., Sun, S., Gaschler, W., Doyle, H., Betley, T., and Kagan, C. *IBM Journal of Research and Development* **45**, 47–56 (2001).
- [69] Zhong, X., Feng, Y., Knoll, W., and Han, M. *Journal of the American Chemical Society* **125**, 13559–13563 (2003).
- [70] Ghezelbash, A. and Korgel, B. *Langmuir* **21**, 9451–9456 (2005).
- [71] Manna, L., Scher, E., and Alivisatos, A. *Journal of the American Chemical Society* **122**, 12700–12706 (2000).
- [72] Lee, S., Jun, Y., Cho, S., and Cheon, J. *Journal of the American Chemical Society* **124**, 11244–11245 (2002).
- [73] Peng, Z. and Peng, X. *Journal of the American Chemical Society* **123**, 1389–1395 (2001).
- [74] Penn, R. and Banfield, J. *Geochimica et Cosmochimica Acta* **63**, 1549–1557 (1999).
- [75] Cho, K., Talapin, D., Gaschler, W., and Murray, C. *Journal of the American Chemical Society* **127**, 7140–7147 (2005).
- [76] Carbone, L. and Cozzoli, P. D. *Nano Today* **5**, 449–493 (2010).
- [77] Hornyak, G. L., Tibbals, H. F., Dutta, J., and Moore, J. J. *Introduction to nanoscience and nanotechnology*. CRC Press, Boca Raton (2009).
- [78] Williams, D. B. and Barry, C. C. *Transmission electron microscopy: a textbook for material science*. Springer, New York (1996).
- [79] Borchert, H., Shevchenko, E., Robert, A., Mekis, I., Kornowski, A., Grubel, G., and Weller, H. *Langmuir* **21**, 1931–1936 (2005).
- [80] Kruszynska, M., Borchert, H., Parisi, J., and Kolny-Olesiak, J. *Journal of the American Chemical Society* **132**, 15976–15986 (2010).
- [81] Hesse, M., Meier, H., and Zeeh, B. *Spektroskopische Methoden in der organischen Chemie*. Thieme, Stuttgart (2005).
- [82] Liu, Q., Lu, W., Ma, A., Tang, J., Lin, J., and Fang, J. *Journal of the American Chemical Society* **127**, 5276–5277 (2005).
- [83] Kolny-Olesiak, J., Kloper, V., Osovsky, R., Sashchiuk, A., and Lifshitz, E. *Surface Science* **601**, 2667–2670 (2007).
- [84] Noone, K. M., Anderson, N. C., Horwitz, N. E., Munro, A. M., Kulkarni, A. P., and Ginger, D. S. *ACS Nano* **3**, 1345–1352 (2009).
- [85] Zhong, H., Li, Y., Ye, M., Zhu, Z., Zhou, Y., Yang, C., and Li, Y. *Nanotechnology* **18**, 1–6 (2007).
- [86] Lutterotti, L., Chateigner, D., Ferrari, S., and Ricote, J. *Thin Solid Films* **450**, 34–41 (2004).
- [87] Popa, N. *Journal of Applied Crystallography* **31**, 176–180 (1998).

## BIBLIOGRAPHY

---

- [88] Popa, N. *Journal of Applied Crystallography* **25**, 611–616 (1992).
- [89] Joo, J., Pietryga, J. M., McGuire, J. A., Jeon, S.-H., Williams, D. J., Wang, H.-L., and Klimov, V. I. *Journal of the American Chemical Society* **131**, 10620–10628 (2009).
- [90] Murphy, J., Beard, M., Norman, A., Ahrenkiel, S., Johnson, J., Yu, P., Micic, O., Ellingson, R., and Nozik, A. *Journal of the American Chemical Society* **128**, 3241–3247 (2006).
- [91] Kovalenko, M. V., Talapin, D. V., Loi, M. A., Cordella, F., Hesser, G., Bodnarchuk, M. I., and Heiss, W. *Angewandte Chemie-International Edition* **47**, 3029–3033 (2008).
- [92] Baek, I. C., Seok, S. I., and Chung, Y.-C. *Bulletin of the Korean Chemical Society* **29**, 1729–1731 (2008).
- [93] Lifshitz, E., Bashouti, M., Kloper, V., Kigel, A., Eisen, M., and Berger, S. *Nano Letters* **3**, 857–862 (2003).
- [94] Zutz, F., Lokteva, I., Radychev, N., Kolny-Olesiak, J., Riedel, I., Borchert, H., and Parisi, J. *Physica Status Solidi A-Applications and Materials Science* **206**, 2700–2708 (2009).
- [95] Heinemann, M. D., von Maydell, K., Zutz, F., Kolny-Olesiak, J., Borchert, H., Riedel, I., and Parisi, J. *Advanced Functional Materials* **19**, 3788–3795 (2009).
- [96] Radychev, N., Lokteva, I., Witt, F., Kolny-Olesiak, J., Borchert, H., and Parisi, J. *Journal of Physical Chemistry C* **115**, 14111–14122 (2011).
- [97] Lu, W., Fang, J., Stokes, K., and Lin, J. *Journal of the American Chemical Society* **126**, 11798–11799 (2004).
- [98] Steckel, J. S., Yen, B. K. H., Oertel, D. C., and Bawendi, M. G. *Journal of the American Chemical Society* **128**, 13032–13033 (2006).
- [99] Cademartiri, L., Montanari, E., Calestani, G., Migliori, A., Guagliardi, A., and Ozin, G. A. *Journal of the American Chemical Society* **128**, 10337–10346 (2006).
- [100] Yu, W., Falkner, J., Shih, B., and Colvin, V. *Chemistry of Materials* **16**, 3318–3322 (2004).
- [101] Hanrath, T., Veldman, D., Choi, J. J., Christova, C. G., Wienk, M. M., and Janssen, R. A. J. *ACS Applied Materials & Interfaces* **1**, 244–250 (2009).
- [102] Law, M., Luther, J. M., Song, O., Hughes, B. K., Perkins, C. L., and Nozik, A. J. *Journal of the American Chemical Society* **130**, 5974–5985 (2008).
- [103] Houtepen, A. J., Koole, R., Vanmaekelbergh, D., Meeldijk, J., and Hickey, S. G. *Journal of the American Chemical Society* **128**, 6792–6793 (2006).
- [104] Khan, F. A., Sudheer, C., and Soma, L. *Chemical Communications* , 4239–4241 (2007).
- [105] Cottrell, I. F., Moloney, M. G., and Smithies, K. *Tetrahedron Letters* **50**, 1097–1099 (2009).
- [106] Pradhan, B. and Ghosh, P. *Indian Journal of Chemistry. Section B - Organic Chemistry including Medicinal Chemistry* **31**, 631–632 (1992).
- [107] Pardhasaradhi, V. and Gowda, B. *Journal of the Indian Chemical Society* **68**, 327–330 (1991).
- [108] Coseri, S. *Journal of Physical Organic Chemistry* **22**, 397–402 (2009).
- [109] Heiba, E., Dessau, R., and Koehl, W. *Journal of the American Chemical Society* **90**, 2706–2707 (1968).
- [110] Foos, E., Wilkinson, J., Makinen, A., Watkins, N., Kafafi, Z., and Long, J. *Chemistry of Materials* **18**, 2886–2894 (2006).
- [111] Dai, Q., Wang, Y., Li, X., Zhang, Y., Pellegrino, D. J., Zhao, M., Zou, B., Seo, J., Wang, Y., and Yu, W. W. *ACS Nano* **3**, 1518–1524 (2009).
- [112] Selishcheva, E., Witt, F., Trautwein, N., Fenske, D., Neumann, J., Borchert, H., Parisi, J., and Kolny-Olesiak, J. *Physical Chemistry Chemical Physics* . Submitted.
- [113] Beek, W. J. E., Wienk, M. M., and Janssen, R. A. J. *Advanced Functional Materials* **16**, 1112–1116 (2006).



## BIBLIOGRAPHY

- [114] Oesterbacka, R., An, C., Jiang, X., and Vardeny, Z. *Science* **287**, 839–842 (2000).
- [115] Witt, F., Kruszynska, M., Borchert, H., and Parisi, J. *Journal of Physical Chemistry Letters* **1**, 2999–3003 (2010).
- [116] Takeda, Y., Kato, N., Higuchi, K., Takeichi, A., Motohiro, T., Fukumoto, S., Sano, T., and Toyoda, T. *Solar Energy Materials and Solar Cells* **93**, 808–811 (2009).
- [117] Chen, S.-Y., Wu, M.-C., Lee, C.-S., and Lin, M. C. *Journal of Materials Science* **44**, 794–798 (2009).
- [118] Wang, C., Chen, D., and Jiao, X. *Journal of Physical Chemistry C* **113**, 7714–7718 (2009).
- [119] El-Maghraby, E. M., Ahsanulhaq, Q., and Yamazaki, T. *Journal of Nanoscience and Nanotechnology* **10**, 4950–4954 (2010).
- [120] Askarinejad, A., Iranpour, M., Bahramifar, N., and Morsali, A. *Journal of Experimental Nanoscience* **5**, 294–301 (2010).
- [121] Hu, W. B., Tian, D. T., Mi, Y. Z., Nie, G. H., Zhao, Y. M., Liu, Z. L., and Yao, K. L. *Materials of Chemistry and Physics* **118**, 277–280 (2009).
- [122] Acacia, N., Barreca, F., Barletta, E., Spadaro, D., Curro, G., and Neri, F. *Applied Surface Science* **256**, 6918–6922 (2010).
- [123] Yang, H., Yang, Z., Liang, H., Liu, L., Guo, J., and Yang, Y. *Materials Letters* **64**, 1418–1420 (2010).
- [124] Tseng, T.-T. and Tseng, W. J. *Ceramics International* **35**, 2837–2844 (2009).
- [125] Narayanaswamy, A., Xu, H., Pradhan, N., Kim, M., and Peng, X. *Journal of the American Chemical Society* **128**, 10310–10319 (2006).
- [126] Ohhata, Y., Shinoki, F., and Yoshida, S. *Thin Solid Films* **59**, 255–261 (1979).
- [127] Koo, B., Patel, R. N., and Korgel, B. A. *Journal of the American Chemical Society* **131**, 3134–3135 (2009).
- [128] Yin, W., Su, J., Cao, M., Ni, C., Cloutier, S. G., Huang, Z., Ma, X., Ren, L., Hu, C., and Wei, B. *Journal of Physical Chemistry C* **113**, 19493–19499 (2009).
- [129] Donega, C. d. M. *Chemical Society Reviews* **40**, 1512–1546 (2011).
- [130] Huang, S., Huang, J., Yang, J., Peng, J.-J., Zhang, Q., Peng, F., Wang, H., and Yu, H. *Chemistry-A European Journal* **16**, 5920–5926 (2010).
- [131] Hao, R., Xing, R., Xu, Z., Hou, Y., Gao, S., and Sun, S. *Advanced Materials* **22**, 2729–2742 (2010).
- [132] Dimitrijevi, N. M., Rajh, T., Ahrenkiel, S. P., Nedeljkovi, J. M., Mii, O. I., and Nozik, A. J. *The Journal of Physical Chemistry B* **109**, 18243–18249 (2005).
- [133] Berr, M., Vaneski, A., Susha, A. S., Rodriguez-Fernandez, J., Doblinger, M., Jackel, F., Rogach, A. L., and Feldmann, J. *Applied Physics Letters* **97**, 093108 (2010).
- [134] Menagen, G., Macdonald, J. E., Shemesh, Y., Popov, I., and Banin, U. *Journal of the American Chemical Society* **131**, 17406–17411 (2009).
- [135] Carbone, L., Jakab, A., Khalavka, Y., and Sonnichsen, C. *Nano Letters* **9**, 3710–3714 (2009).
- [136] Yang, J., Levina, L., Sargent, E. H., and Kelley, S. O. *Journal of Materials Chemistry* **16**, 4025–4028 (2006).
- [137] Puzder, A., Williamson, A., Zaitseva, N., Galli, G., Manna, L., and Alivisatos, A. *Nano Letters* **4**, 2361–2365 (2004).
- [138] Mokari, T., Sztrum, C., Salant, A., Rabani, E., and Banin, U. *Nature Materials* **4**, 855–863 (2005).
- [139] Xie, R., Rutherford, M., and Peng, X. *Journal of the American Chemical Society* **131**, 5691–5697 (2009).
- [140] Allen, P. M. and Bawendi, M. G. *Journal of the American Chemical Society* **130**, 9240–9241 (2008).
- [141] Kruszynska, M., Borchert, H., Parisi, J., and Kolny-Olesiak, J. *Journal of Nanoparticle Research* **13**, 5815–5824 (2011).

## BIBLIOGRAPHY

---

- [142] Xu, Y. and Li, Q. *Nanoscale* **3**, 3238–3243 (2011).
- [143] Qi, Y., Liu, Q., Tang, K., Liang, Z., Ren, Z., and Liu, X. *The Journal of Physical Chemistry C* **113**, 3939–3944 (2009).
- [144] Norako, M. E. and Brutchey, R. L. *Chemistry of Materials* **22**, 1613–1615 (2010).
- [145] Batabyal, S. K., Tian, L., Venkatram, N., Ji, W., and Vittal, J. J. *The Journal of Physical Chemistry C* **113**, 15037–15042 (2009).
- [146] Wang, J.-J., Wang, Y.-Q., Cao, F.-F., Guo, Y.-G., and Wan, L.-J. *Journal of the American Chemical Society* **132**, 12218–12221 (2010).
- [147] Malik, M. A., O'Brien, P., and Revaprasadu, N. *Advanced Materials* **11**, 1441–1444 (1999).
- [148] Khalavka, Y. and Soennichsen, C. *Advanced Materials* **20**, 588–591 (2008).

# Lebenslauf

## Elena Selishcheva

### Persönliche Daten

Geschlecht: weiblich

Geburtsdatum: 4. Februar 1985

Geburtsort: Woronesch, Russland

Staatsangehörigkeit: russisch

Familienstand: ledig

### Schulbildung

09/1998–06/2002 Gymnasium in Woronesch (Russland)

Abschluss: Abitur (Gesamtnote: sehr gut)

### Studium

09/2002–06/2007 Chemie-Studium an der Staatlichen Universität Woronesch (Russland)

Abschluss: Diplom-Chemikerin (mit Auszeichnung)

Schwerpunkt: Analytische Chemie

Thema der Diplomarbeit: Spektroskopische Untersuchung diverser medizinischer Präparate

### Berufserfahrung und Promotion

09/2007–06/2008 Mitarbeiterin im analytischen Labor an der Firma „Elektrosignal“ (Woronesch, Russland)

Aufgabenbereich: Luftkontrolle nach gesundheitsschädlichen Stoffen am Arbeitsplatz der Mitarbeiter

07/2008–12/2011 Doktorandin und wissenschaftliche Mitarbeiterin an der Carl von Ossietzky Universität Oldenburg, Institut für Physik, Abteilung Energie- und Halbleiterforschung, Arbeitsgruppe Nanochemie

Forschungsbereich: Synthese und Charakterisierung von Halbleiter- und Metall-Halbleiter-nanopartikeln

# Verzeichnis wissenschaftlicher Publikationen

## Artikel in Zeitschriften

1. Elena Selishcheva, Florian Witt, Niklas Trautwein, Daniela Fenske, Johannes Neumann, Holger Borchert, Jürgen Parisi, and Joanna Kolny-Olesiak. Synthesis of Lead Chalcogenide Nanocrystals and Study of Charge Transfer in Blends of PbSe Nanocrystals and Poly(3-hexylthiophene). Physical Chemistry Chemical Physics, eingereicht.
2. Elena Selishcheva, Jürgen Parisi, and Joanna Kolny-Olesiak. Copper-Assisted Shape Control in Colloidal Synthesis of Indium Oxide Nanoparticles. Journal of Nanoparticle Research, 14 (2012), 711 (DOI: 10.1007/s11051-011-0711-6).
3. Diyar Sadiq, Javid Shirdel, Jae Sung Lee, Elena Selishcheva, Namkyoo Park, and Christoph Lienau. Adiabatic Nanofocusing Scattering-Type Optical Nanoscopy of Individual Gold Nanoparticles. Nano Letters, 11 (2011), 1609-1613.

## Konferenzbeitrag

Elena Selishcheva, Florian Witt, Niklas Trautwein, Holger Borchert, Jürgen Parisi, and Joanna Kolny-Olesiak. Photoinduced Charge Transfer in Blends of PbSe Nanocrystals and Poly(3-hexylthiophene). Posterpräsentation. DPG Frühjahrstagung 2011, 13.-18. März 2011, Dresden.

## **Erklärung**

Hiermit erkläre ich, dass ich diese Arbeit selbstständig und nur unter zu  
Hilfenahme der angegebenen Hilfsmittel angefertigt habe.

Oldenburg, den 10. November 2011